

# Two-Dimensional Phononic Crystal Simulation and Analysis

by

Ryan Christopher Norris

A thesis  
presented to the University of Waterloo  
in fulfilment of the  
thesis requirement for the degree of  
Master of Applied Science  
in  
Electrical and Computer Engineering

Waterloo, Ontario, Canada, 2005

© Ryan Norris 2005

I hereby declare that I am the sole author of this thesis. This is a true copy of the thesis, including any required final revisions, as accepted by my examiners.

I understand that my thesis may be made electronically available to the public.

# Abstract

This thesis presents the design of a two-dimensional phononic band gap crystal simulator, and phononic crystal analysis.

Phononic crystals and their application to microwave acoustic filters are studied. Wave mechanics is introduced. A two-dimensional phononic crystal simulator is developed. Simulator operation is validated through comparison with published data. Design parameters for phononic crystal band gap engineering are outlined. Digital signal processing and wave mechanics are utilized to analyze fractal and circular inclusion based phononic crystals. Topics for further study are given.

Phononic crystal band structure is found to be sensitive to inclusion boundary geometry. Fractal inclusion based crystals provide multiple pass band characteristics. The evolution of a fractal inclusion in a phononic crystal may cause band gap widening and the formation of new band gaps. Circular inclusion based phononic crystals have piecewise-linear phase characteristics and quality factors up to 600.

# Acknowledgments

I would like to recognize Professor John Starr Hamel for his inventiveness in combining the disciplines of microwave acoustic filter engineering, phononic band gap crystal engineering, and micro-electro-mechanical-system engineering to create the novel class of filtering devices known as silicon integrated phononic band gap filters. Many thanks go to Professor Hamel for granting me the opportunity to perform research with him in this new and expanding research effort. During my study with him, Professor Hamel has provided me with the the fundamental knowledge required to rapidly break into the silicon integrated phononic band gap filter research effort. This thesis is a testament of his ingenuity.

# Dedication

This thesis is dedicated to Professor John Starr Hamel and the advancement of the silicon integrated phononic band gap filter research effort.

# Contents

<b>1</b>	<b>Introduction to Phononic Crystals and Their Applications</b>	<b>1</b>
1.1	Linguistic Stipulations . . . . .	2
1.2	Microwave Acoustic Filters . . . . .	3
1.3	Micro-Electro-Mechanical-System Transducers . . . . .	7
1.4	Phononic Band Gap Filters . . . . .	9
1.5	Outline of Thesis Subject Matter . . . . .	11
<b>2</b>	<b>Wave Mechanics</b>	<b>13</b>
2.1	Group Delay . . . . .	16
2.2	Phase Delay . . . . .	16
2.3	Phase Velocity . . . . .	17
2.4	Wave Vector . . . . .	18

<b>3</b>	<b>Two-Dimensional Phononic Crystal Simulator Development</b>	<b>20</b>
3.1	The Elastic Wave Equation . . . . .	23
3.2	Finite Difference Time Domain Solution to Elastic Wave Equation .	25
3.3	The Absorbing Boundary Condition . . . . .	32
3.4	The Periodic Boundary Condition . . . . .	38
3.5	Simulator . . . . .	44
3.5.1	Simulator Inputs . . . . .	44
3.5.2	Source and Detector Locations . . . . .	55
3.5.3	Program Flow . . . . .	56
3.6	On Choosing $k_{max}$ . . . . .	59
3.7	Verification of Simulator Operation . . . . .	61
3.7.1	The Absorbing Boundary Condition . . . . .	62
3.7.2	The Periodic Boundary Condition . . . . .	65
3.7.3	Reproducing Published Data . . . . .	67
3.7.4	Conclusions . . . . .	78
<b>4</b>	<b>Two-Dimensional Phononic Crystal Analysis</b>	<b>81</b>
4.1	Phononic Crystal Band Gap Engineering . . . . .	82
4.2	Fractal Inclusion Based Phononic Crystals . . . . .	85
4.2.1	Introduction to Fractal Crystals . . . . .	85

4.2.2	Representation of Fractal Structures on a Discrete Grid . . .	88
4.2.3	Uniformity of Simulation Conditions . . . . .	89
4.2.4	Wavelength Characteristics . . . . .	94
4.2.5	Forward Transmission Parameter Characteristics . . . . .	104
4.2.6	Band Gap Engineering Functions of Fractals . . . . .	111
4.2.7	Reflection, Refraction, and Diffraction in a Fractal Based Phononic Crystal . . . . .	111
4.2.8	Fractals For Use In Generalized Boundaries . . . . .	113
4.2.9	Implications of Fractal Structure Simulation Results . . . . .	113
4.3	Circular Inclusion Based Phononic Crystals . . . . .	114
4.3.1	Transient Response . . . . .	114
4.3.2	Bode Plots . . . . .	117
4.3.3	Group Delay Characteristics . . . . .	119
4.3.4	Phase Delay Characteristics . . . . .	120
4.3.5	Phase Velocity Characteristics . . . . .	120
4.3.6	Dispersion Characteristics . . . . .	122
4.3.7	Quality Factor Characteristics . . . . .	123
<b>5</b>	<b>Conclusions and Topics for Further Study</b>	<b>125</b>
<b>A</b>	<b>Material Constants</b>	<b>130</b>



<b>B Fractal Inclusion Layout</b>	<b>131</b>
<b>Bibliography</b>	<b>142</b>

# List of Tables

1.1	Comparison of microwave acoustic filters [2], [3]. . . . .	5
1.2	Microwave acoustic filters applications [2]. . . . .	6
3.1	Typical values of $\Delta t$ that provide good convergence for various systems.	48
3.2	Simulation constants for the simulation of the layered structure. . .	70
3.3	Simulation constants for the simulation of the aluminium-air crystal.	75
3.4	Simulation constants for the simulation of the aluminium-mercury crystal. . . . .	78
4.1	Fractal inclusion structures [25]. . . . .	86
4.2	Simulation constants for the simulation of fractal systems. . . . .	92
4.3	Simulation variables for the simulation of fractal systems. . . . .	93
4.4	Wavelength at 3.5[MHz] for all fractal based crystal structures. . .	102
4.5	Minimum feature sizes of fractal inclusion structures. . . . .	103
4.6	Simulation constants for the simulation of a phononic crystal that is composed of circular inclusions. . . . .	115

A.1 Material parameters. . . . . 130

# List of Figures

1.1	Types of microwave acoustic devices. List of acronyms: SAW (Surface Acoustic Wave), BAW (Bulk Acoustic Wave), LF (Low Frequency), TFR (Thin Filter Resonator), HF (High Frequency), PBG (Phononic Band Gap), FBAR (Film Bulk Acoustic Wave Resonator), SMR (Solidly Mounted Resonator). . . . .	4
2.1	Experimental setup of plane wave source and point detector. . . . .	14
3.1	Discrete grid representation of discrete space. . . . .	27
3.2	Simulation space. . . . .	33
3.3	Pictorial depiction of the operation of the PBC equations. The depicted simulation space measures 5[ <i>nodal units</i> ] by 6[ <i>nodal units</i> ]. The computational domain measures 3[ <i>nodal units</i> ] by 4[ <i>nodal units</i> ]. The $u_x$ component of the displacement vector is shown located in the PBC domains, and at the top and bottom edges of the computational domain. . . . .	40
3.4	Map of inputs to $u_x$ (Equation 3.15) at time $k_{cur}$ . . . . .	41

3.5	Illustration of how ABCs and PBCs act to make the two-dimensional simulation space into an infinitely long cylindrical simulation space. The arrows indicate the path of elastic wave propagation. The left edge ABC domain is not shown. . . . .	43
3.6	Illustration of the parameters that characterize the structure of a phononic crystal. The following abbreviations are applied in the figure: the lattice constant, $acell_{NODES}$ , has been abbreviated as $a$ ; the total width of the homogeneous region, $homo_{WIDTH}$ , has been abbreviated as $homo$ ; the inclusion material density, $\rho_{inclusion}$ , has been abbreviated as $\rho_i$ ; the host material density, $\rho_{host}$ , has been abbreviated as $\rho_h$ . The unit cell is depicted as a square inclusion for illustration purposes only. . . . .	47
3.7	The transient response of the source signal induced into the phononic crystal as detected at a location just beside the plane wave source ( $\Delta t = 0.997623539[ns]$ ). The envelope of the transient response appears to be an exponentially decaying function: the dotted curve is given by $\frac{2.5 \times 10^{-9}}{44400000(t - 0.75 \times 10^{-6})} + 0.4 \times 10^{-8}$ . . . . .	53
3.8	The discrete fourier transform of the source signal of Figure 3.7. . .	54
3.9	Overall program flow of the phononic band gap crystal simulator. .	57
3.10	Program flow of the FDTD block of the phononic crystal simulator.	58
3.11	Snapshots of wave traveling into the boundary of the simulation space with no boundary condition applied. . . . .	63

3.12	Snapshots of wave traveling into the boundary of the simulation space with ABC applied. . . . .	64
3.13	Verification of PBC operation for source at node 3 (close up near the location of the source). As seen in the figure, the plane wave source is located two nodal units away from the PBC domain. . . . .	66
3.14	Verification of PBC operation for source at node 75. . . . .	67
3.15	Structure of the Bragg grating. The lattice constant, $a_{cell_{NODES}}$ , has been abbreviated as $a$ . The thickness of the plates is denoted using the variable $t$ . The plates are composed of Perspex, while the host material is water. Finally, $t = 0.2[cm]$ and $a = 0.724[cm]$ . . . . .	69
3.16	Transient response of the layered structure, of Figure 3.15, as detected by a point detector. . . . .	71
3.17	Magnitude response of the layered structure of Figure 3.15. . . . .	72
3.18	Magnitude response of a two-dimensional phononic crystal that is composed of an aluminum host and circular air inclusions. The data curves that are attributed to Sun in the legend were taken from [21].	76
3.19	Magnitude response of a two-dimensional phononic crystal that is composed of an aluminum host and circular mercury inclusions. The data curves that are attributed to Garcia in the legend were taken from [23]. . . . .	79
4.1	Arbitrary structure represented on discrete grid. . . . .	90

4.2	Wavelength characteristic for a filter created using the Initial Square inclusion structure, and the wavelength characteristic for the aluminum inclusion material and the mercury host material. For the filter created using the Initial Square structure $a_{cell_{CM}} = 0.24[cm]$ .	96
4.3	Wavelength characteristic for Structure 1 (please refer to the legend of Figure 4.2).	98
4.4	Wavelength characteristic for Structure 2 (please refer to the legend of Figure 4.2).	99
4.5	Wavelength characteristic for Structure 3 (please refer to the legend of Figure 4.2).	100
4.6	Forward transmission parameters for Structure 1.	105
4.7	Forward transmission parameters for Structure 2.	106
4.8	Forward transmission parameters for Structure 3.	107
4.9	Lattice vibrations within the unit cell for the Initial Square Structure (left), Iteration 1 of Structure 3 (center) and Iteration 2 of Structure 3 (right). The amplitude of vibration in the regions that are shaded white are larger than the amplitude of vibrations in the regions that are shaded black.	112
4.10	Transient response of the phononic crystal that was created using circular inclusion structures.	116

4.11	The Bode plot that was generated by taking the discrete fourier transform of the transient response of the phononic crystal that was created using circular inclusion structures. . . . .	117
4.12	Magnitude response on a logarithmic axis. . . . .	118
4.13	Group delay characteristic of the phononic crystal created from circular inclusions. . . . .	119
4.14	Phase delay characteristic of the phononic crystal created from circular inclusions. . . . .	120
4.15	Phase velocity characteristic of the phononic crystal created from circular inclusions. . . . .	121
4.16	Dispersion characteristic of the phononic crystal created from circular inclusions. . . . .	122
4.17	Quality factor characteristic of the phononic crystal created from circular inclusions. . . . .	124
B.1	Layout of Initial Square Structure. . . . .	132
B.2	Layout of Structure 1 Iteration 1. . . . .	133
B.3	Layout of Structure 1 Iteration 2. . . . .	134
B.4	Layout of Structure 2 Iteration 1. . . . .	135
B.5	Layout of Structure 2 Iteration 2. . . . .	136
B.6	Layout of Structure 3 Iteration 1. . . . .	137
B.7	Layout of Structure 3 Iteration 2. . . . .	138



# Chapter 1

## Introduction to Phononic Crystals and Their Applications

Phononic band gap crystals are periodic structures created through the repeated placement of one, two- or three-dimensional unit cells. The unit cell is comprised of a host medium in which an inclusion medium is embedded. The host medium and inclusion medium differ in their material properties, such as density and elastic wave velocities. Energy is transmitted through the phononic band gap crystal via an elastic wave.

The phononic band structure of a phononic band gap crystal is analogous to the electronic band structure of semiconductors, and the electromagnetic band structure of photonic band gap crystals. The electronic band structure of a semiconductor is a consequence of the wave nature of the electrons present in a periodic lattice of atomic nuclei. The electromagnetic band structure of a photonic band gap crystal

results from the presence of electromagnetic waves in a periodic lattice of inclusions, whose dielectric constant contrasts that of the host medium. The phononic band structure results from the presence of elastic waves in the phononic band gap crystal. "Phononic band gap" crystals are often also referred to as "acoustic band gap" crystals, "elastic band gap" crystals or "sonic band gap" crystals.

This introductory chapter continues, in the next section, by clarifying the aforementioned terminology. An introduction to contemporary microwave acoustic filters follows. For a phononic band gap crystal to perform a filtering operation in microwave acoustic filters, an electromechanical transducer would be required to convert electrical signals to elastic wave vibrations and vice versa. Micro-Electro-Mechanical-System (MEMS) transducer technologies are later introduced as an electromechanical transducer solution. The invention of the silicon integrated phononic band gap filter is then formalized. The introduction concludes by outlining the thesis subject matter.

## **1.1 Linguistic Stipulations**

The term "phononic" was derived in analogy to the term "phonon", which is a quanta of energy that characterizes atomic vibrations. Phonons may have wavelengths with a magnitude on the order of the atomic crystal lattice constant [1]. Similarly, the elastic wave vibrations, in phononic band gap crystals, may have wavelengths on the order of the phononic band gap crystal lattice constant.

In the special case, where the elastic wave wavelength becomes much greater

than the phononic band gap crystal lattice constant, then the term "acoustic band gap" or "elastic band gap" is also accurate. However, the wavelength of elastic waves is usually only larger than the crystal lattice constant at low frequencies (near zero hertz where the wavelength approaches infinity).

The term "acoustic band gap" crystal may also be being utilized, to draw analogy with the nomenclature used to describe microwave acoustic filters, such as Surface Acoustic Wave (SAW) and Bulk Acoustic Wave (BAW) filters. The term "sonic" and "acoustic" are interchangeable.

It may be seen then, that the term "phononic band gap crystal" scientifically describes a device that may contain elastic wave vibrations at relatively arbitrary wavelengths. Appropriately, the term "phononic band gap" will be used throughout this thesis.

The terms "phononic band gap crystal" and "phononic crystal" will be used synonymously.

## **1.2 Microwave Acoustic Filters**

Phononic crystals may be utilized to perform a filtering operation in microwave acoustic filters. A similarity exists between phononic crystal based filtering devices and SAW and BAW filtering devices in that the propagation of energy in these devices is described using elastic wave mechanics. Figure 1.1, categorizes some commonly used microwave acoustic devices. A phononic crystal based filter would be categorized as a BAW device since the energy carrying elastic waves travel

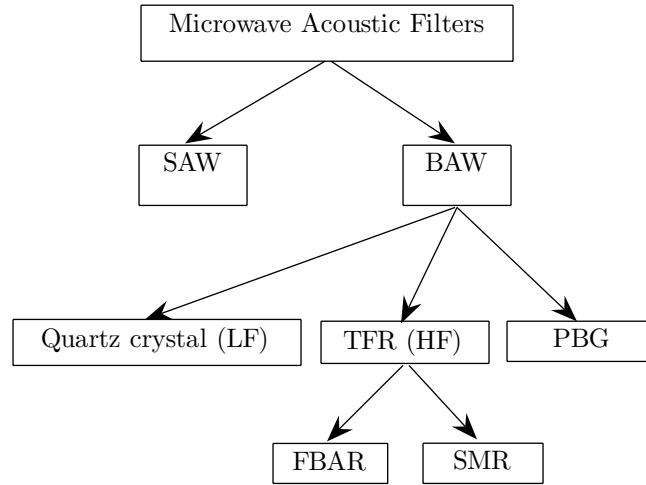


Figure 1.1: Types of microwave acoustic devices. List of acronyms: SAW (Surface Acoustic Wave), BAW (Bulk Acoustic Wave), LF (Low Frequency), TFR (Thin Filter Resonator), HF (High Frequency), PBG (Phononic Band Gap), FBAR (Film Bulk Acoustic Wave Resonator), SMR (Solidly Mounted Resonator).

through the bulk of the crystal structure. This is in contrast to a SAW device where the energy carrying wave travels along the surface of the structure.

Advantages and disadvantages of SAW devices, BAW devices and the proposed phononic crystal based filters are listed in Table 1.1. Table 1.1 may be summarized by stating that SAW filtering devices are capable of wider bandwidth, however, BAW filtering devices will outperform SAW filtering devices in high Q (quality factor) and high frequency applications. While SAW and BAW devices are established technologies, phononic crystal based devices are purely in the research and development phase. Applications of SAW, BAW and phononic crystal based filters are listed in Table 1.2.

Though phononic crystal based microwave acoustic filters are under research and development, it is known that a phononic crystal based filter would perform

Table 1.1: Comparison of microwave acoustic filters [2], [3].

	Surface Acoustic Wave	Bulk Acoustic Wave	Phononic Band Gap (proposed)
Advantages	<p>Package footprint size on the order of <math>mm \times mm</math></p> <p>Magnitude response and group delay can be designed independently</p> <p>Unassisted SAW has higher bandwidth than BAW filter</p> <p>Linear phase response (transversal SAW filter)</p>	<p>Package footprint size on the order of <math>mm \times mm</math></p> <p>Operating frequency range: 600[MHz] to 12[GHz] (conservatively)</p> <p>Excellent power handling at frequencies up to 10[GHz] without expensive photolithographic equipment and fabrication processes</p> <p>Lower insertion loss than SAW devices</p> <p>Higher Q than SAW devices</p> <p>Small layout SMRs show promise for integration onto substrates</p>	<p>Multiple degrees of freedom in band gap engineering</p> <p>Device scaling would allow the operating frequency range to be easily increased</p> <p>Magnitude response and group delay may be designed independently</p>
Disadvantages	<p>Contamination of wave propagation surface disturbs device operation, so hermetic packaging is required</p> <p>Inter-Digital transducer size decreases as frequency increases and feature sizes become too small to fabricate reliably, maximum operating frequency is thus limited by minimum Inter-Digital Transducer line width</p> <p>May be incompatible with standard silicon processes, and thus are off-chip filters</p> <p>Power handling decreases with frequency</p> <p>Operating frequency range: 10[MHz] to 3[GHz] (impractically large size at some low intermediate frequencies)</p> <p>Modest Q (relative to BAW filter)</p>	<p>At least one vibrating surface will be exposed to the ambient and so hermetic packaging is required</p> <p>Incompatible with standard silicon processes, and thus are off-chip filters</p> <p>At high frequency film thickness becomes small and the thin films are difficult to fabricate</p>	<p>Magnitude response of the overall filter may be a function of the resonant frequency of the MEMS transducer</p> <p>Maximum operating frequency is limited by minimum fabrication process feature size</p> <p>May require a wide band transducer</p> <p>Still in research and development phase, many problems to be addressed</p>
Wave location	Surface	Bulk	Bulk

Table 1.2: Microwave acoustic filters applications [2].

	Surface Acoustic Wave	Bulk Acoustic Wave	Phononic Band Gap (proposed)
Applications	High selectivity filter in mobile phone and radio front ends	Global Positioning System receiver front end (TFR based lattice or lattice filter)	Fully integrated on-chip band pass or low pass filters for transceiver front end
	Analog signal processing: delay lines, tapped delay lines, chirp filters, convolvers, duplexers, correlators, multiplexers and demultiplexers	Thin film SMRs for integration with microwave heterojunction bipolar transistor voltage controlled oscillators	Low power communications
	Intermediate frequency band pass filters in television receivers	FBARs have been used in cellular phone transceiver front ends	Multiplexers, demultiplexers, elastic waveguides
	Wireless passive identification tags, sensors, passive transponders, microbalances, ladder filters, resonators (precision clock oscillators), digital radios, satellites, modems  Pulse compression filters for radar systems	Duplexers, delay lines, crystal resonators, SMRs, FBARs	

a filtering operation by a fundamentally new mechanism. The filtering operation is determined by the elastic band structure of the phononic crystal. Moreover, a phononic crystal based filter may not require the use of a piezoelectric transducer to induce elastic waves into the phononic crystal.

The transducer utilized in a SAW or a BAW device is partially composed of a piezoelectric material. It may be possible to incorporate a phononic crystal into a SAW or BAW device in order to exploit the phononic band gap phenomenon to further alter the frequency response of the SAW and BAW devices. This, however, would not leverage the notion that a phononic crystal based filter may not necessarily require a piezoelectric transducer. The MEMS transducer solution for phononic crystal based devices is discussed next.

## 1.3 Micro-Electro-Mechanical-System

### Transducers

SAW and BAW filtering devices utilize a piezoelectric transducer and so these devices are not purely mechanical devices, and may not be fabricated in standard silicon processes. Moreover, in the case of a SAW device, the piezoelectric transducer may not be eliminated since the frequency response of the SAW device is a function of the geometry of the piezoelectric Inter-Digital Transducer (IDT).

In contrast, it may be possible that the frequency response of a phononic crystal based filter be determined by the phononic crystal itself. The MEMS developer would be free to design the actuator and sensor transducers in a novel fashion. The utilization of MEMS transducers in phononic band gap crystal based filtering devices would result in a filtering system that is purely mechanical.

It may be likely that a phononic crystal can be fabricated in a standard silicon process. Since a MEMS transducer may also be fabricated in a standard silicon process, it may be possible to integrate a phononic crystal based filter with other microelectronic circuits and systems. This may, for example, enable the fabrication of a single chip transceiver where microwave filtering devices and mixed signal integrated circuits are fabricated in a single silicon process.

The required transducer must convert electrical signals into elastic wave vibrations, which are mechanical deformations, and such a transducer is referred to as an electromechanical transducer. The silicon integrated phononic crystal based filter development challenge is then to develop an electromechanical transducer that can

be fabricated in a standard silicon process. A list of MEMS structures that may provide the required transduction capabilities includes:

1. current carrying wires (a mechanical force is generated between current carrying wires),
2. a capacitive micromachined ultrasonic transducer (for example, a capacitive diaphragm transducer),
3. a clamped-clamped beam with electrostatic electrodes [4], and
4. an electrostatic comb drive [4].

Clamped-clamped beams, and electrostatic comb drives, have been used to create electrostatic coupled beam filters, and comb drive filters, respectively [4]. In the electrostatic coupled beam filter, two clamped-clamped resonators (one at the input and one at the output) are couple via a beam. The comb drive filter consists of two comb drives (one at the input and one at the output), which are also coupled via a beam. In both cases, the elastic wave signal flow path from the input to the output is through the beam structure. Creating a phononic crystal based filter may involve incorporating a phononic crystal into this beam structure.

In such a configuration, the elastic wave would travel from the input transducer, through the phononic crystal beam structure, and to the output transducer. The signal would thus be filtered according to the frequency response of the phononic crystal that is embedded in the beam, achieving the desired filtering operation.

Many design challenges were not addressed here, however, the utility of MEMS transducers in the development of silicon integrated phononic crystal based filter



structures was illustrated. The origin of the notion of phononic band gap filters will now be elaborated upon.

## 1.4 Phononic Band Gap Filters

The seminal papers that describe phononic crystals and the phononic band structure were presented by Sigalas in 1992 [5] and Kushwaha in 1993 [6]. In 1992, Sigalas proposed that phononic crystals may find application in devices that perform a filtering operation.

As eluded to above, the combination of phononic crystals and MEMS transducer technologies may create a new breed of on-chip integrated microwave acoustic filtering devices, for which the name "silicon integrated phononic band gap filter" has been coined.

The functional feature of a phononic crystal may be observed through an examination of the phononic crystal frequency response. The frequency response of a phononic crystal contains band gaps: frequency bands in which neither an elastic traveling wave nor an elastic standing wave may exist. Through band gap engineering, the frequency response of phononic crystals may be developed to create a wide variety of filtering characteristics. Phononic crystals have been demonstrated to generate low pass filter, band pass filter, band stop filter, waveguide [7], multiplexing [8], and demultiplexing [8] phenomenon.

In essence, a phononic band gap filter would be comprised of a phononic crystal, which is sandwiched between two electromechanical transducers, and hence is

comprised of at least three components:

1. an input actuator electromechanical transducer,
2. the phononic crystal, and
3. the output sensor electromechanical transducer.

MEMS transducers were described in the previous section. Additional elements that the phononic band gap filter may require include acoustic impedance matching and reflective layers.

If solidly mounted to the substrate, the phononic crystal based device may be acoustically isolated from the substrate using quarter wave reflectors (as in Solidly Mounted Resonators (SMRs)) or acoustically impedance matched to the substrate using acoustic absorbers (possibly similar to those utilized in SAW devices).

Alternatively, the device may be isolated from the substrate by being mounted on a suspended membrane (as in Film Bulk Acoustic Wave Resonators (FBARs)), or the crystal may be fabricated directly in the suspended membrane. The membrane may be suspended using tethers, which may have a taper geometry (like the cross section of an electromagnetic horn antenna), to acoustically impedance match the device to the silicon substrate. Scattered waves traveling into the tethers will not be reflected back into the device, and so would not interfere with the operation of the device.

The challenge of fabricating a silicon integrated phononic band gap filter may be summarized by stating that the real world device must realize the functionality of

the theoretical structures (such as, Absorbing Boundary Conditions (ABCs), Perfectly Matched Layers (PMLs) or Periodic Boundary Conditions (PBCs)) that are implemented in device simulators. Realization of the theoretical structures is subject to the constraints (such as, mask errors, material availability, minimum feature size and minimum economically affordable mask address unit) of the fabrication process.

Projecting into the future, if it were possible to integrate several phononic crystal based filters into a reasonable die area, a parallel bank of such filters could be realized. Each filter in the filter bank could be tuned to a different channel. If the quality factor ( $Q$ ) of each filter was sufficiently high, it has been proposed that such a filter bank may be used to develop a new front-end receiver architecture in which channel selection is performed at radio frequencies [9]. Performing channel selection at radio frequencies would alleviate low noise amplifier linearity and local oscillator phase noise requirements, thereby reducing the power consumption of these components [9]. For this reason, as stated in Table 1.2, a silicon integrated phononic band gap filter may find application in low power communications.

## **1.5 Outline of Thesis Subject Matter**

The attention of this thesis is confined to two topics:

1. the development of a simulator that can simulate phononic crystals that are composed of two-dimensional units cells arranged on a square lattice: a two-dimensional phononic band gap crystal simulator, and

2. the analysis of the properties of the phononic crystals that have been simulated using this simulator.

Transducer development is not discussed so that exclusive attention is paid to the simulation and analysis of phononic crystals.

Chapter two of the thesis contains an introduction to wave mechanics, which provides the mathematical framework for the analysis of phononic crystals. In Chapter three, the development of the two-dimensional phononic band gap simulator is detailed. An analysis of two phononic crystals is found in Chapter four. The thesis concludes, in Chapter five, with suggested topics to further the study of silicon integrated phononic band gap filters.

# Chapter 2

## Wave Mechanics

A sinusoidal wave may be represented by [10]:

$$\psi(t, x) = A \cos\left(\frac{2\pi t}{T} - \frac{2\pi x}{\lambda}\right), \quad (2.1)$$

where  $\psi(t, x)$  is the displacement of the medium at time  $t$  and position  $x$ ,  $A$  is the amplitude of the wave,  $T$  is the temporal period, and  $\lambda$  is the spatial wavelength.

If the sinusoidal wave of Equation 2.1 is observed at a fixed point  $x = x_o$ , the period of the displacement versus time function,  $\psi(t, x_o)$  will be found to be  $T$ . If the sinusoidal wave of Equation 2.1 is observed at a fixed time  $t = t_o$ , the period of the displacement versus position function,  $\psi(t_o, x)$  will be found to be  $\lambda$ . The reciprocal of the temporal period,  $T$ , is the frequency,  $f$ :

$$f = \frac{1}{T}. \quad (2.2)$$

Consider the experimental setup of Figure 2.1. Waves are generated by a plane wave source and travel through the elastic medium toward the point detector. After a finite duration of time, waves will begin to arrive at, and be detected by, the point detector, which measures the displacement versus time function,  $\psi(t, x_o = d)$ .

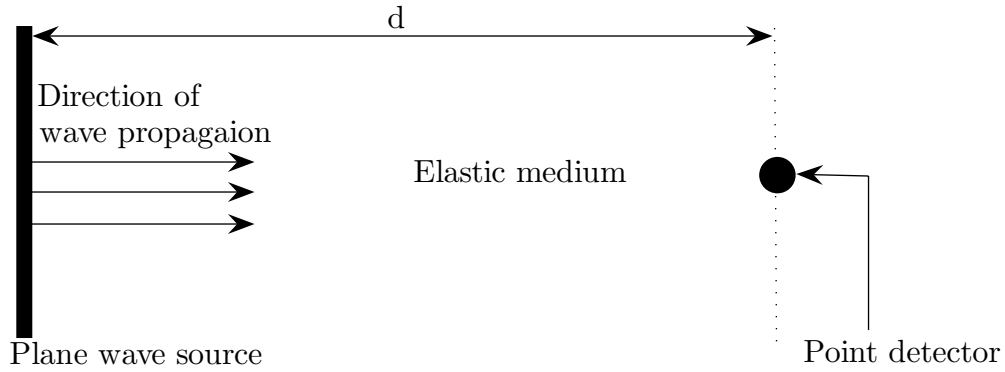


Figure 2.1: Experimental setup of plane wave source and point detector.

If the plane wave source generates the Dirac Delta function, which will be defined as

$$\delta(t) = \begin{cases} 0 & t \neq 0 \\ 1 & t = 0 \end{cases}, \quad (2.3)$$

then sinusoidal waves at all frequencies are induced into the elastic medium since the Fourier transform of Equation 2.3,  $F(\delta(t))$ , is equal to [11]

$$F(f(t)) \Big|_{f(t)=\delta(t)} = \int_{-\infty}^{\infty} f(t) e^{-j2\pi ft} dt \Big|_{f(t)=\delta(t)} = 1, \quad (2.4)$$

a constant for all  $f$ . Hence, by using the plane wave source to induce a unit impulse into the elastic medium, the displacement versus time function,  $\psi(t, x_o = d)$ , is equal to the impulse response,  $h(t)$ , of the elastic medium:

$$h(t) = \psi(t, x_o = d). \quad (2.5)$$

The Fourier transform of the impulse response,  $h(t)$ , is the transfer function,  $H(2\pi f)$ , of the elastic medium:

$$H(2\pi f) = \int_{-\infty}^{\infty} h(t) e^{-j2\pi f t} dt \Big|_{h(t)=\psi(t, x_o=d)} = \int_{-\infty}^{\infty} \psi(t, x_o = d) e^{-j2\pi f t} dt. \quad (2.6)$$

In general, the transfer function,  $H(2\pi f)$ , is a complex number that may be represented using a magnitude and a phase:

$$H(2\pi f) = |H(2\pi f)| e^{j\angle H(2\pi f)} = |H(2\pi f)| e^{j\Theta(2\pi f)}. \quad (2.7)$$

where  $|H(2\pi f)|$  is referred to as the magnitude response and  $\Theta(2\pi f) = \angle H(2\pi f)$  is referred to as the phase response. The quantity  $2\pi f$  is defined as the angular frequency,  $\omega$ :

$$\omega = 2\pi f. \quad (2.8)$$

The magnitude, and phase response, are often denoted as  $|H(\omega)|$  and  $\Theta(\omega)$ , re-

spectively, and provide a complete description of the system: for a sinusoidal input  $A\cos(\omega t)$ , the output is the sinusoid given by  $A|H(\omega)|\cos(\omega t + \Theta(\omega))$ . The phase response is less than zero:  $\Theta(\omega) < 0$ .

## 2.1 Group Delay

The group delay,  $\tau(\omega)_g$ , is defined as the rate of change of the phase response with respect to angular frequency [12]:

$$\tau(\omega)_g = -\frac{d\Theta(\omega)}{d\omega}, \quad (2.9)$$

and has the units of seconds.

Most signals can be defined over some finite, non-zero, bandwidth  $\omega_o \pm \delta\omega$ . Since the magnitude response  $|H(\omega)|$ , and group delay,  $\tau(\omega)_g$  are, in general, not a constant over the bandwidth,  $\omega_o \pm \delta\omega$ , the magnitude of each frequency component of the input signal will be scaled according to  $|H(\omega)|$  and have a group delay  $\tau(\omega)_g$ . In the time domain, the result is that the output signal will not resemble the input signal: the signal is said to have been distorted and the elastic medium is said to be dispersive.

## 2.2 Phase Delay

The phase delay,  $\tau(\omega)_p$ , is defined as the phase response divided by frequency:



$$\tau(\omega)_p = -\frac{\Theta(\omega)}{\omega}, \quad (2.10)$$

and has the units of seconds. The phase delay is the time, in seconds, taken for the signal to travel from the input to the output.

## 2.3 Phase Velocity

If the sinusoidal wave of Equation 2.1 is observed at a fixed displacement,  $\psi(t, x) = \psi_o$ , then Equation 2.1 may be rearranged as:

$$\frac{2\pi t}{T} - \frac{2\pi x}{\lambda} = \cos^{-1}\left(\frac{\psi_o}{A}\right). \quad (2.11)$$

Taking the derivative of position with respect to time, gives the definition of phase velocity,  $v_p$ :

$$v_p = \frac{dx}{dt} = \frac{\lambda}{T} = f\lambda, \quad (2.12)$$

which is the velocity of the sinusoidal wave. The experimentally determined phase response may be used to compute the phase velocity of a sinusoidal wave in the elastic medium:

$$v_p(\omega) = \frac{d}{\tau(\omega)_p}, \quad (2.13)$$

where  $d$  is the distance between the plane wave source and detector (as illustrated in Figure 2.1), and  $\tau(\omega)_p$  is the phase delay (as given by Equation 2.10).

When applied to phononic crystals, Equation 2.13 is only an approximation since the distance traversed by each frequency component, as it travels through the crystal, may not equal  $d$ . As may be observed in following chapters, low frequency components tend to be unaffected by the presence of the phononic crystal and so travel direct paths from the input to the output - hence Equation 2.13 may be accurate for low frequency components. However, as frequency increases, the phononic crystal becomes frequency selective and high frequency components may follow indirect paths as they traverse the phononic crystal - as a result the distance traveled may not equal  $d$ .

## 2.4 Wave Vector

The wave vector is defined as:

$$k(\omega) = \frac{2\pi}{\lambda(\omega)} = \frac{\omega}{v_p(\omega)}, \quad (2.14)$$

where Equation 2.12 was used to relate the wavelength,  $\lambda$ , to the phase velocity,  $v_p(\omega)$ . As described at the end of Section 2.3, Equation 2.13, for phase velocity,  $v_p(\omega)$ , is an approximation when applied to phononic crystals. Hence, Equation 2.14, for the wave vector,  $k(\omega)$ , which depends on Equation 2.13, is also an approximation when applied to phononic crystals.

Using Equation 2.8 for the angular frequency,  $\omega$ , and Equation 2.14 for the wave vector,  $k(\omega)$ , Equation 2.1 may be simplified to:

$$\psi(t, x) = A \cos(\omega t - k(\omega)x). \quad (2.15)$$

In summary, utilizing the experimentally determined phase response, the group delay, phase delay, phase velocity and wave vector may be computed. In a dispersive medium, the group delay, phase delay, phase velocity, and wave vector vary with frequency.

## Chapter 3

# Two-Dimensional Phononic Crystal Simulator Development

The discussion will begin with an explanation of why it is of interest to code a two-dimensional phononic band gap crystal simulator when a physically realizable device would be three-dimensional. When it is said that the simulator is a two-dimensional simulator, it is meant that the simulator is capable of simulating two-dimensional crystals.

A two-dimensional phononic crystal is a crystal that displays periodicity only in the  $\hat{x}$ - $\hat{y}$  plane, and the device geometry is uniform in the  $\hat{z}$  direction and so displays no periodicity in the  $\hat{z}$  direction. The structure is assumed to be infinitely thick in the  $\hat{z}$  direction.

Band gaps in the  $\hat{x}$  and  $\hat{y}$  direction do not depend on device thickness in the  $\hat{z}$  direction. Hence, theoretically, the simulated  $\hat{x}$  and  $\hat{y}$  direction band structure

should match that of a crystal that has an arbitrary thickness in the  $\hat{z}$  direction. This justifies the assumption that the two-dimensional phononic crystal is infinitely thick in the simulator.

A three-dimensional crystal displays periodicity in all three physical directions (the  $\hat{x}$ ,  $\hat{y}$ , and  $\hat{z}$  directions). An elastic wave may have three components: two transverse components, and one longitudinal component. When a phononic crystal suppresses the propagation of all three components of the elastic wave vector at a given frequency, the crystal is said to display a "full band gap". It is more difficult to obtain a full band gap when using a two-dimensional phononic crystal [13], than it is when using a three-dimensional crystal. However, a two-dimensional phononic crystal would be easier to realize in planar integrated circuit fabrication processes, which is why the two-dimensional simulator is of interest.

One may wonder whether or not it is a hinderance that it is more difficult to obtain full band gaps using a two-dimensional phononic crystal. An abundance of two-dimensional phononic crystals having partial band gaps (a band gap for just one or two components of the elastic wave vector) have been discovered and are a topic of discussion in Chapter 4. It may be possible that the proposed silicon integrated phononic band gap filter be created using such a phononic crystal that has a partial band gap for only the longitudinal component, or one transverse component, of the elastic wave vector. This may simplify the development of the transducers that would be needed to create and detect the displacement of the phononic crystal since the transducer only has to operate in a single direction. Moreover, this illustrates that only a partial band gap may be required by a phononic crystal based filter.

If a full band gap were required, it has been shown [13] that altering the thickness, in the  $\hat{z}$  direction, of a thin two-dimensional crystal (thin meaning the crystal has a thickness in the  $\hat{z}$  direction that is much smaller than wavelength) causes the location of existing band gaps in the  $\hat{z}$  component of the displacement vector to change frequency. Band gaps in the  $\hat{x}$  and  $\hat{y}$  components of the displacement vector are independent of device thickness. Hence, if the thickness in the  $\hat{z}$  direction is chosen appropriately it would be possible to align a band gap in the  $\hat{z}$  component with the band gaps in the  $\hat{x}$  and  $\hat{y}$  components of the displacement vector thereby creating a full band gap. Full band gaps are also relatively easier to obtain with thick two-dimensional crystals [13] (thick meaning the crystal has a thickness in the  $\hat{z}$  direction that is much larger than wavelength).

An advantage of developing a filter from a crystal that only has a partial band gap in one direction is that it eases design constraints in the other directions. Let the  $\hat{x}$  direction be the longitudinal direction. Let the  $\hat{y}$  and  $\hat{z}$  directions be transverse directions. Consider a crystal that has a partial band gap for the  $\hat{x}$  and  $\hat{y}$  directions. Partial band gaps are independent of the device thickness in the  $\hat{z}$  direction. Hence, the designer may arbitrarily choose the thickness in the  $\hat{z}$  direction. This decreases the requirements on the fabrication process. Moreover, the designer is free to choose the device thickness in the  $\hat{z}$  direction to perform other functions, for example to decrease internal stress or to increase mechanical strength.

As a final note, due to the fact that the two-dimensional crystal thickness may be chosen arbitrarily, a phononic band gap filter may be fabricated out of a thin film or membrane and hence may be realizable using a planar Complementary Metal

Oxide Semiconductor (CMOS) compatible, or a surface micro-machining, process.

### 3.1 The Elastic Wave Equation

The energy carrying waves of interest in a phononic crystal are elastic waves. Elastic waves are described by the elastic wave equation an in inhomogeneous isotropic media:

$$\rho \frac{\delta^2 \vec{u}}{\delta t^2} = \vec{\nabla} \cdot \vec{T}, \quad (3.1)$$

where  $\rho$  is the material density,  $\vec{u} = [u_x, u_y, u_z] = u_x \hat{x} + u_y \hat{y} + u_z \hat{z}$  is the displacement vector,  $t$  is the time variable, and  $\vec{\nabla} = [\frac{\delta}{\delta x}, \frac{\delta}{\delta y}, \frac{\delta}{\delta z}] = \frac{\delta}{\delta x} \hat{x} + \frac{\delta}{\delta y} \hat{y} + \frac{\delta}{\delta z} \hat{z}$  is the nabla operator. The stress tensor,  $\vec{T}$ , is given by

$$\vec{T} = \begin{bmatrix} T_{xx} & T_{xy} & T_{xz} \\ T_{yx} & T_{yy} & T_{yz} \\ T_{zx} & T_{zy} & T_{zz} \end{bmatrix} \quad (3.2)$$

$$T_{xx} = (\lambda + 2\mu) \frac{\delta u_x}{\delta x} + \lambda \frac{\delta u_y}{\delta y} + \lambda \frac{\delta u_z}{\delta z} \quad (3.3)$$

$$T_{yy} = (\lambda + 2\mu) \frac{\delta u_y}{\delta y} + \lambda \frac{\delta u_x}{\delta x} + \lambda \frac{\delta u_z}{\delta z} \quad (3.4)$$

$$T_{zz} = (\lambda + 2\mu) \frac{\delta u_z}{\delta z} + \lambda \frac{\delta u_x}{\delta x} + \lambda \frac{\delta u_y}{\delta y} \quad (3.5)$$

$$T_{xy} = T_{yx} = \mu \frac{\delta u_y}{\delta x} + \mu \frac{\delta u_x}{\delta y} \quad (3.6)$$

$$T_{xz} = T_{zx} = \mu \frac{\delta u_z}{\delta x} + \mu \frac{\delta u_x}{\delta z} \quad (3.7)$$

$$T_{yz} = T_{zy} = \mu \frac{\delta u_z}{\delta y} + \mu \frac{\delta u_y}{\delta z}, \quad (3.8)$$

where  $\lambda$  and  $\mu$  are the Lamé coefficients and are given by:  $\lambda = \rho \times c_l^2 - 2 \times \mu$  and  $\mu = \rho \times c_t^2$ . The Lamé coefficients are material dependent parameters.

Three material parameters are of interest: the material density,  $\rho$ , and the longitudinal, and transverse, elastic wave velocities,  $c_l$ , and  $c_t$ , respectively. Since the phononic crystal is composed of two different materials, the value of the material parameters and Lamé coefficients are a function of position  $(x, y, z)$ .

By reverse substitution, each of the components of the elastic wave displacement vector may be expressed in terms of a partial differential equation:

$$\rho \frac{\delta^2 u_x}{\delta t^2} = \frac{\delta T_{xx}}{\delta x} + \frac{\delta T_{yx}}{\delta y} + \frac{\delta T_{zx}}{\delta z} \quad (3.9)$$

$$\rho \frac{\delta^2 u_y}{\delta t^2} = \frac{\delta T_{xy}}{\delta x} + \frac{\delta T_{yy}}{\delta y} + \frac{\delta T_{zy}}{\delta z} \quad (3.10)$$

$$\rho \frac{\delta^2 u_z}{\delta t^2} = \frac{\delta T_{xz}}{\delta x} + \frac{\delta T_{yz}}{\delta y} + \frac{\delta T_{zz}}{\delta z}. \quad (3.11)$$



## 3.2 Finite Difference Time Domain Solution to Elastic Wave Equation

Since it is proposed that a phononic band gap filter may only require a crystal that has a band gap in the longitudinal direction, the simulator only provides information about the propagation of the  $u_x$  (longitudinal) component of the elastic wave displacement vector. To compute  $u_x$ , the elastic wave equation must be solved for the components of the displacement vector. A second order accurate Finite Difference Time Domain (FDTD) numerical method was used to solve the elastic wave equation for the components of the displacement vector.

The phononic crystal is assumed to be infinitely thick in the  $\hat{z}$  direction. This means that the device is geometrically invariant in the  $\hat{z}$  direction. Hence, the derivative with respect to  $z$ , in Equations 3.3 to Equation 3.11, evaluates to zero.

Further, the crystal will only be excited in the longitudinal ( $\hat{x}$ ) direction, since it is only desired to determine the response of a phononic crystal to a transducer that provides excitation in the longitudinal direction. Due to the geometrical uniformity along the  $\hat{z}$  direction, no waves can become refracted into the  $\hat{z}$  direction. Thus:

$$u_z = 0. \quad (3.12)$$

Under these conditions, the set of equations needed to quantify elastic wave vibrations become:

$$\begin{aligned}
\rho \frac{\delta^2 u_x}{\delta t^2} &= \frac{\delta T_{xx}}{\delta x} + \frac{\delta T_{yx}}{\delta y} \\
\rho \frac{\delta^2 u_y}{\delta t^2} &= \frac{\delta T_{xy}}{\delta x} + \frac{\delta T_{yy}}{\delta y} \\
T_{xx} &= (\lambda + 2\mu) \frac{\delta u_x}{\delta x} + \lambda \frac{\delta u_y}{\delta y} \\
T_{yy} &= (\lambda + 2\mu) \frac{\delta u_y}{\delta y} + \lambda \frac{\delta u_x}{\delta x} \\
T_{xy} = T_{yx} &= \mu \frac{\delta u_y}{\delta x} + \mu \frac{\delta u_x}{\delta y}.
\end{aligned} \tag{3.13}$$

The two-dimensional simulation plane, in discrete space, is represented using discrete points. To maintain second order accuracy, the  $u_x$  and  $u_y$  components of the displacement vector are represented on two different grids (see Figure 3.1). The  $u_x$  component is computed at the set of points  $(l, m)$ , which form the integer-grid. The  $u_y$  component is computed at the set of points  $(l + \frac{1}{2}, m + \frac{1}{2})$ , which form the half-grid. Both  $l$  and  $m$  are integers. Figure 3.1 depicts both the integer-grid (represented by solid lines) and the half-grid (represented by dotted lines).

Time is also discrete in the simulator. The location in discrete time is represented by an integer,  $k$ , called the time step.

The distance between points on the integer-grid or half-grid is the spatial resolution of the simulation plane. The spatial resolution in the  $\hat{x}$  direction, and  $\hat{y}$  direction, are  $\Delta x$ , and  $\Delta y$ , respectively. The duration of time that elapses between time steps is the temporal resolution,  $\Delta t$ .

Distances between points on the integer-grid or half-grid may be described in terms of nodal units. Figure 3.1 illustrates the meaning of a nodal unit.

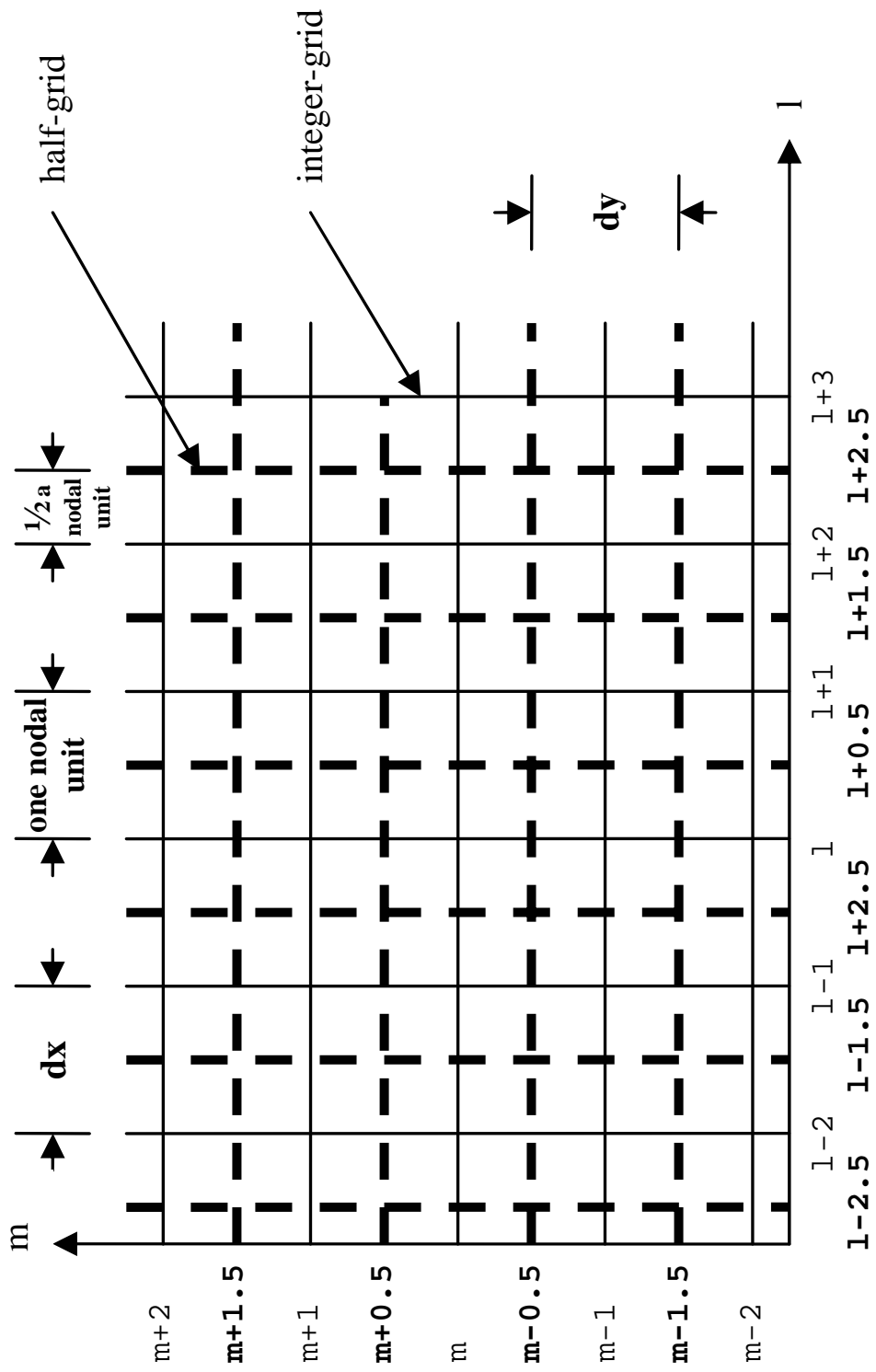


Figure 3.1: Discrete grid representation of discrete space.

The  $u_x$ , and  $u_y$ , component of the displacement vector are physically and temporally located at  $(l\Delta x, m\Delta y, k\Delta t)$ , and  $((l + \frac{1}{2})\Delta x, (m + \frac{1}{2})\Delta y, k\Delta t)$ , respectively. Where  $l \in [0, l_{max}]$ ,  $m \in [0, m_{max}]$ , and  $k \in [0, k_{max}]$  are integers.

Finite differences are used to approximate the derivatives in Equation 3.13. In particular, the space derivatives are approximated using central differences (*CD*), and the time derivative is approximated using forward differences (*FD*) and backward differences (*BD*) [14]:

$$\begin{aligned}
\frac{\delta u_i(l, m, k)}{\delta x} &\approx \frac{u_i(l + \frac{1}{2}, m, k) - u_i(l - \frac{1}{2}, m, k)}{\Delta x} && (CD) \\
\frac{\delta u_i(l, m, k)}{\delta y} &\approx \frac{u_i(l, m + \frac{1}{2}, k) - u_i(l, m - \frac{1}{2}, k)}{\Delta y} && (CD) \\
\frac{\delta u_i(l, m, k)}{\delta t} &\approx \frac{u_i(l, m, k + 1) - u_i(l, m, k)}{\Delta t} && (FD) \\
\frac{\delta u_i(l, m, k)}{\delta t} &\approx \frac{u_i(l, m, k) - u_i(l, m, k - 1)}{\Delta t} && (BD) \\
\frac{\delta^2 u_i(l, m, k)}{\delta t^2} &\approx \frac{u_i(l, m, k + 1) - u_i(l, m, k)}{\Delta t} \Bigg|_{u_i(l, m, k) = \frac{u_i(l, m, k) - u_i(l, m, k - 1)}{\Delta t}} \\
&= \frac{u_i(l, m, k + 1) - 2u_i(l, m, k) + u_i(l, m, k - 1)}{\Delta t^2}
\end{aligned} \tag{3.14}$$

where  $i \in [x, y]$ . If  $i = x$  then the  $(l, m)$  pairs correspond to the integer-grid. If  $i = y$  then the  $(l, m)$  pairs are replaced by  $(l + \frac{1}{2}, m + \frac{1}{2})$  pairs, which correspond to the half-grid.

Applying the finite difference approximations of Equation 3.14 to Equation 3.13, and letting  $k_{cur} = k + 1$ ,  $k_{pr1} = k$  and  $k_{pr2} = k - 1$  (where the subscript *cur* implies the current time step, the subscript *pr1* implies the previous time step, and so

forth) yields the equations of discrete space:

$$\begin{aligned}
u_x(l, m, k_{cur}) &= 2u_x(l, m, k_{pr1}) - u_x(l, m, k_{pr2}) \\
&+ \frac{\Delta t^2}{\rho(l, m)\Delta x} \left( T_{xx}(l + \frac{1}{2}, m, k_{pr1}) - T_{xx}(l - \frac{1}{2}, m, k_{pr1}) \right) \\
&+ \frac{\Delta t^2}{\rho(l, m)\Delta y} \left( T_{xy}(l, m + \frac{1}{2}, k_{pr1}) - T_{xy}(l, m - \frac{1}{2}, k_{pr1}) \right)
\end{aligned} \tag{3.15}$$

$$\begin{aligned}
u_y(l + \frac{1}{2}, m + \frac{1}{2}, k_{cur}) &= 2u_y(l + \frac{1}{2}, m + \frac{1}{2}, k_{pr1}) - u_y(l + \frac{1}{2}, m + \frac{1}{2}, k_{pr2}) \\
&+ \frac{\Delta t^2}{\rho(l + \frac{1}{2}, m + \frac{1}{2})\Delta y} \left( T_{xy}(l + 1, m + \frac{1}{2}, k_{pr1}) - T_{xy}(l, m + \frac{1}{2}, k_{pr1}) \right) \\
&+ \frac{\Delta t^2}{\rho(l + \frac{1}{2}, m + \frac{1}{2})\Delta x} \left( T_{yy}(l + \frac{1}{2}, m + 1, k_{pr1}) - T_{yy}(l + \frac{1}{2}, m, k_{pr1}) \right)
\end{aligned} \tag{3.16}$$

$$\begin{aligned}
&T_{xx}(l + \frac{1}{2}, m, k_{pr1}) = \\
&\left( \lambda(l + \frac{1}{2}, m) + 2\mu(l + \frac{1}{2}, m) \right) \frac{u_x(l + 1, m, k_{pr1}) - u_x(l, m, k_{pr1})}{\Delta x} \\
&+ \left( \lambda(l + \frac{1}{2}, m) \right) \frac{u_y(l + \frac{1}{2}, m + \frac{1}{2}, k_{pr1}) - u_y(l + \frac{1}{2}, m - \frac{1}{2}, k_{pr1})}{\Delta y}
\end{aligned} \tag{3.17}$$

$$\begin{aligned}
&T_{xx}(l - \frac{1}{2}, m, k_{pr1}) = \\
&\left( \lambda(l - \frac{1}{2}, m) + 2\mu(l - \frac{1}{2}, m) \right) \frac{u_x(l, m, k_{pr1}) - u_x(l - 1, m, k_{pr1})}{\Delta x} \\
&+ \left( \lambda(l - \frac{1}{2}, m) \right) \frac{u_y(l - \frac{1}{2}, m + \frac{1}{2}, k_{pr1}) - u_y(l - \frac{1}{2}, m - \frac{1}{2}, k_{pr1})}{\Delta y}
\end{aligned} \tag{3.18}$$

$$\begin{aligned}
& T_{xy}(l, m + \frac{1}{2}, k_{pr1}) = \\
& \left( \mu(l, m + \frac{1}{2}) \right) \frac{u_x(l, m + 1, k_{pr1}) - u_x(l, m, k_{pr1})}{\Delta y} \\
& + \left( \mu(l, m + \frac{1}{2}) \right) \frac{u_y(l + \frac{1}{2}, m + \frac{1}{2}, k_{pr1}) - u_y(l - \frac{1}{2}, m + \frac{1}{2}, k_{pr1})}{\Delta x}
\end{aligned} \tag{3.19}$$

$$\begin{aligned}
& T_{xy}(l, m - \frac{1}{2}, k_{pr1}) = \\
& \left( \mu(l, m - \frac{1}{2}) \right) \frac{u_x(l, m, k_{pr1}) - u_x(l, m - 1, k_{pr1})}{\Delta y} \\
& + \left( \mu(l, m - \frac{1}{2}) \right) \frac{u_y(l + \frac{1}{2}, m - \frac{1}{2}, k_{pr1}) - u_y(l - \frac{1}{2}, m - \frac{1}{2}, k_{pr1})}{\Delta x}
\end{aligned} \tag{3.20}$$

$$\begin{aligned}
& T_{xy}(l + 1, m + \frac{1}{2}, k_{pr1}) = \\
& \left( \mu(l + 1, m + \frac{1}{2}) \right) \frac{u_x(l + 1, m + 1, k_{pr1}) - u_x(l + 1, m, k_{pr1})}{\Delta y} \\
& + \left( \mu(l + 1, m + \frac{1}{2}) \right) \frac{u_y(l + 1.5, m + \frac{1}{2}, k_{pr1}) - u_y(l + \frac{1}{2}, m + \frac{1}{2}, k_{pr1})}{\Delta x}
\end{aligned} \tag{3.21}$$

$$\begin{aligned}
& T_{yy}(l + \frac{1}{2}, m + 1, k_{pr1}) = \\
& \left( \lambda(l + \frac{1}{2}, m + 1) + 2\mu(l + \frac{1}{2}, m + 1) \right) \frac{u_y(l + \frac{1}{2}, m + 1.5, k_{pr1}) - u_y(l + \frac{1}{2}, m + \frac{1}{2}, k_{pr1})}{\Delta y} \\
& + \left( \lambda(l + \frac{1}{2}, m + 1) \right) \frac{u_x(l + 1, m + 1, k_{pr1}) - u_x(l, m + 1, k_{pr1})}{\Delta x}
\end{aligned} \tag{3.22}$$

$$\begin{aligned}
T_{yy}(l + \frac{1}{2}, m, k_{pr1}) = & \\
\left( \lambda(l + \frac{1}{2}, m) + 2\mu(l + \frac{1}{2}, m) \right) & \frac{u_y(l + \frac{1}{2}, m + \frac{1}{2}, k_{pr1}) - u_y(l + \frac{1}{2}, m - \frac{1}{2}, k_{pr1})}{\Delta y} \\
+ \left( \lambda(l + \frac{1}{2}, m) \right) & \frac{u_x(l + 1, m, k_{pr1}) - u_x(l, m, k_{pr1})}{\Delta x}.
\end{aligned} \tag{3.23}$$

Due to the finite difference approximations used above, the central difference space derivatives have second order accuracy. However, these approximations have the result that the  $u_x$  and  $u_y$  components of the displacement vector are located at different points in space: the  $u_x$  component is on the integer-grid, while the  $u_y$  component is on the half-grid. To compute the  $u_x$  component on the half-grid, and the  $u_y$  component on the integer-grid, averaging may be used:

$$\begin{aligned}
u_x(l + \frac{1}{2}, m + \frac{1}{2}, k) = & \frac{1}{4} [u_x(l + 1, m + 1, k) + u_x(l + 1, m, k) \\
& + u_x(l, m + 1, k) + u_x(l, m, k)] \\
u_y(l, m, k) = & \frac{1}{4} [u_y(l + \frac{1}{2}, m + \frac{1}{2}, k) + u_y(l + \frac{1}{2}, m - \frac{1}{2}, k) \\
& + u_y(l - \frac{1}{2}, m + \frac{1}{2}, k) + u_y(l - \frac{1}{2}, m - \frac{1}{2}, k)].
\end{aligned} \tag{3.24}$$

To assist stability in the computations the CFL (Courant-Friedrichs-Lewy; sometimes Levy appears as Lewy) condition was applied:

$$\Delta t = \frac{\Delta t \text{ Numerator}}{c_{max}} \sqrt{\frac{1}{\Delta x^2} + \frac{1}{\Delta y^2}}, \quad (3.25)$$

where  $\Delta t \text{ Numerator} \in [0, 0.5]$  is chosen through experience. The phononic crystal will be composed of two materials. Each material is described by a longitudinal and transverse velocity. The variable  $c_{max}$ , of Equation 3.25, represents the largest of these velocities. The CFL condition is necessary, but not sufficient, for stability.

As described in Chapter 2, a plane wave source will be used to excite the phononic crystal. For the reasons discussed in Chapter 2, the continuous time domain signal that will be used at the source will be the Dirac Delta. The discrete time domain dual of the Dirac Delta is the Kronecker Delta:

$$\delta(k) = \begin{cases} 0 & k \neq 0 \\ 1 & k = 0 \end{cases}, \quad (3.26)$$

where  $k$ , an integer, is the time step.

### 3.3 The Absorbing Boundary Condition

When performing computations using a computer that has a finite amount of memory, the two-dimensional simulation plane must be truncated: the result is the finite two-dimensional simulation space depicted in Figure 3.2. As seen in Figure 3.2, the method utilized to truncate the simulation space was to apply an Absorbing Boundary Condition (ABC) and a Periodic Boundary Condition (PBC). Mur's first order



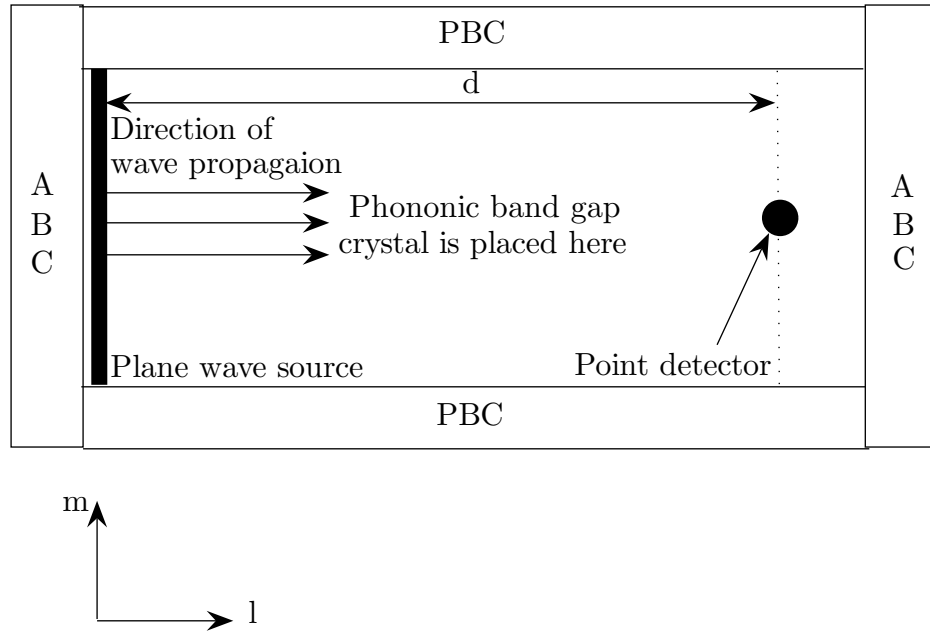


Figure 3.2: Simulation space.

ABC truncates the two-dimensional simulation plane in the  $\hat{x}$  direction, and is the topic of discussion in this section.

The ideal operation of the ABC is to ensure that the waves that impinge on the left, and right edges, of the simulation space, near the source, and detector, respectively, are absorbed (not reflected) and removed from the simulation space. The absence of reflected waves eliminates the possibility of interference patterns, which could cause erroneous simulation data. Moreover, as soon as the wave arrives at the ABC it is ideally removed from the simulation space, and so the same wave cannot be repeatedly detected by the detector.

The boundary formed by Mur's first order ABC is finite in width, and ensures that outgoing waves effectively travel out of the system. Applying an ABC at the boundary of a finite simulation space, thus, causes the finite simulation space to

mimic open (unbounded) space [15].

Mur's first order ABC truncates the two-dimensional simulation plane in the  $\hat{x}$  direction, and is given by [16], [17]:

$$\begin{aligned}
u_x(l_L, m, k_{cur}) &= u_x(l_L + 1, m, k_{pr1}) \\
&\quad + \frac{c_l(l_L, m)\Delta t - \Delta x}{c_l(l_L, m)\Delta t + \Delta x} [u_x(l_L + 1, m, k_{cur}) - u_x(l_L, m, k_{pr1})] \\
u_y(l_L + \frac{1}{2}, m + \frac{1}{2}, k_{cur}) &= u_y(l_L + \frac{1}{2} + 1, m + \frac{1}{2}, k_{pr1}) \\
&\quad + \frac{c_t(l_L + \frac{1}{2}, m + \frac{1}{2})\Delta t - \Delta x}{c_t(l_L + \frac{1}{2}, m + \frac{1}{2})\Delta t + \Delta x} \\
&\quad \times [u_y(l_L + \frac{1}{2} + 1, m + \frac{1}{2}, k_{cur}) - u_y(l_L + \frac{1}{2}, m + \frac{1}{2}, k_{pr1})] \\
u_x(l_R, m, k_{cur}) &= u_x(l_R - 1, m, k_{pr1}) \\
&\quad + \frac{c_l(l_R, m)\Delta t - \Delta x}{c_l(l_R, m)\Delta t + \Delta x} [u_x(l_R - 1, m, k_{cur}) - u_x(l_R, m, k_{pr1})] \\
u_y(l_R + \frac{1}{2}, m + \frac{1}{2}, k_{cur}) &= u_y(l_R + \frac{1}{2} - 1, m + \frac{1}{2}, k_{pr1}) \\
&\quad + \frac{c_t(l_R + \frac{1}{2}, m + \frac{1}{2})\Delta t - \Delta x}{c_t(l_R + \frac{1}{2}, m + \frac{1}{2})\Delta t + \Delta x} \\
&\quad \times [u_y(l_R + \frac{1}{2} - 1, m + \frac{1}{2}, k_{cur}) - u_y(l_R + \frac{1}{2}, m + \frac{1}{2}, k_{pr1})]
\end{aligned} \tag{3.27}$$

where  $l_L$ , and  $l_R$ , specify the location where the ABC is applied in the left, and right, side, respectively, of Figure 3.2. The phononic crystal lies within the ABC and PBC boundaries of the simulation space and so the  $c_l$  and  $c_t$ , in Equation 3.27, are the longitudinal and transverse wave velocities in the host material.

Mur's ABC is a differential-equation-based or "traditional" ABC [18]. The discrete form of a traditional ABC applies a "one-way boundary operator", which only permits outgoing waves [18]. As seen in Equation 3.27, the boundary computed by Mur's first order ABC is a function of points that are, at most, one nodal unit in from the boundary. For this reason Mur's ABC and the traditional ABC's are considered local [18] and so are computationally efficient. Arbitrary order ABC's may be utilized to increase accuracy of the ABC, however, higher order ABC's are less stable [18] and less computationally efficient.

For example, as stated Mur's first order ABC utilizes values one nodal unit in from the boundary, and also utilizes values from one time step back in time. In contrast, Mur's second order ABC, which is considered a highly absorbing boundary condition [17], utilizes values at one and two nodal units in from the boundary, and values one and two time steps back in time [17] and so is less computationally efficient.

Mur's first order ABC suffers from the problems of the other traditional ABC's, which generally assume that the incoming waves are plane waves or normally incident on the boundary [15]. In electromagnetic applications Mur's second and higher order ABC's reportedly produce fewer reflections, than Mur's first order ABC, for obliquely incident waves and grazing fields. Traditional ABC's also perform poorly in dispersive mediums since traditional ABC's assume a constant speed of propagation [18].

Traditional ABC's were commonly used due to the lack of a boundary condition which would eliminate reflections for waves impinging at arbitrary angles of

incidence [17]. Though Mur's second order ABC of 1981 decreased reflections for oblique angles of incidence, the next widely accepted alternative didn't come until 1994 when Berenger developed the Perfectly Matched Layer (PML) [15].

The PML is categorized as a material ABC (in contrast to a differential-equation based or traditional ABC). In 1996, Chew and Liu proved the existence of, and developed, a PML for simulations involving the elastic wave equation [19]. The PML has been proved to have zero reflections for waves of arbitrary frequency and angle of incidence.

The PML is only "perfect" in the continuous case and numerical errors develop in the discrete case. That said, in general the PML still performs better than Mur's ABC. However, due to its simplicity, computational efficiency, and widespread use, Mur's first order ABC was used in the development of the phononic band gap crystal simulator.

To account for the described short comings of Mur's first order ABC, a plane wave source has been used. The waves generated by the plane wave source are normally incident on the boundaries where Mur's first order ABC is applied.

In addition, Mur's first order ABC is applied near a homogeneous region in which the elastic wave velocity is a constant. The homogeneous region also separates the boundary at which Mur's first order ABC is applied from the phononic crystal. Thus, the waves that are reflected off the crystal, must travel through the homogeneous region before they arrive at the ABC. The ABC can be thought of as being in the far-field of the scattering crystal, and so the reflected waves may be approximated as plane waves at the location of the ABC [20].

The homogeneous region also ensures that the ABC is far enough from the crystal so that the ABC will not remove elastic waves that are important in computing the crystal's response [20].

Finally, even with all the aforementioned provisions, reflections will still be generated at Mur's first order ABC. Having a large homogeneous region ensures that it will take a finite amount of time for the first set of waves, which emerge from the crystal, to travel past the detector, be reflected at Mur's ABC, and travel back to the detector. By locating the detector in the middle of the homogeneous region, far from the boundary at which the ABC is located, the initial set of detected elastic waves will not include any reflected waves. The first part of the transient response is essential in determining the frequency response of the crystal and so it is crucial that the first part of the transient response only be composed of the waves that came directly out of the crystal (and not reflected waves generated at the boundaries of the simulation space).

If the simulation is stopped before the reflected waves travel back to the detector, then the waves reflected by Mur's first order ABC will not be detected again. By choosing the total width of the homogeneous regions to be four, the simulation is being optimized to minimize simulation time and not simulation error since it is likely that some reflected waves will pass by the detector more than once. If the homogeneous region were chosen large enough, an ABC would not even be required, however, simulation time would become impractically large.

### 3.4 The Periodic Boundary Condition

PBC's are applied to truncate the two-dimensional simulation plane in the  $\hat{y}$  direction:

$$\begin{aligned}
 u_x(l, m_B, k_{pr1}) &= u_x(l, m_B, k_{pr1}) \\
 u_y(l + \frac{1}{2}, m_B + \frac{1}{2}, k_{pr1}) &= u_y(l + \frac{1}{2}, m_B + \frac{1}{2}, k_{pr1}) \\
 u_x(l, m_T, k_{pr1}) &= u_x(l, m_T, k_{pr1}) \\
 u_y(l + \frac{1}{2}, m_T, k_{pr1}) &= u_y(l + \frac{1}{2}, m_T, k_{pr1})
 \end{aligned} \tag{3.28}$$

where  $m_B$ , and  $m_T$ , specify the location of the PBC at the bottom, and top, of Figure 3.2, respectively.

An ideal crystal is infinitely periodic. The PBC ensures that the finite simulation space mimics an infinitely periodic crystal in the  $\hat{y}$  direction.

Figure 3.3 illustrates the operation of the PBC equations (Equation 3.28). In Figure 3.3 a computational domain that measures 3[*nodal units*] by 4[*nodal units*] is depicted surrounded by the ABC and PBC domains. Each integer-grid node is illustrated by a square box. The ABC domain is not currently of interest.

As may be seen in Figure 3.3, the  $u_x$  component at the top, and bottom, edges of the computational domain are relocated by the PBC to the bottom, and top, PBC domain, respectively. Thus, a wave traveling into the top edge of the computational domain is relocated and appears outside the computational domain in the bottom PBC domain. Similarly, a wave traveling into the bottom edge of the computational

domain is relocated and appears outside the computational domain in the top PBC domain.

Since the relocating operation of the PBC removes components of  $u_x$  from the computational domain and relocates them to a location outside the computational domain (in the PBC domain), it may not be immediately obvious that the relocated component of  $u_x$  will even have an impact on the future computations that occur in the computational domain. Moreover, it is not obvious that a wave traveling into the top edge (or bottom edge) of the computational domain will reenter the computational domain after being relocated to the bottom (or top) PBC domain. For the PBC operation to be successful the following condition is required.

The condition required by the PBC is that the component of  $u_x$  that was relocated to PBC domain must be analytically linked into the computational. This means that the  $u_x$  at the edge of the computational domain must be a function of the  $u_x$ 's that are located in the PBC domain.

The  $u_x$ 's at the edge of the computational domain are located one nodal unit away from the  $u_x$ 's in the PBC domain. Hence, the PBC requires that  $u_x$  at some location  $(l, m)$  must be a function of  $u_x$ 's that are located one nodal unit away from  $(l, m)$ . Turning to Figure 3.4, it may be seen that this is indeed the case.

Figure 3.4 illustrates that Equation 3.15 for  $u_x(l, m, k_{cur})$  is a direct function of the components of the stress tensor at time  $k_{pr1}$  and the value of  $u_x(l, m, k)$  at both  $k = k_{pr1}$  and  $k = k_{pr2}$ . The components of the stress tensor are physically located half a nodal unit away from  $(l, m)$ . Figure 3.4 also illustrates that the components of the stress tensor, Equations 3.17 to Equation 3.20, are a function of the  $u_x$  at





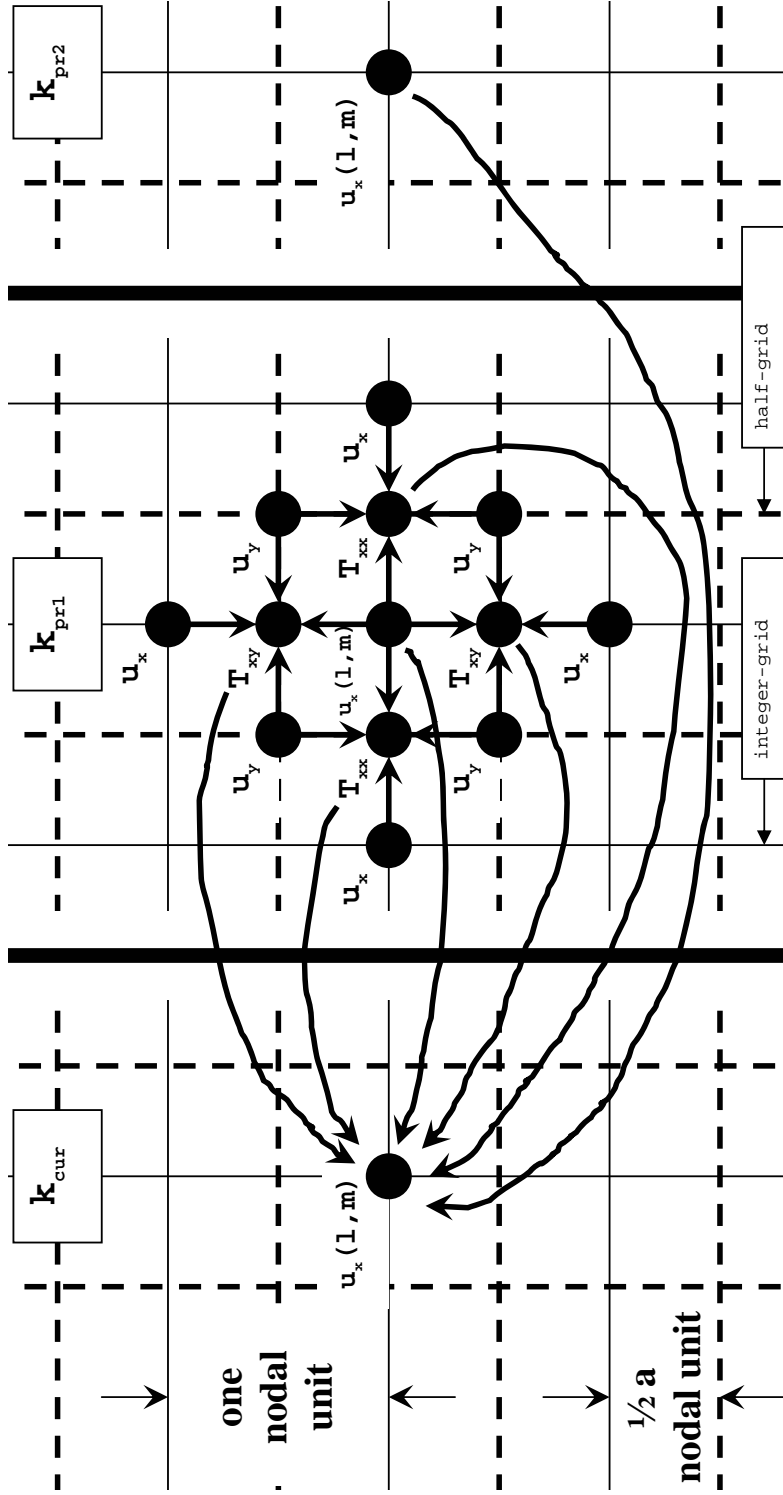


Figure 3.4: Map of inputs to  $u_x$  (Equation 3.15) at time  $k_{cur}$ .

$k_{pr1}$ : these  $u_x$ , however, are located one nodal unit away from  $(l, m)$ . In other words, the  $u_x$  at  $k_{cur}$  are a function of  $u_x$  at  $k_{pr1}$ :  $u_x(k_{cur}) = f(u_x(k_{pr1}))$ , where the  $u_x(k_{pr1})$  are located one nodal unit away from location  $(l, m)$ . Thus, the function for  $u_x$  at  $(l, m)$ , and  $u_x$  one nodal unit away from  $(l, m)$ , are analytically linked through the components of the stress tensor.

Hence, the top, and bottom, edges of the computational domain are analytically linked to the bottom, and top, PBC domains, respectively. A wave traveling into the upper edge of the computational domain is relocated to the bottom PBC domain, and will then emerge from the bottom edge of the computational domain, and continue traveling up through the crystal. It is this same analytic feature of the discrete equations for  $u_x$  and  $u_y$  that also results in wave propagation within the computational domain. Similarly, waves traveling into the bottom edge of the computational domain are relocated to the top PBC domain and emerge from the upper edge of the computational domain. The same arguments hold for the  $u_y$  component of the displacement vector.

In conclusion, the proper operation of the PBC will ensure that a wave traveling toward the edge of the simulation space where the PBC is applied (the top and bottom edges in Figure 3.2) will emerge from the opposite edge and continue to travel through the periodic crystal. Thus, the PBC causes the simulation space to wrap around on itself in the  $\hat{y}$  direction. As in Figure 3.5, the two-dimensional simulation space becomes a cylinder.

Figure 3.5 illustrates that the combined action of the ABC and PBC result in a cylindrical simulation space, which is effectively infinitely long in the  $\hat{x}$  direction.

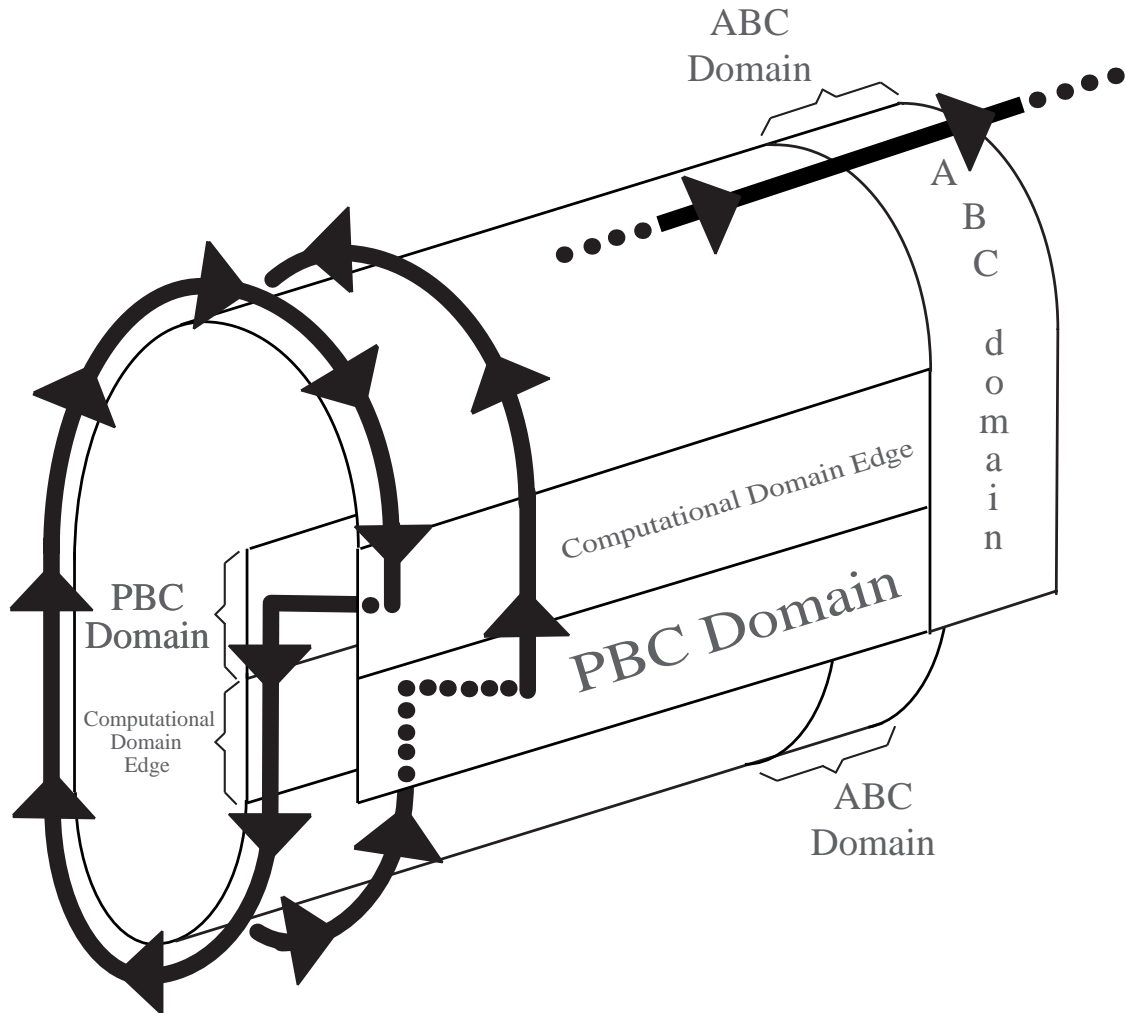


Figure 3.5: Illustration of how ABCs and PBCs act to make the two-dimensional simulation space into an infinitely long cylindrical simulation space. The arrows indicate the path of elastic wave propagation. The left edge ABC domain is not shown.

Waves traveling into the ABC domain are absorbed and so effectively travel to infinity. Waves traveling into the PBC domain, emerge coming out of the opposite edge and continue to travel through the periodic phononic crystal. Hence, the application of the PBC effectively provides infinite periodicity in the  $\hat{y}$  direction.

## 3.5 Simulator

In Section 3.2, the FDTD numerical method was applied to solve the elastic wave equation in discrete time and discrete space. The discrete form of a Dirac Impulse, the Kronecker Delta, was also introduced in Section 3.2. In Section 3.3 and Section 3.4, a discrete version of the ABCs and PBCs, respectively, was introduced. Hence, a computer program may be written to simulate the impulse response of an elastic media (namely a phononic crystal) that is bounded by boundary conditions as illustrated in Figure 3.2.

### 3.5.1 Simulator Inputs

Three text files are input into the simulator:

1. `architecture.txt`,
2. `device.txt`, and
3. `source.txt`.

A discussion of these three text files follows.

### The `architecture.txt` File

The discussion begins with `archutecture.txt`, which defines phononic crystal architecture, meaning the location of the host and inclusion materials. The phononic crystal is represented using a two-dimensional matrix:

$$medium(l, m) = \begin{cases} 1, & \text{if the host material is present at node } (l, m) \\ 2, & \text{if the inclusion material is present at node } (l, m) \end{cases} . \quad (3.29)$$

Only the points at which the inclusion material is present need to be input into the simulator (if the inclusion material is not present at location  $(l, m)$  then the host material is present there). The coordinate pair that represents the points at which the inclusion material is present are stored in the `architecture.txt` file.

With the phononic crystal architecture defined in `architecture.txt`, next the material parameters, data regarding the number and size of inclusions in the crystal, the simulation duration, and the value of  $\Delta t Numerator$  are input into the simulator via the `device.txt` file.

### The `device.txt` File

The `device.txt` file defines 11 parameters:

1. host material density,  $\rho_{host}$ ; units:  $[g/cm^2]$ ,

2. host material longitudinal velocity,  $c_{l\_host}$ , (velocity in the  $\hat{x}$  direction); units:  $[cm/s]$ ,
3. host material transverse velocity,  $c_{t\_host}$ , (velocity in the  $\hat{y}$  direction); units:  $[cm/s]$ ,
4. inclusion material density,  $\rho_{inclusion}$ ; units:  $[g/cm^2]$ ,
5. inclusion material longitudinal velocity,  $c_{l\_inclusion}$ , (velocity in the  $\hat{x}$  direction); units:  $[cm/s]$ ,
6. inclusion material transverse velocity,  $c_{t\_inclusion}$ , (velocity in the  $\hat{y}$  direction); units:  $[cm/s]$ ,
7. the filters dimensions,  $N_x$ ; units: number of unit cells, or  $[lattice\ constants]$ , in the  $\hat{x}$  direction,
8. the filters dimensions,  $N_y$ ; units: number of unit cells, or  $[lattice\ constants]$ , in the  $\hat{y}$  direction,
9. the lattice constant,  $acell_{NODES}$ ; units:  $[nodal\ units]$ ,
10. the simulation duration,  $k_{max}$ ; units:  $[time\ steps]$ , and
11. the temporal resolution coefficient,  $\Delta t_{Numerator} \in [0, 0.5]$ .

The host and inclusion material parameters  $\rho$ ,  $c_l$ , and  $c_t$  for all devices that will be studied in this thesis are tabulated in Appendix A. The phononic crystal structure is characterized using three parameters:  $N_x$ ,  $N_y$  and  $acell_{NODES}$ , which are described

in Figure 3.6. The last two parameters contained in the `device.txt` file are  $k_{max}$  and  $\Delta t_{numerator}$ .

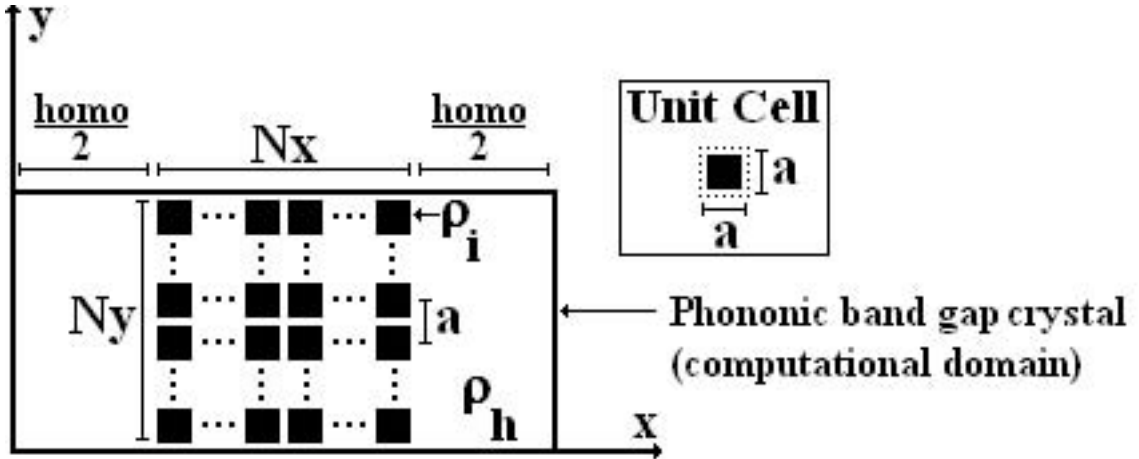


Figure 3.6: Illustration of the parameters that characterize the structure of a phononic crystal. The following abbreviations are applied in the figure: the lattice constant,  $acell_{NODES}$ , has been abbreviated as  $a$ ; the total width of the homogeneous region,  $homowIDTH$ , has been abbreviated as  $homo$ ; the inclusion material density,  $\rho_{inclusion}$ , has been abbreviated as  $\rho_i$ ; the host material density,  $\rho_{host}$ , has been abbreviated as  $\rho_h$ . The unit cell is depicted as a square inclusion for illustration purposes only.

A discussion on how to deduce which materials may be utilized in the simulator is in order. The discrete equations provide insight into the materials that may be utilized in the simulator. The discrete equations for  $u_x$  and  $u_y$  (Equation 3.15 and Equation 3.16) are inversely proportional to the density of the medium through the  $\frac{(\Delta t)^2}{\rho}$  factor. This eliminates the possibility of simulating a vacuum (which has a material density of approximately zero); however, an elastic wave cannot be present in a vacuum.

Low density materials, such as air, which has a density of  $0.001225 [g/cm^3]$  (see Appendix A), may cause convergence problems. The known solution for dealing

Table 3.1: Typical values of  $\Delta t$  that provide good convergence for various systems.

Materials (Host-Inclusion)	Inclusion geometry	$\Delta t Numerator$	$\Delta x = \Delta y$ [cm]	$\Delta t$ [ns]
Aluminium-Air	Circle	0.008	0.0093	0.0818562926
Aluminium-Mercury	Circle	0.100	0.0091	0.997623539
Aluminium-Mercury	Fractal	0.100	0.0035	0.383701376
Silicon-Air	Circle	0.010	0.0100	0.095041231
Water-Perspex	Layer	0.010	0.0329	1.57187929

with low density materials is to decrease  $\Delta t Numerator$  or  $\Delta x(= \Delta y)$ . By decreasing  $\Delta t Numerator$  or  $\Delta x(= \Delta y)$ ,  $\Delta t$  is decreased and this compensates for the low density that appears in the  $\frac{(\Delta t)^2}{\rho}$  factor of the equations for  $u_x$  and  $u_y$  (Equation 3.15 and Equation 3.16).

Typical values for  $\Delta t Numerator$ , and the resultant value of  $\Delta t$ , which provide good convergence for various phononic crystals are listed in Table 3.1; these values were obtained through experience (trial and error). The general trend is that  $\Delta t$  is within a factor of 10 of 1[ns] in magnitude. Moreover, the value of  $\Delta t$  that ensures convergence may depend on both the materials utilized and the inclusion geometry.

Figure 3.6 depicts the two equal sized homogeneous regions that lie to the left and right of the phononic crystal. The total width of the homogeneous regions,  $homo_{WIDTH}$ , was fixed at four lattice constants for all simulations (see Section 3.3). This results in left and right homogeneous regions which are each two lattice constants wide. From Figure 3.6, this means that the source is located in a homogeneous region that is two lattice constants wide, and the detector is located in a homogeneous region that is two lattice constants wide. The functionality of the



homogeneous regions was discussed in detail in Section 3.3.

The method of choosing  $k_{max}$  is detailed in Section 3.6.

The dimensions of the phononic crystal, measured in the number of inclusions in the  $\hat{x}$  direction,  $N_x$ , and  $\hat{y}$  direction,  $N_y$ , are through trial and error. Due to the complexity of describing the response of a phononic crystal analytically, design and development generally consists of trial and error.

The last simulation parameter defined in `device.txt` is the lattice constant,  $acell_{NODES}$ , which is measured in nodal units. The lattice constant,  $acell_{NODES}$ , is set during the design of the unit cell fill factor.

The fill factor for a two-dimensional unit cell is the inclusion area divided by the total unit cell area. To determine  $acell_{NODES}$ , the phononic crystal designer first chooses the inclusion geometry. The inclusion is then drawn on a discrete grid, such as that in Figure 3.1. Extra padding is added around the inclusion to achieve the desired fill factor. Since, the two-dimensional phononic band gap crystal simulator is designed to simulate only square lattices the unit cell is always a square. The width of the square box that contains the inclusion and the extra padding is the lattice constant,  $acell_{NODES}$ , which has the units [*nodal units*]. The physical length of the lattice constant is computed as follows:

$$acell_{CM}[cm] = acell_{NODES}[nodal\ units] \times \Delta x[cm/nodal\ unit]. \quad (3.30)$$

### The source.txt File

The final input to the simulator is the `source.txt` file, which contains the discrete time domain amplitude data of the signal that is generated by the plane wave source.

The sampling period,  $\Delta t$ , is computed using Equation 3.25 and obeys Nyquist's Law. Nyquist's Law states that in order to accurately represent a continuous time signal, in the discrete time domain, the continuous time signal must be sampled with a sampling period,  $\Delta t$ , that is, at most, half of the period of the highest frequency component in the continuous time signal. That is:  $\Delta t \leq \frac{1}{2}T_{min}$ , where  $T_{min}$  is the period of the highest frequency component in the signal that is being represented in the discrete time domain. From Table 3.1, typically  $\Delta t \approx 1[ns]$ , so typically  $T_{min} = 2 \times \Delta t = 2[ns]$ . Thus, theoretically, the frequency of the highest frequency component that can typically be accurately represented is  $f_{max} = 1/T_{min} = 1/2ns = 500[MHz]$ . A frequency of  $500[MHz]$  is much higher than any frequency that will be examined.

As stated in Section 3.2, a Kronecker Delta will be used as the plane wave source signal. The Kronecker Delta was represented by nine zeros, the value  $10^{-6}$ , followed by 1,250 zeros, that is  $source(k) = [0\ 0\ 0\ 0\ 0\ 0\ 0\ 0\ 0\ 10^{-6}\ 0\ 0\ 0\dots 0]$ . Hence, the size of the  $source(k)$  vector is 1260 time steps, where  $k$  is the time step. Most simulations run for over 40,000 time steps, which is more than 1,260 time steps, and so during the simulation the end of the source vector will be reached. Two source models were experimented with to handle the condition of reaching the end of the source vector.

The first model utilized was referred to as the "floating source model": after the end of the source array was reached, the simulator allowed the crystal to undergo a natural response (the source is essentially detached from the crystal, and the crystal is allowed to vibrate, or "float", freely). The second model utilized was termed the "zero padded source model": after the end of the source array was reached, the amplitude of vibrations at the source location is fixed at zero for the remainder of the simulation.

The disadvantage of the floating source is that the crystal is free to vibrate and eventually the simulation may diverge beginning at the source end. Eventually the diverging vibrations travel to the detector end, and so the simulation must be stopped prematurely so that the vibrations at the detector do not diverge. The zero padded source does not suffer from this problem. Thus, if divergence due to the use of a floating source is a problem, then a zero padded source should be used.

For example, in the study of wave guides it is useful to generate surface plots of the amplitude of vibration versus position in the crystal. When utilizing a floating source, the amplitude of the vibrations at the source end will eventually diverge, and the information on the surface plot becomes unintelligible. Hence, in the study of wave guides the use of a zero padded source is recommended.

In addition, the simulated frequency response was found to be dependent on whether a floating or zero padded source was implemented. In one instance, the use of the zero padded source caused high frequency components to become suppressed. The two-dimensional phononic band gap crystal simulator, developed to produce the results presented in this thesis, implemented a floating source.

Returning to the discussion of the Kronecker Delta: the above stated representation of the Kronecker Delta works well in practice in that the DFT of a displacement versus time signal that was detected near the input source was observed to have a band limited "white" spectrum.

The transient response (displacement versus time signal) of an aluminum host material at a point just beside the Kronecker Delta plane wave source is depicted in Figure 3.7. Though the amplitude of the induced Kronecker Delta was  $10^{-6}[cm]$ , the amplitude of the transient response is on the order of  $10^{-8}[cm]$  indicating the presence of propagation losses. The curve represented by the dotted line in Figure 3.7 is the function  $\frac{2.5 \times 10^{-9}}{44400000(t - 0.75 \times 10^{-6})} + 0.4 \times 10^{-8}$ . Hence, the amplitude of vibrations decay exponentially with respect to time.

Figure 3.8 depicts the DFT of the transient response of Figure 3.7. During the simulation used to generate Figure 3.7 and Figure 3.8, the temporal resolution was set to  $\Delta t = 0.997623539[ns]$ . The spectrum of the signal induced, by the Kronecker Delta source, into the aluminium host is a constant up to about  $20[MHz]$ . A frequency of  $20[MHz]$  is approximately 10 times higher than the highest frequency that will be of interest. As  $\Delta t$  decreases the frequency up to which the DFT remains a constant increases.

Thus, in practice, the above stated Kronecker Delta implementation, used in conjunction with the floating source model, is a satisfactory approximation of an ideal Kronecker Delta. During each simulation, the DFT of the source signal detected at a point adjacent to the source was checked to ensure that the induced signal had a 'white' spectrum in the frequency regime that would be of interest.

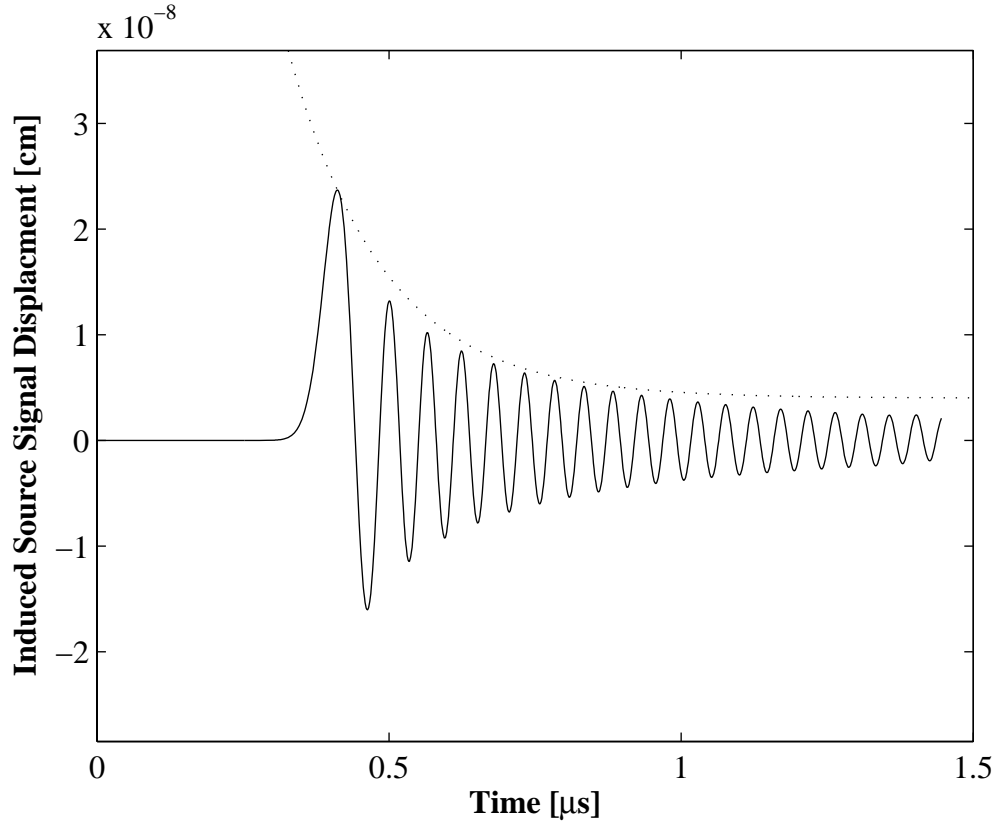


Figure 3.7: The transient response of the source signal induced into the phononic crystal as detected at a location just beside the plane wave source ( $\Delta t = 0.997623539[ns]$ ). The envelope of the transient response appears to be an exponentially decaying function: the dotted curve is given by  $\frac{2.5 \times 10^{-9}}{44400000(t - 0.75 \times 10^{-6})} + 0.4 \times 10^{-8}$ .

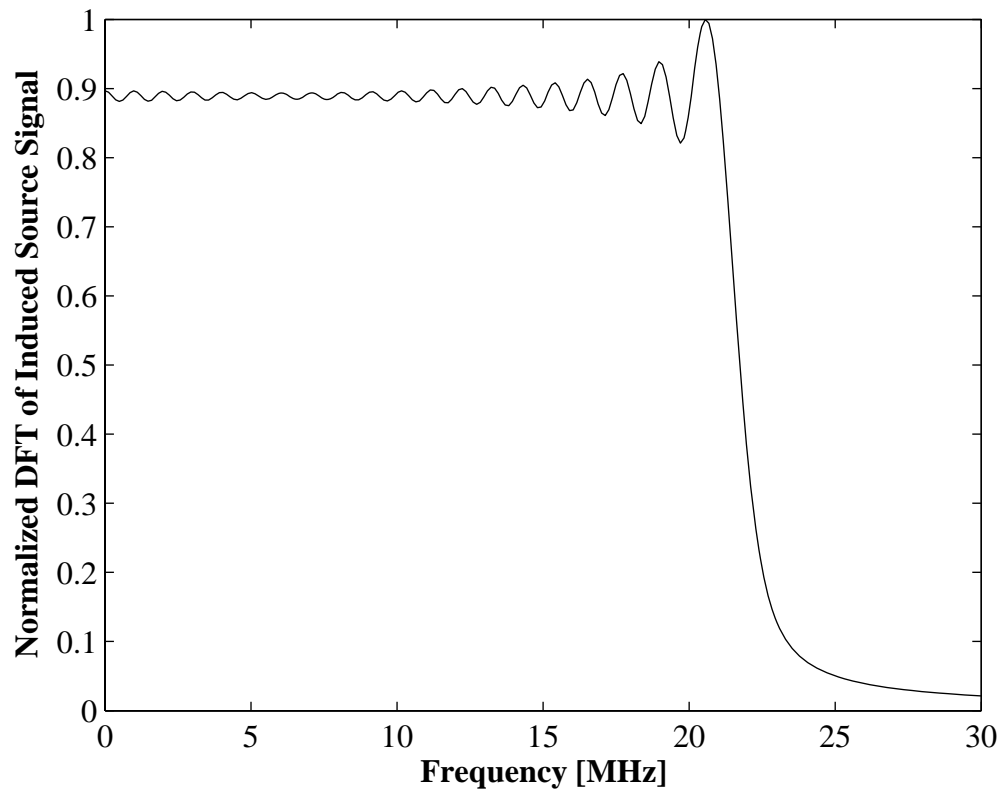


Figure 3.8: The discrete fourier transform of the source signal of Figure 3.7.

### 3.5.2 Source and Detector Locations

The plane wave source was chosen to be located two nodal units in from the left ABC domain, and is parallel to the left ABC domain as in Figure 3.2. Section 3.3 describes why the plane wave source was used and applied parallel to the ABC domain. The plane wave source generates waves in two directions: one wave is directed toward the phononic crystal and the other wave is directed in the opposite direction toward the left ABC domain. By having the plane wave source very close to the left ABC domain the plane wave that is directed toward the left ABC domain is immediately absorbed and removed from the simulation, leaving only the plane wave that was directed toward the phononic crystal.

The detector was chosen to be a point detector. The point detector was located directly in the middle of the right homogeneous region. Since the right homogeneous region is two lattice constants wide, the point detector is located one lattice constant from the right ABC domain. The choice of point detector location is justified in Section 3.3.

Another choice for the point detector location may have been away from the center of the right homogeneous region. Such a point detector location may be chosen if it is desired to eliminate symmetry in the simulation, or to eliminate line of sight from the source to the detector. An alternative to a point detector may be to average the vibrations detected over the area of a unit cell [21].

Changing the plane wave source and point detector locations was found to change the overall amplitude of the magnitude response. However, the ability of the simulator to predict band gap location appeared to be relatively independent

of the source and detector locations.

### 3.5.3 Program Flow

An overview of the two-dimensional phononic band gap crystal simulator program flow is provided in Figure 3.9.

As may be seen in Figure 3.9, upon execution of the program, variables are declared and text files are opened for data input and output. The data contained in the `source.txt` file is read into memory and used to initialize variables of the FDTD routine. Data that is contained in the `device.txt` file is used to compute the Lamé coefficients and the CFL condition, and is input into the FDTD routine along with the Lamé coefficients and the CFL condition. The data contained in the `architecture.txt` file is input into the FDTD routine and is used to compute the fill factor of the unit cell. Lastly, several simulation parameters are written to the `simparametes.txt` file so that the operation of the simulator can be verified.

The block that contains the FDTD numerical method block and boundary condition blocks, is of primary interest and will be referred to as the FDTD block. The computer code represented by the FDTD block is described in Figure 3.10.

The FDTD block consists of three loops: one time loop and two space loops. The time loop cycles through discrete time from  $k = 0 \dots k_{max}$ . The two space loops are nested in the time loop. The space loops step through discrete space for  $l = 0 \dots l_{max}$  and  $m = 0 \dots m_{max}$ .

Upon entering the loop that steps through discrete time, the simulator checks to see if the current time step is less than, or equal to, the length of the source



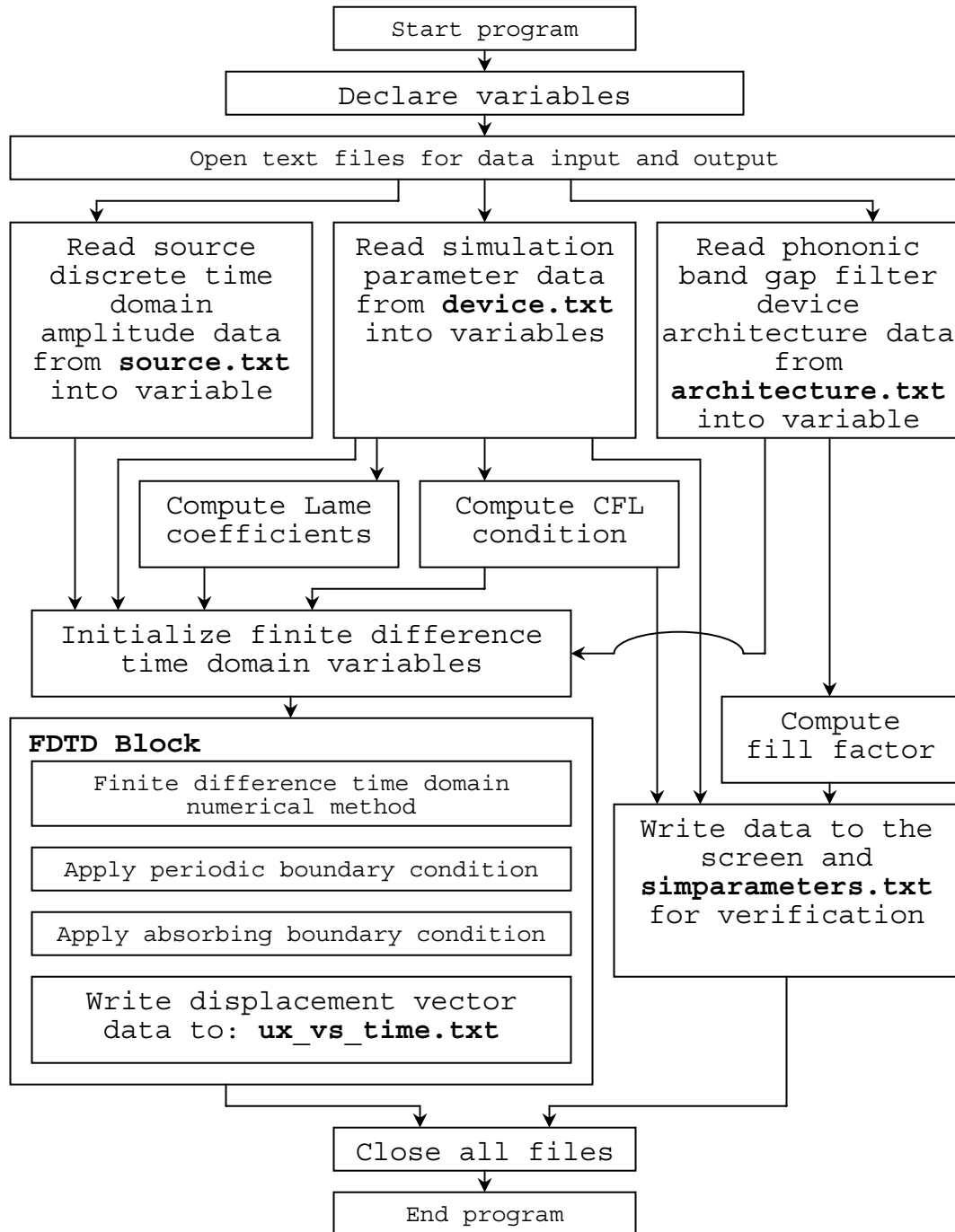


Figure 3.9: Overall program flow of the phononic band gap crystal simulator.

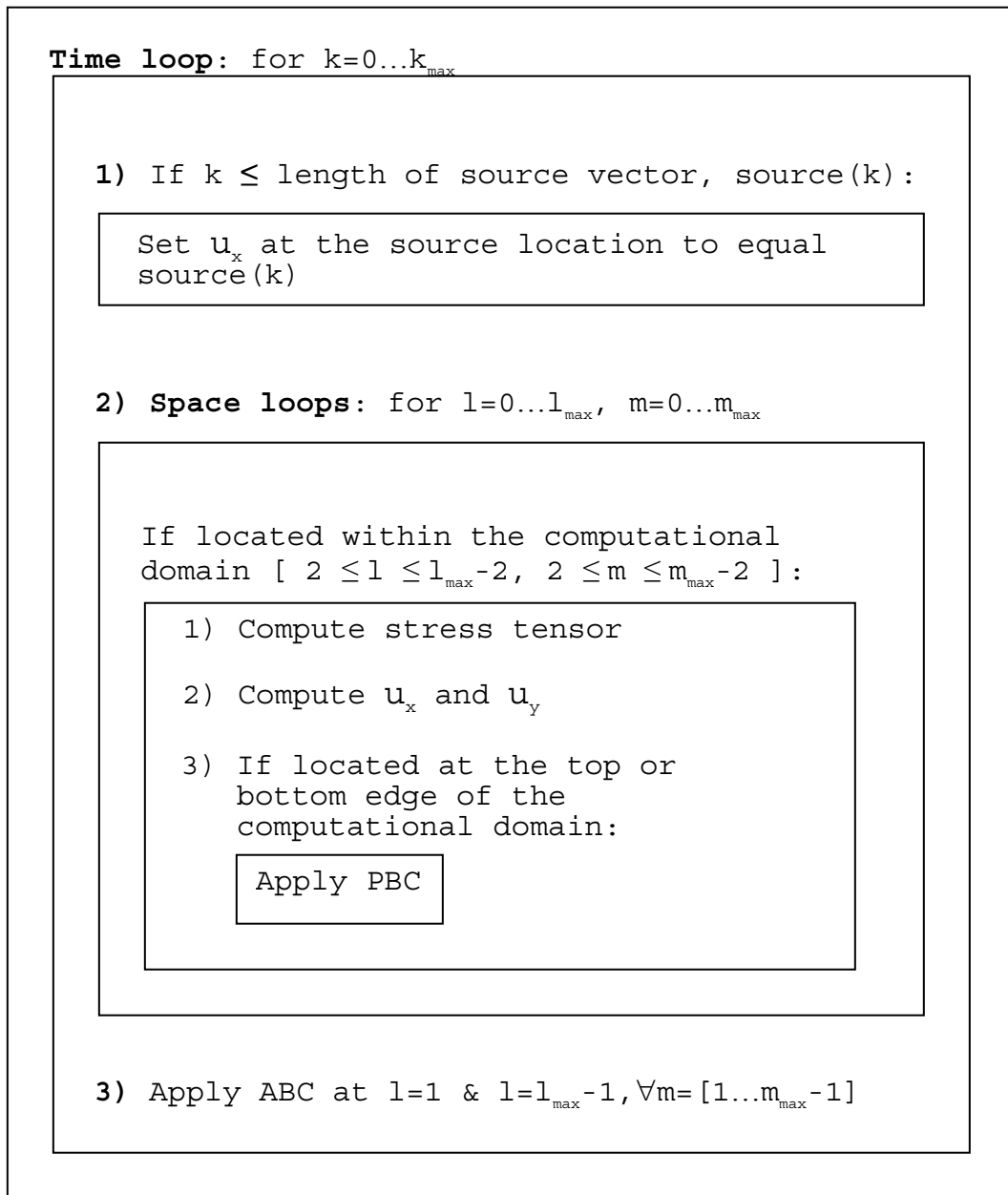
**FDTD Block**

Figure 3.10: Program flow of the FDTD block of the phononic crystal simulator.

vector,  $source(k)$ . The amplitude of vibrations at the location of the plane wave source are set equal to  $source(k)$  or the floating source model of Section 3.5.1 is applied.

The simulator then enters the two loops that step through discrete space. Upon entering the loop that steps through discrete space, the simulator checks if it is currently located within the computational domain: if this condition is true the components of the stress tensor, and  $u_x$  and  $u_y$ , are computed. Then the simulator checks if it is currently located at the top or bottom edge of the computational domain: if this condition is true the PBC is applied. Applying the PBC in such a fashion was found to provide good convergence (the alternative is to apply the PBC along with the ABC outside of the space loops). The space loops step through all of discrete space.

Finally, the ABC is then applied and the simulator proceeds to the next time step.

### 3.6 On Choosing $k_{max}$

This section discusses the process utilized to choose the simulation duration, which is defined as the number of time steps signified by  $k_{max}$ .

The lower bound on  $k_{max}$  is provided by considering that it will take a finite amount of time for elastic waves to travel from the source to the detector. The simulation should continue for a short period of time after elastic waves arrive at the detector so that enough non-zero data is captured.

The upper bound on  $k_{max}$  is determined such that the amount of error that accumulates is negligible. There exist three sources of simulation error: (1) computational errors due to the limited precision of data stored in computer memory, (2) numerical errors due to the discrete approximations of the FDTD numerical method, and (3) error caused by waves that reflect off of Mur's first order ABC. Computational errors are difficult to eliminate. However, through proper choice of  $k_{max}$ , numerical errors and the errors generated by reflected waves can be reduced.

First,  $k_{max}$  is chosen to be large enough such that simulation proceeds until the simulation data becomes erroneous: this was found to be 100,000[time steps] to 200,000[time steps] for the devices discussed in this thesis. Then, the Discrete Fourier Transform (DFT) of the first  $k$  time steps is taken, for  $k \in [40,000 \ 50,000 \dots k_{max}]$ . Generally, the DFT data will look radically different for each  $k_{max}$ . Once in the frequency domain, it is abundantly clear when the simulation has proceeded for too long.

The largest  $k$  for which the data appears to be representative of physical phenomenon is chosen to be the new  $k_{max}$  and the remainder of the data is discarded. The  $k_{max}$  may also be chosen to produce the best match with published data may be utilized. The simulation data that should be utilized is usually the data from time  $t = 0$  to some time  $t_{max}$ . The time  $t_{max}$  is determined through trial and error, and corresponds to the new  $k_{max}$ .

After some time, elastic waves are reflected off of the boundaries where Mur's first order ABC is implemented, and may travel back to the detector to be detected for a second time. It is desired to detect the elastic waves that emerge from the

crystal only once. For this reason, very large homogeneous regions may be utilized in association with Mur's first order ABC. However, in the two-dimensional phononic band gap crystal simulator, two relatively small homogeneous regions (each having a width of two lattice constants) were implemented. The consequence of implementing a small homogeneous region is that it is very likely that elastic waves will reflect off of Mur's first order ABC and travel back to the point detector to be detected again.

In the absence of published data, for example when studying a new phononic crystal, experience is then used to examine the DFT data and determine the optimal value of  $k_{max}$ .

Experience may be utilized to identify features of the DFT that are characteristic of a physical response to the given input. Such features may include pass band ripple (smooth rolling Gibbs type oscillations), or a stop band (band gap) that is consistently present in the frequency response for several different  $k_{max}$ . If a stop band is present for several  $k_{max}$ , there is a high probability that the stop band is real and not an artifact of simulation errors. All the studied systems also possess a pass band at zero frequency.

The optimal  $k_{max}$  is stated for each simulation that will be presented.

### 3.7 Verification of Simulator Operation

The operation of the phononic crystal simulator was verified as follows:

1. first, a reference simulation, in which no boundary conditions are applied, was

executed;

2. next, the operation of the boundary conditions was verified;
3. while examining the operation of the boundary conditions the induced elastic waves were observed to ensure that the waves travel across the computational domain in a physically meaningful fashion; finally
4. simulations were performed to duplicate published data.

In the reference simulation a Gaussian pulse is launched toward a boundary of the simulation space where no boundary condition was applied. Five snapshots, taken at five different moments in time, of the Gaussian pulse traveling toward the boundary are depicted in Figure 3.11. The amplitude of the induced Gaussian pulse was  $10^{-6}[cm]$ .

In the fourth snapshot of Figure 3.11, a non-physical gain is observed since the amplitude of the Gaussian pulse increases to above  $10^{-6}[cm]$ . The phononic crystal is a passive device and so a gain is not physically possible. Then, in the fifth snapshot, the Gaussian pulse is reflected from the boundary. Both the non-physical gain and the reflected pulse are undesired.

Simulations that test the operation of the implemented ABC and PBC will now be discussed, followed by simulations that reproduce published data.

### 3.7.1 The Absorbing Boundary Condition

Turning attention to Figure 3.12, a Gaussian pulse with an amplitude of  $10^{-6}[cm]$  is depicted as it approaches a boundary at which Mur's first order ABC has been

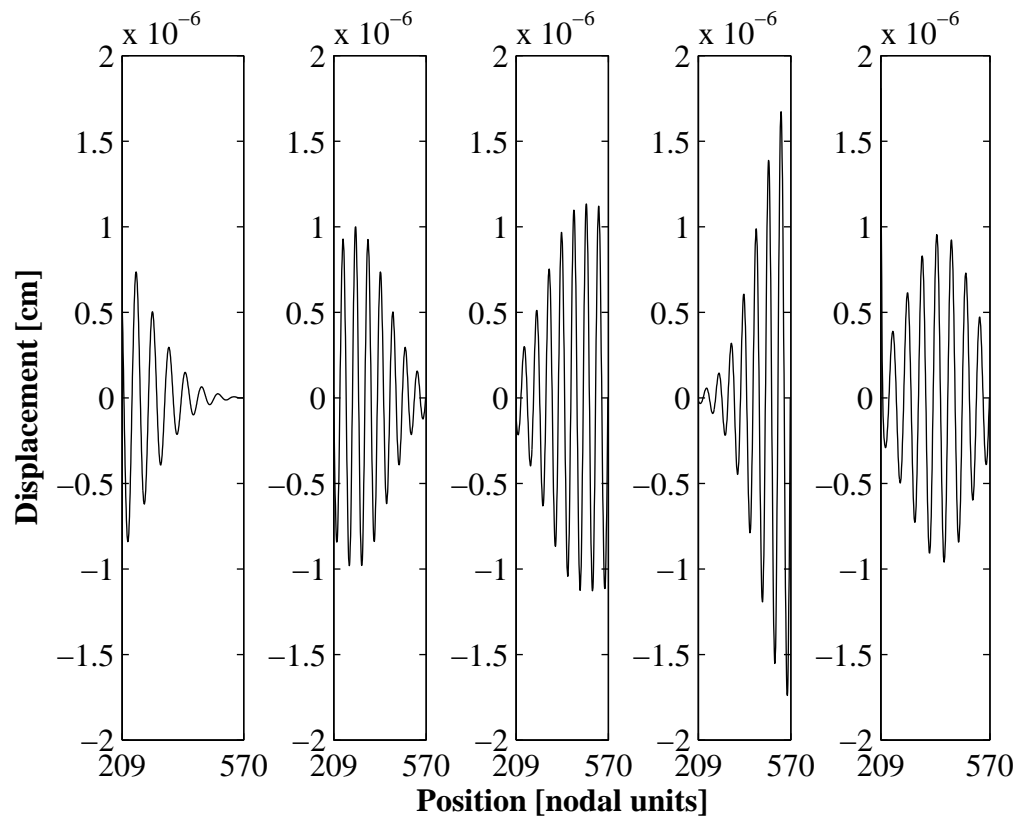


Figure 3.11: Snapshots of wave traveling into the boundary of the simulation space with no boundary condition applied.

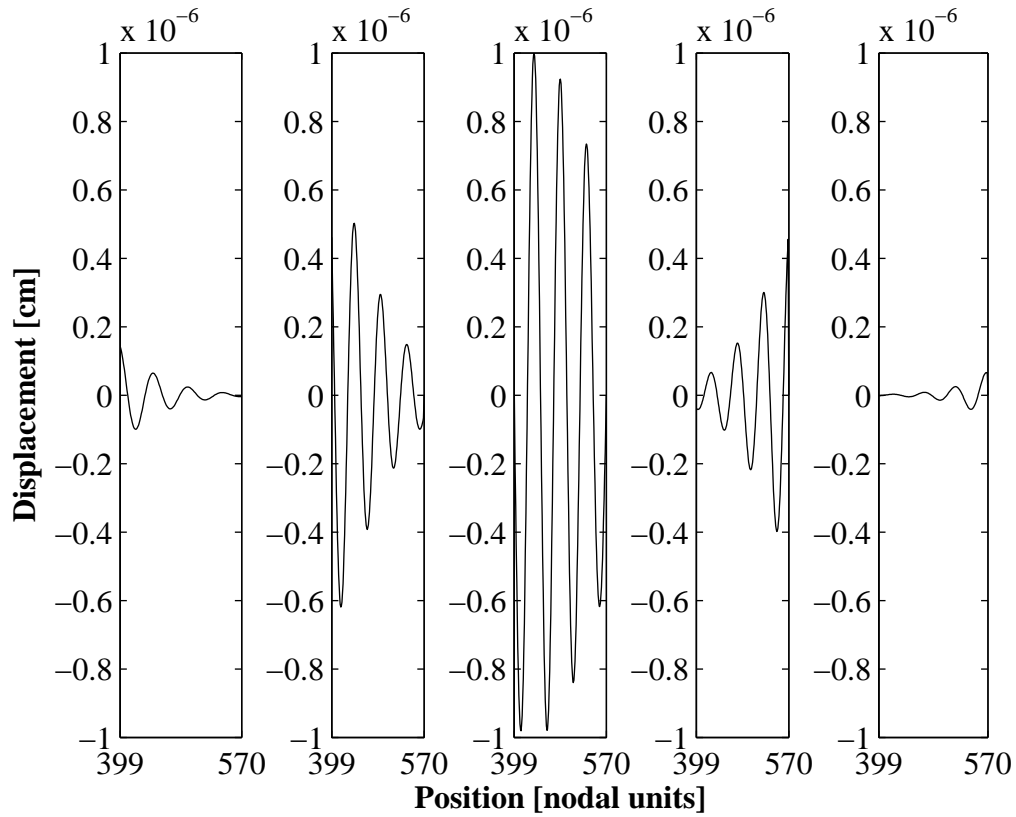


Figure 3.12: Snapshots of wave traveling into the boundary of the simulation space with ABC applied.

applied. The Gaussian pulse was generated so that it is normally incident on the ABC domain. The Gaussian pulse travels toward the boundary and is absorbed as desired.

The Gaussian pulse also migrated across the computational domain in a physically meaningful fashion in that the pulse amplitude was always less than or equal to  $10^{-6}[cm]$ . The simulation supports the implementation of the ABC.

Realistically, however, the phononic crystal will cause elastic waves to reflect, refract, and diffract into a multitude of directions that are not normal to the ABC



domain. When these waves impinge on the ABC domain they would be reflected and may interfere with other waves near the detector. This interference may cause changes in the detected signal that are not attributed to the impulse response of the crystal. Reflections off of the ABC domain would also cause a triple transit phenomenon.

The triple transit phenomenon arises due to the presence of four reflective interfaces: the left and right ABC domains, and the two interfaces between the two homogeneous regions and the phononic crystal. Due to the presence of these reflective interfaces an elastic waves can be reflected back and forth, may transit the phononic crystal a number of times, and potentially be detected by the detector at least twice.

The triple transit phenomenon is known to occur in SAW devices. In SAW devices, acoustic absorbing layers act as an ABC in order to mitigate the triple transit.

During post processing of simulation data, the simulation duration may be decreased (as discussed in Section 3.6) to mitigate the erroneous results that may be generated due to interference caused by reflected waves. Large homogeneous domains also assist in mitigating the triple transit phenomenon.

### 3.7.2 The Periodic Boundary Condition

Figure 3.13 depicts a closeup of the displacement of an aluminum host material versus position in the vicinity a PBC domain. For this test, the plane wave source was applied parallel to the PBC domain. Due to the elastic properties of the

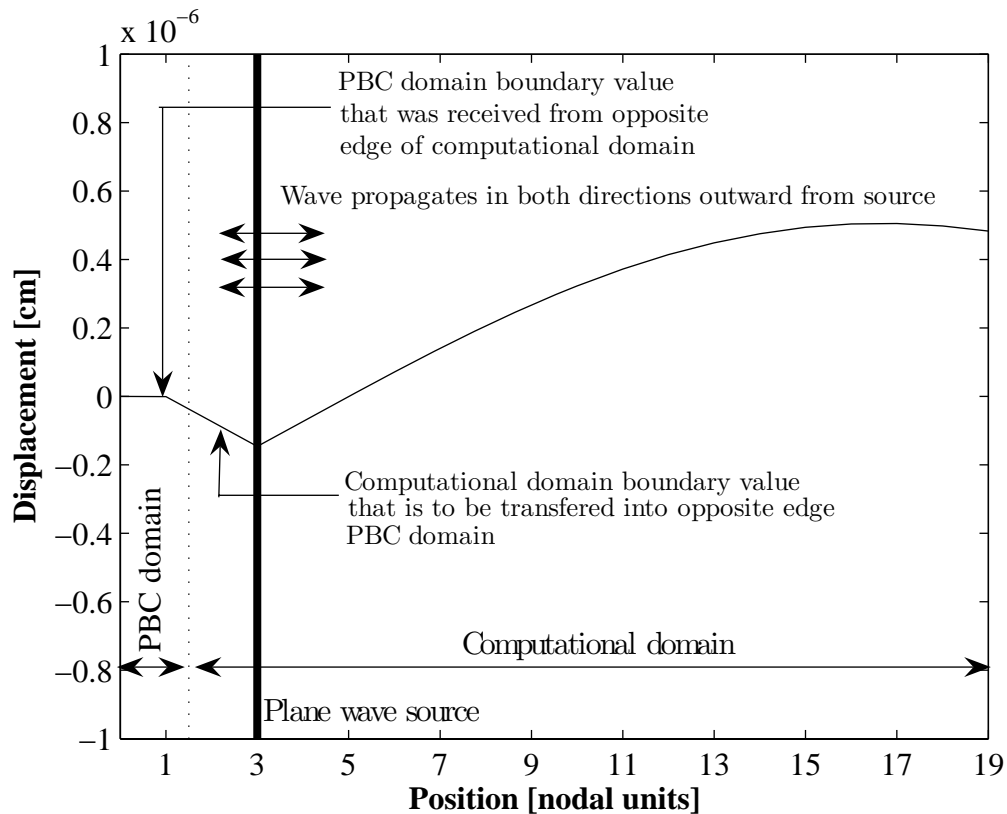


Figure 3.13: Verification of PBC operation for source at node 3 (close up near the location of the source). As seen in the figure, the plane wave source is located two nodal units away from the PBC domain.

aluminum host, the plane wave source displacement generates particle displacement both to the left and the right of the source.

The waves that travel to left of the source rapidly arrive at the left edge of the computational domain and should be transferred to the right edge PBC domain through application of the PBC. This operation may be verified through observation of Figure 3.14.

In Figure 3.14, the plane wave source is located 75 nodal units away from the

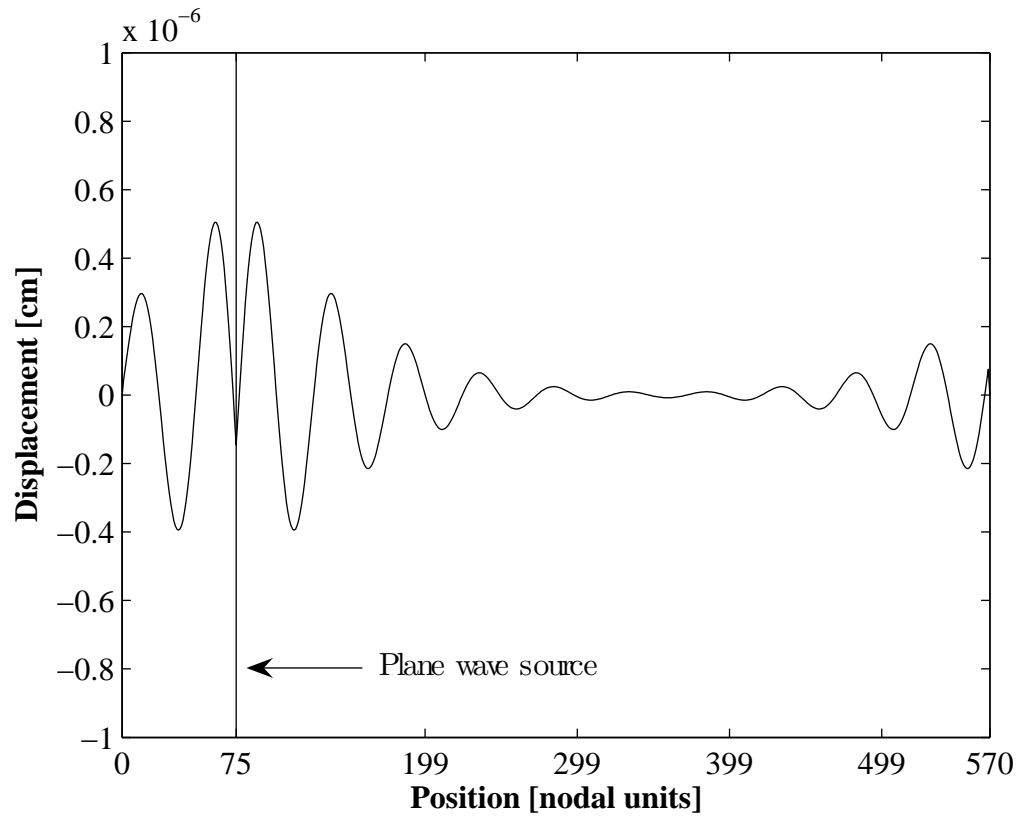


Figure 3.14: Verification of PBC operation for source at node 75.

PBC domain, and generates a Gaussian pulse that has an amplitude of  $10^{-6}[cm]$ . As desired, the elastic wave that traveled into the PBC domain appears emerging from the right edge of the computational domain.

### 3.7.3 Reproducing Published Data

Three structures were simulated to reproduce published data:

1. a layered structure,

2. an aluminium-air crystal, and
3. an aluminium-mercury crystal.

All structures were stimulated using a Kronecker Delta. Hence, the DFT of the transient response is the impulse response. Only the longitudinal component of the elastic waves displacement vector is studied.

Two parameters describe the transient response:

1.  $t_o$ , the time taken for the signal to travel from the source to the detector, and
2.  $t_{transient}$ , the duration of the (non-zero) transient response.

The total simulation duration is computed as follows:

$$t_{TOT} = t_o + t_{transient}. \quad (3.31)$$

### Layered Structure

The phononic band gap crystal simulator was designed for the simulation of two-dimensional phononic crystals, however, the first simulation presented will be that of a layered structure. The layered structure exhibits periodicity in only the  $\hat{x}$  direction, and so is considered a one dimensional phononic crystal.

This layered structure is depicted in Figure 3.15. The dark colored layers were composed of Perspex, while the host material is Water. Simulation constants are contained in Table 3.2.

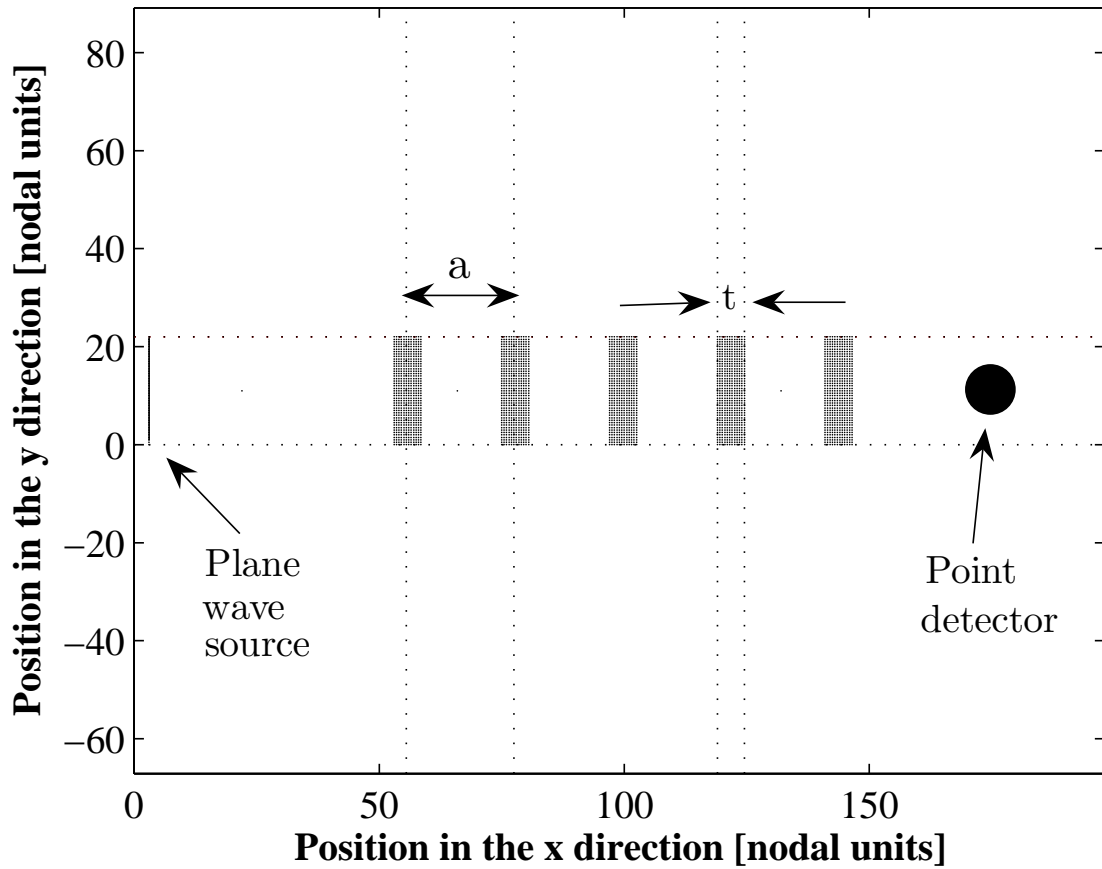


Figure 3.15: Structure of the Bragg grating. The lattice constant,  $acell_{NODES}$ , has been abbreviated as  $a$ . The thickness of the plates is denoted using the variable  $t$ . The plates are composed of Perspex, while the host material is water. Finally,  $t = 0.2[cm]$  and  $a = 0.724[cm]$ .

Table 3.2: Simulation constants for the simulation of the layered structure.

Parameter	Value	Units
Source type	Kronecker Delta, amplitude $1 \times 10^{-6}$	[ <i>cm</i> ]
Host material	Water	–
Layer material	Perspex	–
$N_x$	5	[ <i>cells</i> ]
$N_y$	1	[ <i>cells</i> ]
$\Delta t_{\text{Numerator}}$	0.01	–
$\Delta t$	1.57187929	[ <i>ns</i> ]
$\Delta x = \Delta y$	0.0329	[ <i>cm</i> ]
$k_{\text{max}}$	165000	[ <i>time steps</i> ]
$t_o$	23.476	[ $\mu\text{s}$ ]
$t_{\text{transient}}$	259.3601	[ $\mu\text{s}$ ]
$t_{\text{TOT}}$	282.8361	[ $\mu\text{s}$ ]
$a_{\text{cell}_{CM}}$	0.7238	[ <i>cm</i> ]
$a_{\text{cell}_{NODES}}$	22	[ <i>nodal units</i> ]
<i>Fill Factor</i>	0.272727281	[ $\text{cm}^2/\text{cm}^2$ ]

Simulating the layered structure is of value because the published data are in strong agreement with one another [22]. This agreement positively supports the accuracy of the published data. Moreover, the theoretical data were computed using an approach that is mathematically different from the approach used in the development of the two-dimensional phononic band gap crystal simulator. Validating the simulator operation through comparison with data obtained using a different mathematical approach will illustrate that the results are independent of the approach used to obtain the results.

The DFT of the transient response of Figure 3.16 is presented in Figure 3.17. To achieve the best match with the data presented in [22], the time domain data of Figure 3.16 was modified.

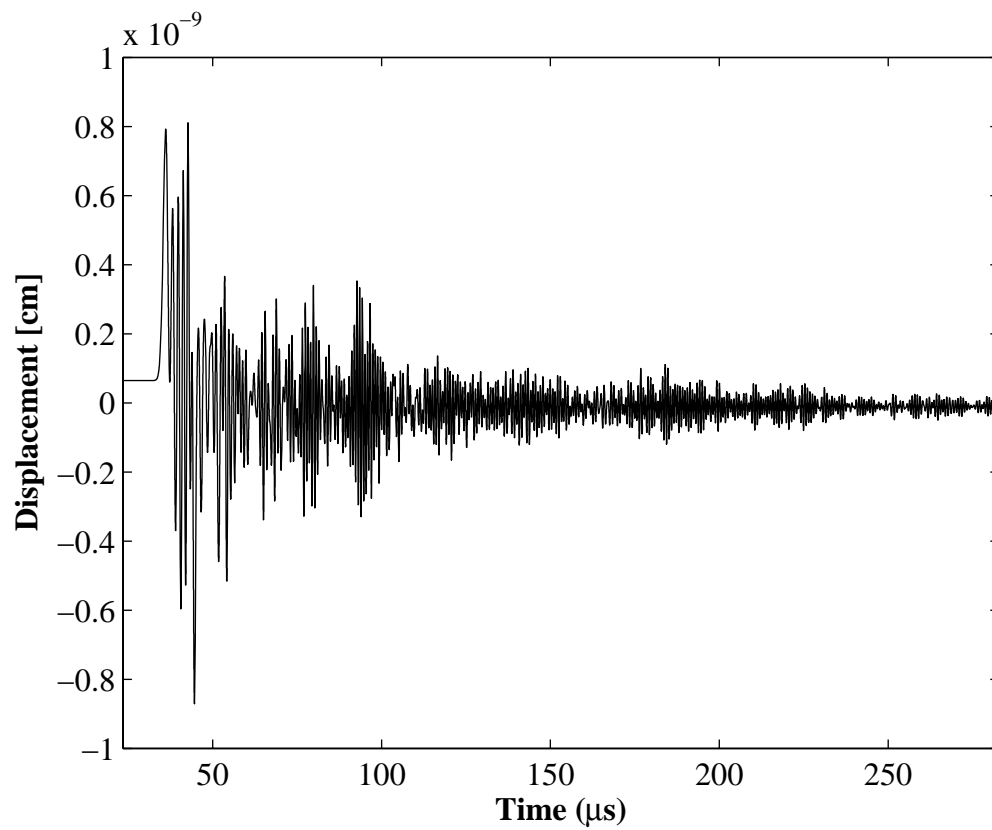


Figure 3.16: Transient response of the layered structure, of Figure 3.15, as detected by a point detector.

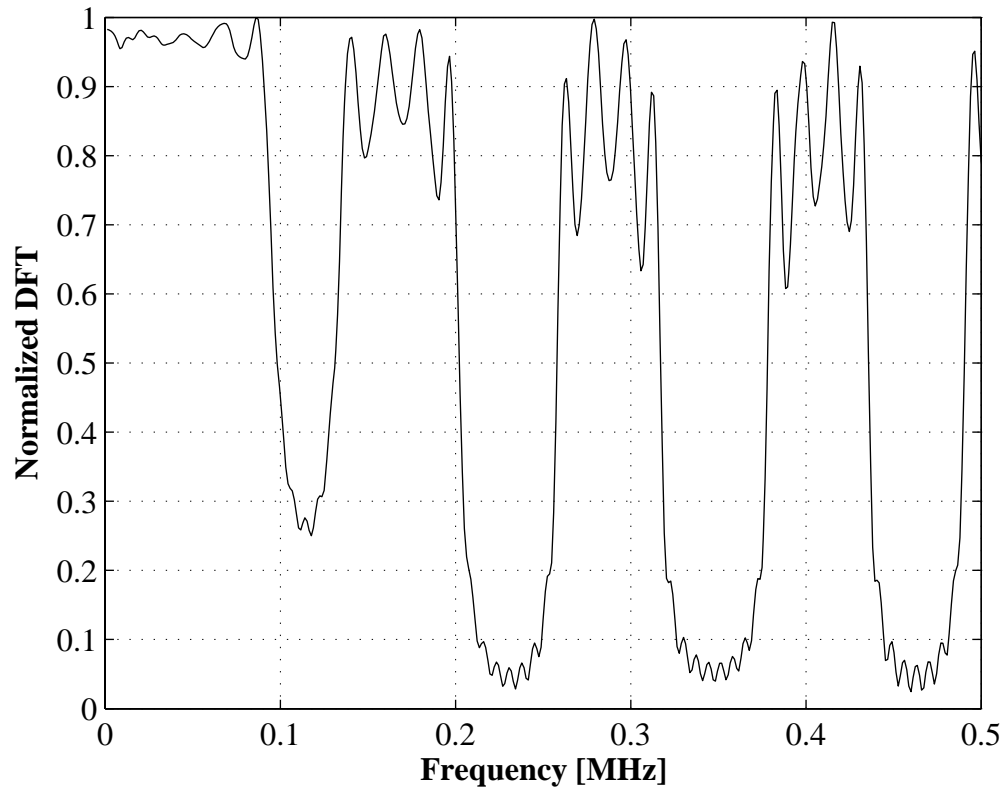


Figure 3.17: Magnitude response of the layered structure of Figure 3.15.



First, the window of time leading up to  $t_o$  was deleted: only the transient response of the phononic band gap crystal remained. Next, the mean value of the remaining transient response was computed and subtracted from the signal. This was done to assist in removing a large spike that was found to occur at zero frequency. The resultant transient response data was presented in Figure 3.16.

The shape of the low frequency pass band of the DFT was still not in strong agreement with the data presented in [22]. It was found that the DFT had to be normalized to the DFT of the transient response (after removing the part of the signal that occurs before the vibrations arrive, and with the mean value of the signal subtracted off in time) of water (the host material). The result is the DFT depicted in Figure 3.17, which is in good agreement with the numerical and experimental data found in [22].

As seen in Figure 3.16, the amplitude of the transient response is always less than  $10^{-6}[cm]$  (the peak amplitude of the input Kronecker Delta) illustrating that the simulator converges. The transient response decays in a fashion expected for a physical system that was stimulated by a Kronecker Delta.

A key feature of the DFT displayed in Figure 3.17 is the presence of pass bands which contain four peaks. The structure depicted in Figure 3.15 contains five Perspex layers, between which four layers of water are enclosed. The number of peaks in the pass bands correspond to the number of enclosed layers of water [22]. As the number of Perspex sheets was increased, the number of peaks in the pass bands was found to increase accordingly, which is consistent with the results presented in [22]. Between the described pass bands occur stop bands (regions of

high attenuation). The locations of the stop bands correspond to the theoretically and experimentally predicted band gaps presented in [22].

If a defect was introduced, into the layered structure depicted in Figure 3.15, by removing the center Perspex plate, a narrow pass band would appear in center of each stop band - this is also in agreement with the data presented in [22].

The stop band that occurs at approximately  $0.1[MHz]$  in Figure 3.17 is not as deep as the other stop bands - this is also consistent with the data reported in [22].

Though the stop bands depicted in Figure 3.17 clearly indicate band gap locations, the stop bands do not indicate infinite attenuation, which is a characteristic of a band gap. To increase the stop band depth, a Hamming temporal window had to be applied to the transient response. However, the use of a Hamming temporal window causes the pass bands to become distorted: the outer peaks of the pass bands become accentuated, while the inner peaks of the pass bands becomes suppressed.

### **Aluminium-Air Crystal**

The next simulated structure was a crystal composed of an aluminium host material with circular air inclusions. The inclusions were arranged in a square lattice. The simulation constants are summarized in Table 3.3. Theoretical and experimental DFT data for the aluminium-air crystal was presented in [21].

Figure 3.18 displays the simulated DFT data overlaid on the data presented in [21]. As was done for the layered structure, the simulated time domain data was modified by deleting the window of time leading up to  $t_o$ , so that only the

Table 3.3: Simulation constants for the simulation of the aluminium-air crystal.

Parameter	Value	Units
Source type	Kronecker Delta, amplitude $1 \times 10^{-6}$	[ <i>cm</i> ]
Host material	Aluminium	—
Inclusion material	Air	—
Inclusion geometry	Circular	—
$N_x$	4	[ <i>cells</i> ]
$N_y$	5	[ <i>cells</i> ]
$\Delta t_{\text{Numerator}}$	0.01	—
$\Delta t$	0.109628952	[ <i>ns</i> ]
$\Delta x = \Delta y$	0.01	[ <i>cm</i> ]
$k_{\text{max}}$	50000	[ <i>time steps</i> ]
$t_o$	2.3	[ $\mu\text{s}$ ]
$t_{\text{transient}}$	5.4824	[ $\mu\text{s}$ ]
$t_{\text{TOT}}$	7.7824	[ $\mu\text{s}$ ]
$a_{\text{cell}_{CM}}$	0.3	[ <i>cm</i> ]
$a_{\text{cell}_{NODES}}$	30	[ <i>nodal units</i> ]
<i>Fill Factor</i>	0.349	[ $\text{cm}^2/\text{cm}^2$ ]

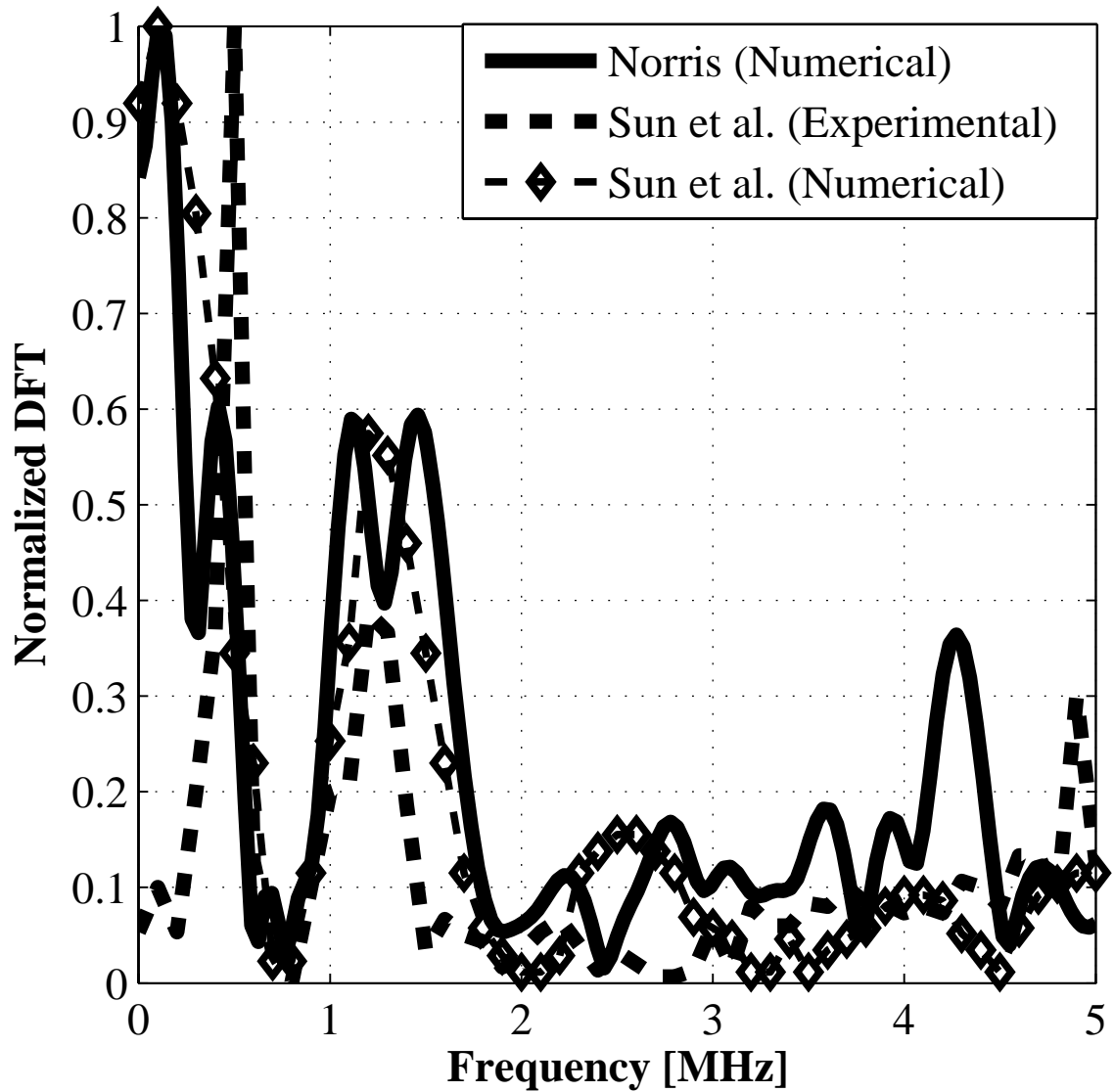


Figure 3.18: Magnitude response of a two-dimensional phononic crystal that is composed of an aluminum host and circular air inclusions. The data curves that are attributed to Sun in the legend were taken from [21].

transient response was utilized in determining the DFT of Figure 3.18. Unlike the simulation of the layered structure: the mean value of the transient response was not subtracted off, and the DFT of the structure was not normalized to that of aluminium (the host material). No temporal window was applied to the transient response data.

Though the numerical data presented in [21] was generated using a different mathematical formulation, and used more accurate FDTD approximations, the overall shape of the DFT data presented in Figure 3.18 shows good agreement with the published numerical and experimental data.

### **Aluminium-Mercury Crystal**

The final structure that was simulated, for validation of the simulator operation, was a crystal composed of an aluminium host material and circular mercury inclusions. The inclusions were arranged in a square lattice. The simulation constants are summarized in Table 3.4. Numerical and experimental DFT data for the aluminium-mercury crystal were presented in [23] and are displayed in Figure 3.19.

Figure 3.19 also displays the DFT data that was obtained using the two-dimensional phononic band gap crystal simulator. As was done for the layered structure, the simulated time domain data was modified by deleting the window of time leading up to  $t_o$ , so that only the transient response was utilized in determining the DFT of Figure 3.19. A temporal window was applied to the transient response. The mean value of the transient response was not subtracted off. The DFT of the transient response of the crystal structure was not normalized to that

Table 3.4: Simulation constants for the simulation of the aluminium-mercury crystal.

Parameter	Value	Units
Source type	Kronecker Delta, amplitude $1 \times 10^{-6}$	[ <i>cm</i> ]
Host material	Aluminium	—
Inclusion material	Mercury	—
Inclusion geometry	Circular	—
$N_x$	15	[ <i>cells</i> ]
$N_y$	3	[ <i>cells</i> ]
$\Delta t_{\text{Numerator}}$	0.1	—
$\Delta t$	0.997623539	[ <i>ns</i> ]
$\Delta x = \Delta y$	0.0091	[ <i>cm</i> ]
$k_{\text{max}}$	55000	[ <i>time steps</i> ]
$t_o$	6.3918	[ $\mu\text{s}$ ]
$t_{\text{transient}}$	54.8683	[ $\mu\text{s}$ ]
$t_{\text{TOT}}$	61.2601	[ $\mu\text{s}$ ]
$a_{\text{cell}_{CM}}$	0.273	[ <i>cm</i> ]
$a_{\text{cell}_{NODES}}$	30	[ <i>nodal units</i> ]
$\text{Fill Factor}$	0.42	[ $\text{cm}^2/\text{cm}^2$ ]

of aluminium (the host material).

The numerical data presented in [23] was generated using the same mathematical formulation, boundary conditions, and FDTD formulation. However, the numerical data (DFT) obtained through simulation using the phononic band gap crystal simulator shows better agreement with the experimental data presented in [23].

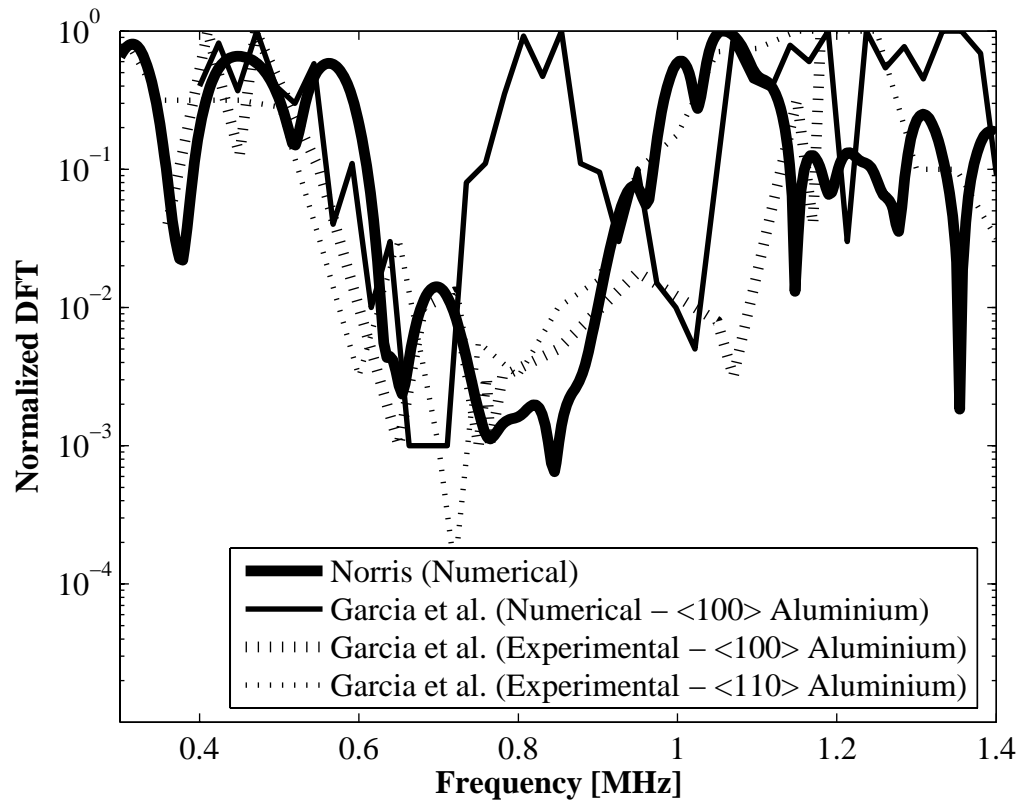


Figure 3.19: Magnitude response of a two-dimensional phononic crystal that is composed of an aluminum host and circular mercury inclusions. The data curves that are attributed to Garcia in the legend were taken from [23].

### 3.7.4 Conclusions

The two-dimensional phononic band gap crystal simulator can capably predict band gap locations for a wide variety of structures. To ensure the best match with published numerical and experimental data, the post processing of the transient response data involved:

1. the proper selection of  $k_{max}$ ;
2. judgement over whether the average value of the transient response should, or should not, be subtracted from the transient response;
3. judgement over whether a temporal window should, or should not, be utilized;  
and
4. judgement over whether the DFT of the transient response of the crystal should, or should not, be normalized to the DFT of the transient response of the host material.

In Section 3.7.2, the plane wave source was observed to generate elastic waves that were directed both to the left and right of the plane wave source. As in Figure 3.2, the plane wave source is located directly beside the left ABC domain. Half of the induced wave energy is directed into the left ABC domain, and the other half of the induced wave energy is directed toward the detector. The ABC domain perfectly absorbs the wave generated by the plane wave source since the wave impinges on the left ABC domain at a normal angle of incidence. Thus, 3[dB] of loss is associated with the plane wave source.



The point detector of the simulator is ideal and detects elastic waves without loss.

## Chapter 4

# Two-Dimensional Phononic Crystal Analysis

This chapter contains a discussion of phononic crystal band gap engineering, followed by an analysis of fractal and circular inclusion based phononic crystals. The phononic crystals are analyzed using techniques that include:

1. the use of the DFT to convert discrete time domain impulse response data into frequency domain (magnitude and phase response) data,
2. the use of phase data to compute group delay, phase velocity, wavelength, and dispersion characteristics, and
3. the generation of three-dimensional surface plots which are used to view particle displacement versus position in the phononic crystal.

## 4.1 Phononic Crystal Band Gap Engineering

The design parameters utilized in the band gap engineering of phononic crystals are enumerated below.

1. Acoustic impedance mismatch between the host and inclusion materials: the reflection coefficient for normally incident waves,  $\Gamma$ , is a good figure of merit to describe the acoustic impedance mismatch between two materials. The reflection coefficient between the host and inclusion material is given by  $\Gamma = (Z_i - Z_h)/(Z_i + Z_h)$ , where  $Z_i$  is the inclusion acoustic impedance and  $Z_h$  is the host acoustic impedance. The acoustic impedance is computed as:  $Z = \rho\nu$ , where  $\rho$  is the material density, and  $\nu$  is the elastic wave velocity in the direction of interest. The reflection coefficient is representative of the density contrast between the host and inclusion material, and also accounts for the wave velocity contrast and thus material properties such as Young's modulus ( $\nu = \sqrt[2]{\frac{K}{\rho}}$ , where  $K$ , the Bulk modulus, is a function of Young's modulus). In rare cases, the host and inclusion may have the same material density and, provided that there is a contrast in Young's modulus, phononic band gaps will form [13]. Hence, while the density contrast between the host and the inclusion may be a valid figure of merit to describe the suitability of materials used in most cases, the reflection coefficient for normal incidence is valid in general.
2. Fill factor: the area (volume) of the inclusion divided by the area (volume) of the unit cell for two-dimensional (three-dimensional) structures is commonly

varied to perform band gap engineering. Fill factor may be varied in two ways: (1) by fixing the lattice constant and varying the inclusion size, and (2) by fixing the inclusion size and varying the lattice constant.

3. Topology: two crystal topologies are utilized. The first is the cermet topology, where the inclusion material density is designed to be greater than the host material density (in other words,  $\Gamma > 0$ ) [13]. In the cermet topology, the scattering center is the inclusion [13]. The second topology is the network topology, where the host material density is designed to be greater than the inclusion material density (in other words,  $\Gamma < 0$ ) [13]. In the network topology, the scattering center is the host [13].
4. Macro and micro features: the feature size of a particular feature on the inclusion is classified as macro or micro by contrasting the feature size with the wavelength of interest. As a rule of thumb, a wave that has a wavelength of  $\lambda$  may only resolve a feature if  $\lambda \leq 2 \times featureSize$ , where *featureSize* is the size of the feature. A feature is denoted as a macro feature if:  $2 \times featureSize > \lambda$ . A feature is denoted as a micro feature if:  $2 \times featureSize < \lambda$ . For two-dimensional phononic crystals both macro and micro features have been shown to be important in determining the band structure of the crystal.
5. Inclusion bulk and inclusion boundary geometry: macro and micro features may be introduced into the boundary of an inclusion while maintaining a similar overall shape to the bulk of the inclusion. This supports the recognition of a distinction between inclusion boundary and inclusion bulk geometry.

6. Inclusion orientation: rotating an inclusion, whose geometry is not rotationally invariant, has been shown to control band gap width [24].
7. Defect states, disorder, and symmetry in the crystal lattice: the symmetry of a crystal lattice may be broken by introducing defects through the removal of a single inclusion (point defect) or portions of, or entire, rows and columns of inclusions (line defects) or random forms of disorder. The introduction of point defects into layered structures has been shown to cause the appearance of narrow pass bands within band gaps [22]. Line defects may be employed in the design of phononic band gap wave guides, multiplexers, and demultiplexers [8].
8. Device size scaling: phononic band gap filters are linear systems. Operating frequency and device size are inversely proportional.
9. Advanced architectures: Cascading phononic crystals, by placing them adjacently in a host material, results in an overall magnitude response which is approximately the product of each crystal's individual magnitude response. To ensure that that the overall magnitude response is identically the product of the individual magnitude responses, the crystals have to be acoustically isolated then cascaded.

These design parameters provide multiple degrees of freedom in the band gap engineering of phononic crystals. These design parameters will now be manipulated to produce two phononic crystals: one based on fractal inclusion structures, and the other based on circular inclusion structures.

## 4.2 Fractal Inclusion Based Phononic Crystals

In this section, a fractal inclusion structure is demonstrated to create two-dimensional phononic crystals. The following discussion is believed to describe the first instance in which fractal inclusion structures have been utilized to create phononic crystals.




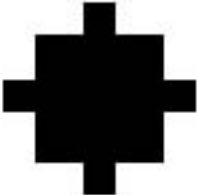

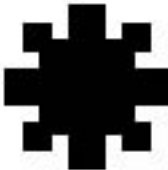
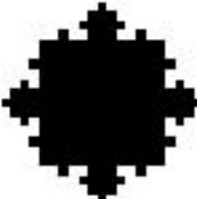


### 4.2.1 Introduction to Fractal Crystals

The fractal inclusion structures that were utilized are depicted in Table 4.1 and were generated using an iterative processes that introduced micro features into the boundary of an inclusion that had a square bulk geometry. As seen in Table 4.1, Structure 2 is related to Structure 1 in that the features on Structure 2 are the features on Structure 1 inverted (that is, turned inside out). Structure 3 does not appear to be related to either Structure 1 or Structure 2.

The fractal structures are well suited for use with the FDTD numerical method since the structures are fundamentally composed of squares, and so a step approximation of curved surfaces was not required. The iterative process utilized to generate the fractal inclusion structures is described in [25], where the fractal inclusion structures were used to create photonic band gap crystals. The study of photonic and phononic crystals are not one and the same; the following distinctions between the study of photonic and phononic crystals may be made.

The waves studied in photonic crystals are electromagnetic waves, while the waves studied in phononic crystals are elastic waves. However, both electromagnetic and elastic waves may contain transverse and longitudinal components.

Table 4.1: Fractal inclusion structures [25].

	Structure 1	Structure 2	Structure 3
Initial			
Iteration 1			
Iteration 2			

Through the use of an appropriate transducer, electrical signals may be processed using both photonic and phononic crystals. However, the phase velocity of an elastic wave is approximately five orders of magnitude less than that of an electromagnetic wave. Hence, it will take noticeably longer to process a signal with a phononic crystal, than with a photonic crystal.

Often it is desirable for the wavelength at a given frequency to equal some device feature size. For a given operating frequency, the wavelength of an elastic wave is smaller than the wavelength of an electromagnetic wave, and so phononic crystals may theoretically be made smaller than photonic crystals. However, if for a given frequency, wavelength is less than the minimum fabrication process feature size, then larger phase velocities and wavelengths would be desirable [4]. The proper selection of material composition may allow for the phononic crystal designer to obtain the desired wavelength at a given frequency.

Photonic crystals are governed by the physics of electromagnetism, while phononic crystals are governed by the physics of elastic wave mechanics. In photonic crystals the refractive index,  $n$ , (or equivalently the relative dielectric constant,  $\epsilon_r$ ) of the host and inclusion materials must differ, while in phononic crystals the material density,  $\rho$ , of the host and inclusion material usually must differ.

Having distinguished between photonic and phononic crystals, it is now reasonable to acknowledge that the application of fractal inclusion structures to phononic crystals may not yield results that are in agreement with the results yielded from the application of fractal structures to photonic crystals and microwave devices. That said, the application of fractal structures to photonic crystals and microwave



structures has been widely observed to produce two effects: (1) band gap widening, and (2) multiple pass band behavior [25].

## 4.2.2 Representation of Fractal Structures on a Discrete Grid

The fractal inclusion layouts are included in Appendix B. A comment may be made regarding the input of fractal shaped structures into a simulator that represents structures on a discrete grid.

The length of time that a simulation runs for is related to the size of the structure being simulated. The size of the structure is defined in terms of the number of discrete nodes that the structure occupies in the simulation space. The larger the structure is in size, the longer the simulation of the structure will take to run.

To minimize simulation time, the minimum feature size was chosen to be represented by a single point. Of the three fractal structures that were simulated, only Structure 3 contains features that have a physical size equal to the minimum feature size.

When modeling a feature that is of the minimum feature size as a single point, it is not clear as to what the physical size of such a feature is. The following rules were applied when analyzing the physical size of the features on a fractal inclusion: the physical distance between three co-linear points, and two co-linear points, in the  $\hat{x}$  and  $\hat{y}$ , directions is  $\Delta x$  and  $\Delta y$ , and  $\frac{1}{2}\Delta x$  and  $\frac{1}{2}\Delta y$ , respectively. The physical size of a point in the  $\hat{x}$ , and  $\hat{y}$ , directions is  $< \frac{1}{2}\Delta x$ , and  $< \frac{1}{2}\Delta y$ , respectively.

Figure 4.1 depicts an arbitrary structure drawn onto the discrete grid by the same method as that utilized to draw the fractal structures onto the discrete grid. As seen in Figure 4.1, the smallest feature size is represented by a single point, as was the case when Structure 3 was drawn onto the discrete grid.

When representing the smallest feature as a single point, it is possible that some features may (1) exist only on the integer-grid, (2) may exist only on the half-grid, or (3) may exist only on points at the intersection of the integer-grid and half-grid. Thus, minimizing simulation time by representing the smallest feature size by a single node, results in the trade off wherein features that have a physical size equal to the smallest feature size may not be represented on both the integer- and half-grid.

Though  $u_x$ , and  $u_y$ , are computed only at the integer-grid, and half-grid, nodes, respectively, the components of the stress tensor are computed everywhere (on integer-grid and half-grid nodes, and at the intersection points of the integer-grid and half-grid). The  $u_x$  and  $u_y$  components of the displacement vector are a function of the stress tensors. Thus,  $u_x$  and  $u_y$  are influenced by fractal features drawn anywhere on the discrete grid. This qualitatively supports the functionality of the described method of representing fractal structures on the discrete grid.

### 4.2.3 Uniformity of Simulation Conditions

In any experiment where the outcome of more than one simulation are going to be compared, it is important that the simulations are conducted using the same simulation parameters. The entity that may be varied amongst simulations is the

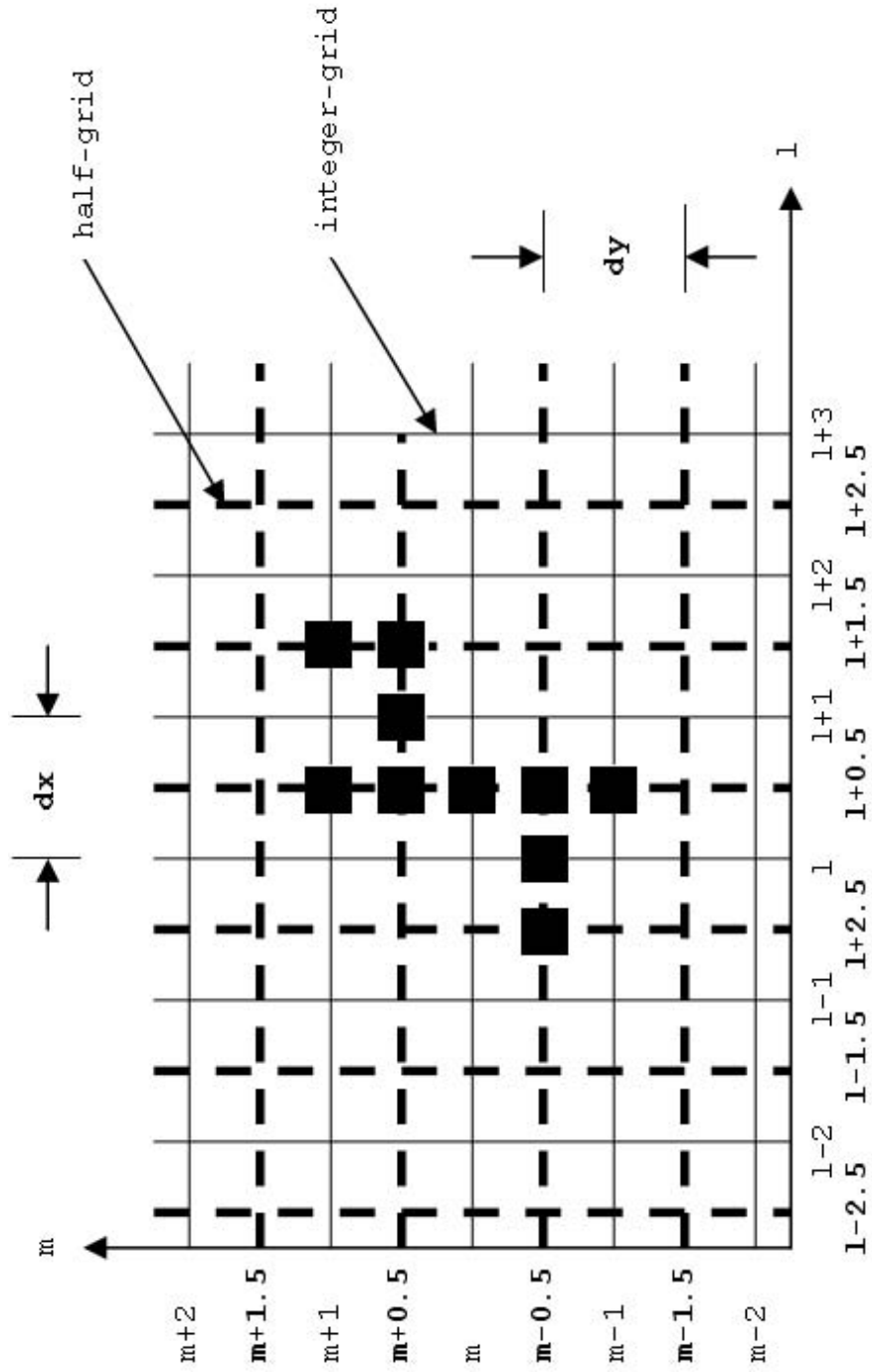


Figure 4.1: Arbitrary structure represented on discrete grid.

structure being simulated. The outcome of the simulations involving the fractal structures will be compared and appropriately the simulation parameters were maintained constant.

To elaborate on the necessity of such an experimental procedure, consider that, for example, varying  $\Delta t$ , may cause a change in the outcome of a simulation - it is not of interest to observe a change in the outcome of a simulation due to a change in such a simulation parameter. What is of interest is to observe the change in the outcome of a simulation due to a change in the geometry of a fractal inclusion structure. Hence, simulation parameters were maintained constant while the fractal inclusion structure was varied.

The physical quantities that are computed by the simulator are the displacement vector and stress tensor (Equation 3.15 to Equation 3.23). As may be deduced when viewing Equation 3.15 to Equation 3.23, the displacement vector and stress tensor are a function of six simulation parameters:  $\Delta t$ ,  $\Delta x$ ,  $\Delta y$ ,  $\lambda$ ,  $\mu$ , and  $\rho$ .

To maintain these six simulation parameters constant, first  $\Delta x$  ( $= \Delta y$ ) and  $\Delta t$  were fixed. As a result,  $\Delta t$  is fixed. The Lamé coefficients,  $\lambda$  and  $\mu$ , and the density,  $\rho$ , are material parameters and were held constant since it was not desired to change the material composition of the fractal based phononic crystals.

The interaction of elastic waves with the inclusion depends on the relative magnitude of the wavelength and the physical size of the inclusion. By maintaining  $\Delta x$  ( $= \Delta y$ ) constant, all fractals consisted of a fundamental element that had fixed physical dimensions. The initial square structure also had a fixed physical size of  $0.12[cm]$  by  $0.12[cm]$ . Thus, by maintaining the physical size of the initial square

Table 4.2: Simulation constants for the simulation of fractal systems.

Parameter	Value	Units
Source type	Kronecker Delta, amplitude $1 \times 10^{-6}$	[ <i>cm</i> ]
Host material	Aluminium	–
Inclusion material	Mercury	–
$N_x$	15	[ <i>cells</i> ]
$N_y$	3	[ <i>cells</i> ]
$N_x H_{omo}$	4	[ <i>cells</i> ]
$\Delta t$	0.54814	[ <i>ns</i> ]
$\Delta x = \Delta y$	0.005	[ <i>cm</i> ]
$t_{transient}$	47	[ $\mu s$ ]

structure a constant, all fractals are created from a structure that initially had the same scattering ability (ability to interact with elastic waves).

The interaction of elastic waves with the phononic crystal also depends on fill factor. With the initial square inclusion size fixed, the lattice constant,  $acell_{NODES}$ , becomes chosen to maintain a constant fill factor. The fill factor was maintained at 25%.

The simulation constants for the simulation of all fractal inclusion structures are contained in Table 4.2, and the simulation variables are listed in Table 4.3. As seen in Table 4.3, it was not possible to maintain the fill factor at exactly 25% throughout all simulations. This is the case because the lattice constant,  $acell_{CM}$ , was adjusted in discrete increments of  $\Delta x$  ( $=\Delta y$ ).

The last measure taken to ensure uniformity in simulation conditions was the varying of  $k_{max}$  during post processing of transient response data. Varying  $k_{max}$  compensates for the variation in the lattice constant, which determines the overall

Table 4.3: Simulation variables for the simulation of fractal systems.

	$acell_{CM}$ [cm]	$acell_{NODES}$ [nodal units]	$F$ [%]	$t_o$ [ $\mu s$ ]	$t_{TOR} = t_o + t_{transient}$ [ $\mu s$ ]	$k_{max} = \frac{t_{TOR}}{\Delta t}$ [time steps]
Initial Square	0.24	48	25.0	6.64	53.64	98,249
Structure 1 Iteration 1	0.26	52	26.6	7.32	54.32	99,489
Structure 1 Iteration 2	0.27	54	25.1	7.60	54.60	100,000
Structure 2 Iteration 1	0.21	42	24.5	5.90	52.90	96,899
Structure 2 Iteration 2	0.19	38	25.8	5.62	52.62	96,388
Structure 3 Iteration 1	0.24	48	26.1	6.75	53.75	98,449
Structure 3 Iteration 2	0.24	48	26.3	6.75	53.75	98,449

physical size of the phononic crystal.

As seen in Table 4.2, the duration of the transient response that is post processed into the DFT was maintained constant at  $t_{transient} = 47[\mu s]$ . All devices contain the same number and arrangement of inclusions. Hence as the lattice constant was varied, the physical size of the phononic crystal would vary. Due to this change in the physical size of the phononic crystal, elastic waves would arrive at the output of the crystals at a different time,  $t_o$ , for each device.

The simulation duration is computed as  $k_{max} = t_{TOT}/\Delta t = (t_o + t_{transient})/\Delta t$ , where  $t_{TOT}$  is given by Equation 3.31. Since  $t_o$  varies from device to device,  $k_{max}$  correspondingly varies, for a constant  $t_{transient}$ . By varying  $k_{max}$  in this fashion, it is ensured that the same duration of the transient response is examined during post processing.

In summary, the described simulation methodology ensures that the only variable between the simulation of different fractal inclusion structures is the geometry of the fractal: all other parameters are held constant. Hence, uniformity in the simulation conditions was maintained and there are equal grounds for comparison of the results presented below.

#### 4.2.4 Wavelength Characteristics

The wavelength characteristic for the phononic crystal created using the Initial inclusion structure is depicted in Figure 4.2. Using the relation  $\lambda = c_l/f$ , where  $c_l$  is the elastic wave longitudinal velocity in the material of interest (see Appendix A),

and  $f$  is frequency, the wavelength characteristics for the aluminum host material and the mercury inclusion material were also plotted in Figure 4.2.

From Figure 4.2 it may be seen that the wavelength characteristic for the crystal does not completely match that of either the host or inclusion material. For wavelengths less than the lattice constant,  $a_{cell_{CM}} = 0.24[cm]$ , the wavelength characteristic is approximated by that of the inclusion material. For wavelengths greater than the lattice constant,  $a_{cell_{CM}} = 0.24[cm]$ , the wavelength characteristic rapidly begins to approach that of the host material. This suggests that, in the crystal, there is a relation between the wavelength at a given frequency and the physical device dimensions, such as the lattice constant.

### One-Dimensional Theory of Elastic Wave Resolving Ability

An elastic wave, of wavelength  $\lambda$ , may resolve a feature, of feature size  $featureSize$ , if the physical size of the feature is greater than half the wavelength:  $featureSize \geq \frac{1}{2}\lambda$ . The largest wavelength,  $\lambda_{max}$ , that may resolve a given feature is:  $\lambda_{max} = 2 \times featureSize$ . In words: as inclusion features become small, or wavelength becomes large, elastic waves may not resolve all inclusion features.

Next, the effects of maximum feature sized features are considered. Then, the effects of minimum feature sized features are considered.

### Effect of Maximum Feature Sizes

The features of a phononic crystal that are considered to be of the maximum feature size are the inclusion width and the lattice constant. The width of the Initial



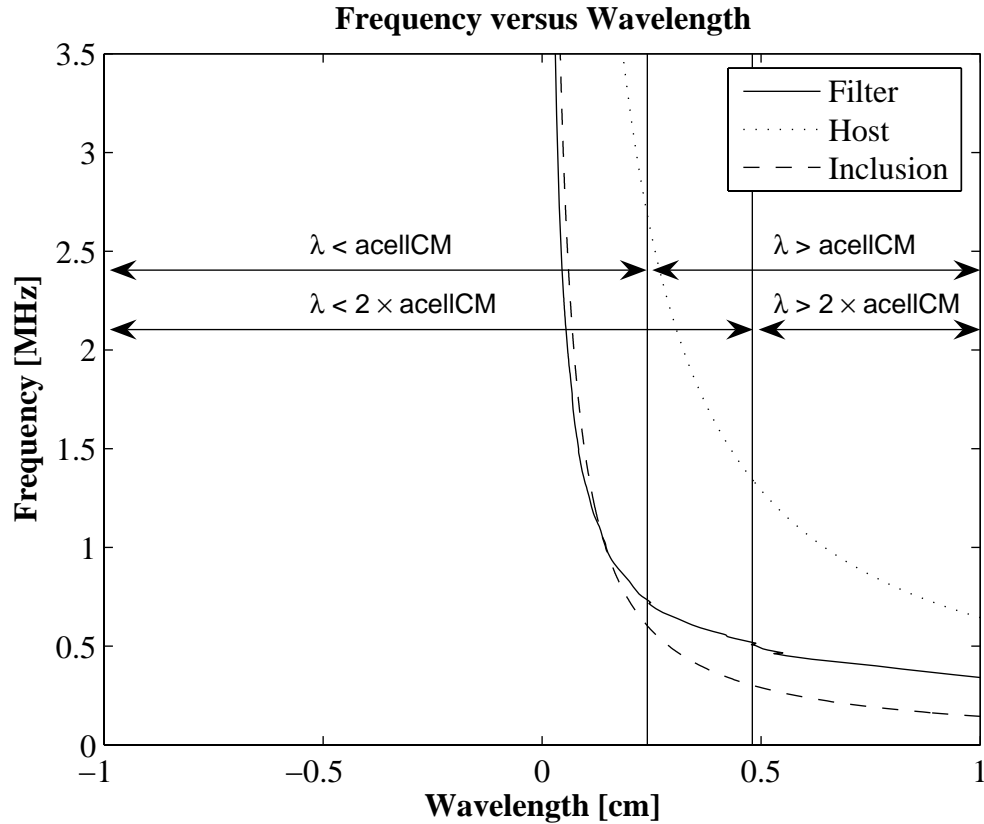


Figure 4.2: Wavelength characteristic for a filter created using the Initial Square inclusion structure, and the wavelength characteristic for the aluminum inclusion material and the mercury host material. For the filter created using the Initial Square structure  $acell_{CM} = 0.24[cm]$ .

inclusion is  $0.12[cm]$ , which would be resolved by waves that have wavelengths of  $0.24[cm]$  and smaller. The lattice constant of the crystal composed of the Initial inclusion is  $0.24[cm]$ . Near a wavelength of approximately  $0.24[cm]$ , an interesting feature is present in the wavelength characteristic (Figure 4.2) of the crystal composed of the Initial inclusion.

Vertical lines corresponding to  $\lambda = 0.24[cm]$  and  $\lambda = 0.48[cm]$  are drawn onto Figure 4.2. Between these two vertical lines, the wavelength characteristic transitions from resembling that of the inclusion, and begins to resemble that of host.

In the frequency domain analysis discussed later, it will be seen that a band gap forms at the frequency where the wavelength characteristic of the crystal transitions from that of the inclusion to that of the host.

The wavelength characteristics for all iterations of Structure 1, Structure 2, and Structure 3 are contained in Figure 4.3, Figure 4.4, and Figure 4.5, respectively.

From Figure 4.3, Figure 4.4, and Figure 4.5, above  $1[MHz]$ , the elastic waves that are present in the phononic crystal have a wavelength that is less than double the lattice constant ( $< 2 \times a_{cell_{CM}}[cm]$ ). Hence, according to the one dimensional theory described above, most of the elastic waves in the frequency regime from  $1[MHz]$  to  $3.5[MHz]$ , are capable of resolving features that are smaller than the maximum feature sizes.

The one-dimensional analysis described above provides insight into the operation of the phononic crystal at low frequencies (frequencies that correspond to wavelengths that have a magnitude on the order of the maximum feature sizes). However, the phononic crystal is a two-dimensional entity and displays a much

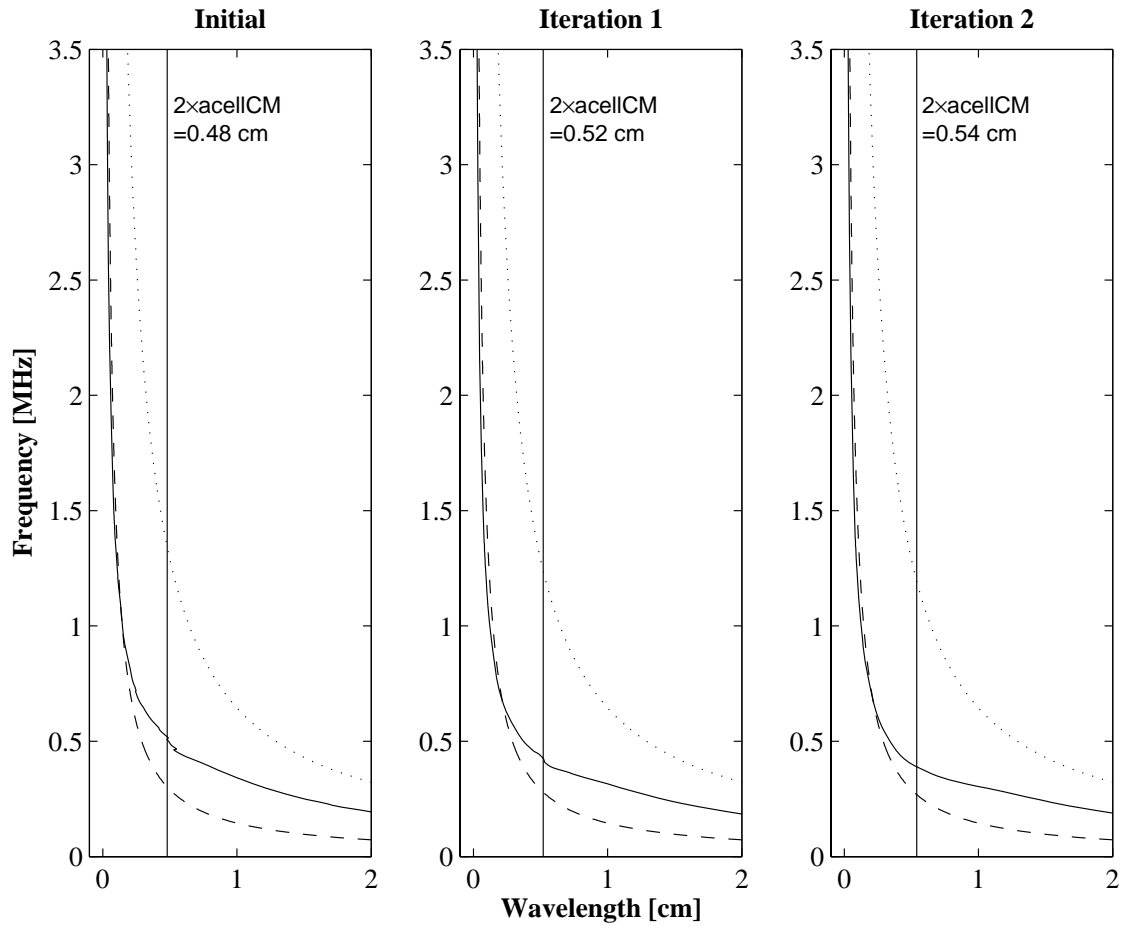


Figure 4.3: Wavelength characteristic for Structure 1 (please refer to the legend of Figure 4.2).

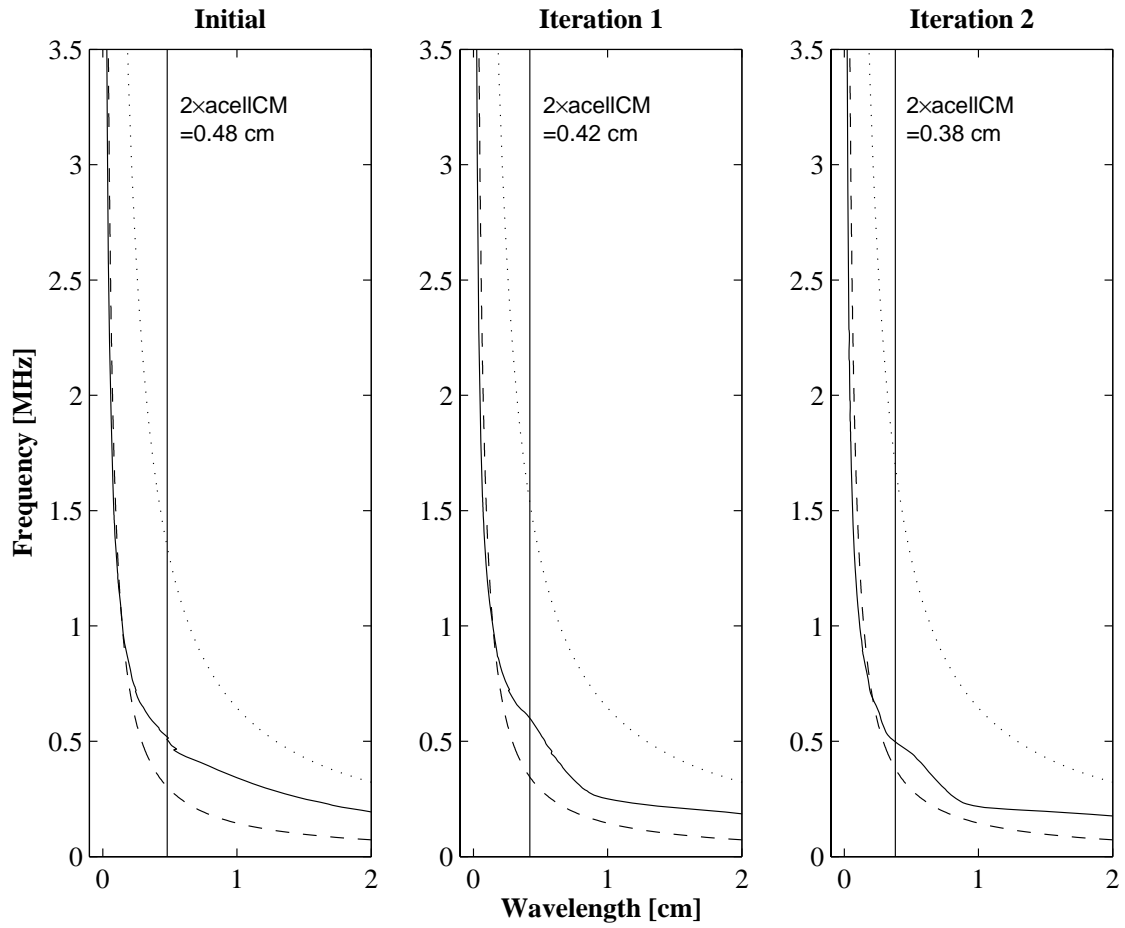


Figure 4.4: Wavelength characteristic for Structure 2 (please refer to the legend of Figure 4.2).

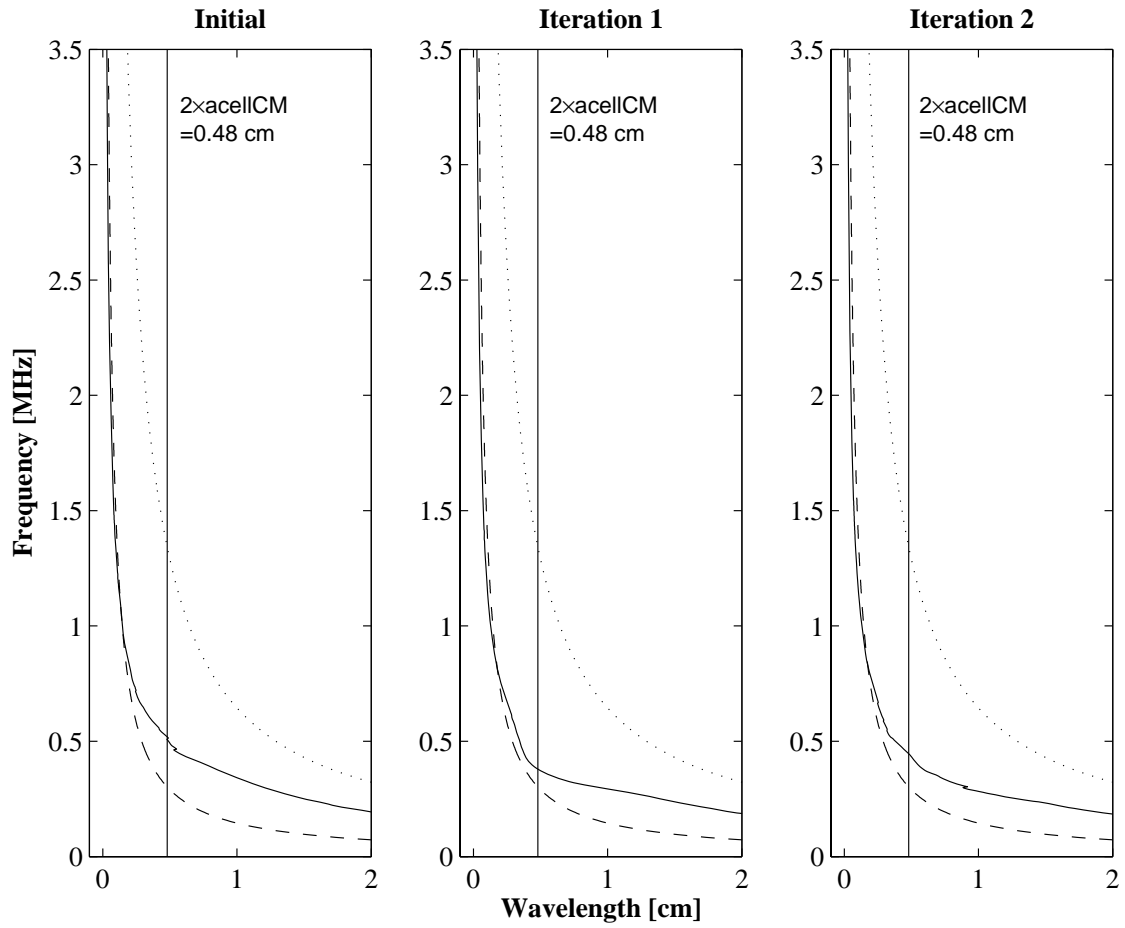


Figure 4.5: Wavelength characteristic for Structure 3 (please refer to the legend of Figure 4.2).

more complex behavior at high frequencies.

Two-dimensional effects increase the complexity of the theory that describes how elastic waves will interact with the crystal at high frequencies (short wavelengths). Short wavelengths also allow for minimum feature sized features, which are in abundance on the fractal boundary, to be resolved. The effects of features that have a physical size less than  $0.12[cm]$  (the width of the Initial inclusion) are now considered.

### Effect of Minimum Feature Sizes

At approximately  $0.5[MHz]$ , wavelength begins to decay to less than  $2 \times acell_{CM}[cm]$ . As wavelength decreases, it becomes wise to check the accuracy of the data. As a rule of thumb, simulation data is considered accurate if  $\lambda \geq 10\Delta x = 10\Delta y$ . In this case,  $10\Delta x = 10\Delta y = 0.05[cm]$ . In Figure 4.3, Figure 4.4, and Figure 4.5, it may be seen that the wavelength characteristic of the phononic crystal converges with the wavelength characteristic of mercury as frequency increases. Hence, by computing the elastic wave wavelength in mercury at  $3.5[MHz]$ , the accuracy of the phononic crystal simulation data, for the  $3.5[MHz]$  regime, can be deduced. Utilizing Appendix A, at a frequency of  $3.5[MHz]$ ,  $\lambda = \frac{c_{l-mercury}}{f} = \frac{145000[cm/s]}{3.5[MHz]} \approx 0.04[cm]$ , which is less than  $10\Delta x = 10\Delta y = 0.05[cm]$ . Hence, data near  $3.5[MHz]$  is less accurate than desired.

The exact numerical values for wavelength at  $3.5[MHz]$  are listed in Table 4.4 along with the minimum resolvable feature size.

Comparing Table 4.4 with Table 4.5, at  $3.5[MHz]$  some fractal features are

Table 4.4: Wavelength at 3.5[MHz] for all fractal based crystal structures.

Device inclusion	Wavelength at 3.5[MHz]	Minimum resolvable feature size for waves at 3.5[MHz]
Initial Square Structure	0.030[cm]	0.015[cm]
Structure 1 Iteration 1	0.028[cm]	0.014[cm]
Structure 1 Iteration 2	0.029[cm]	0.015[cm]
Structure 2 Iteration 1	0.024[cm]	0.012[cm]
Structure 2 Iteration 2	0.021[cm]	0.011[cm]
Structure 3 Iteration 1	0.026[cm]	0.013[cm]
Structure 3 Iteration 2	0.026[cm]	0.013[cm]

resolvable while other features are smaller than the minimum resolvable feature size.

By examining the wavelength characteristic above 3.5[MHz], it was deduced that the wavelengths required to resolve features on the order of  $\Delta x = \Delta y = 0.005[cm]$  - that is, wavelengths of 0.01[cm] or less - are not abundantly present in the wavelength characteristic until frequency approaches 50[GHz]. However, as stated above, the accuracy of the wavelength characteristic as wavelength becomes less than  $10\Delta x = 10\Delta y = 0.05[cm]$  is poor.

Thus, according to the one-dimensional theory, many of the micro features present on some fractal inclusion structures may not be resolved by elastic waves in the 0[MHz] to 3.5[MHz] regime. The micro features on the fractal inclusion structures make the structure unique. Hence, the precise identity of the fractal inclusion structures may be unresolved by the elastic waves in the 0[MHz] to 3.5[MHz] regime.

Table 4.5: Minimum feature sizes of fractal inclusion structures.

	Feature size(s) [cm]	Indentation feature size(s) [cm]	$\lambda_{max} = 2 \times featureSize$ [cm]
Initial Square	0.12	–	0.24
Structure 1 Iteration 1	0.0275	–	0.055
Structure 1 Iteration 2	0.005, 0.0075, 0.025	–	0.010, 0.015, 0.050
Structure 2 Iteration 1	0.042	0.0325	0.065, 0.084
Structure 2 Iteration 2	0.0075, 0.015	0.01, 0.0125, 0.03	0.015, 0.02, 0.025, 0.03, 0.06
Structure 3 Iteration 1	0.025, 0.0325	0.0175	0.035, 0.05, 0.065
Structure 3 Iteration 2	0.0025, 0.005, 0.0075	0.0075 and smaller	0.005, 0.01, 0.015



One may then be tempted to propose that: (1) the magnitude response of some devices may share strong similarities and (2) only low-frequency (large-wavelength) should travel through the crystal unaffected. To the contrary, an examination of the wavelength characteristics (Figure 4.3, Figure 4.4 and Figure 4.5) and the the forward transmission parameters (Figure 4.6, Figure 4.7 and Figure 4.8) illustrates that (1) the magnitude response of all devices are unique and (2) there are localized regions (pass bands) at high frequency where waves that have wavelengths less than two times the largest feature size of the crystal travel through the crystal with little attenuation.

#### 4.2.5 Forward Transmission Parameter Characteristics

The forward transmission parameter,  $S_{21}$ , characteristic is none other than the DFT of the transient response (since the ABC at the crystal input and output effectively cause both the input and output ports to be "matched"). The  $S_{21}$  characteristic for all iterations of the fractal inclusion structures are contained in Figure 4.6, Figure 4.7, and Figure 4.8. The wavelength characteristic is a representation of transfer function phase, while the  $S_{21}$  characteristic is the transfer function magnitude.

Elastic waves that have wavelengths larger than the maximum feature sizes (for example, low frequency elastic waves) appear to propagate through the phononic crystal unaffected, and so all phononic crystals display a low pass property. At higher frequencies, corresponding to shorter wavelengths, the fractal based phononic crystals appear to become frequency selective.

Thus, a phononic crystal appears to have a cut-off frequency above which the

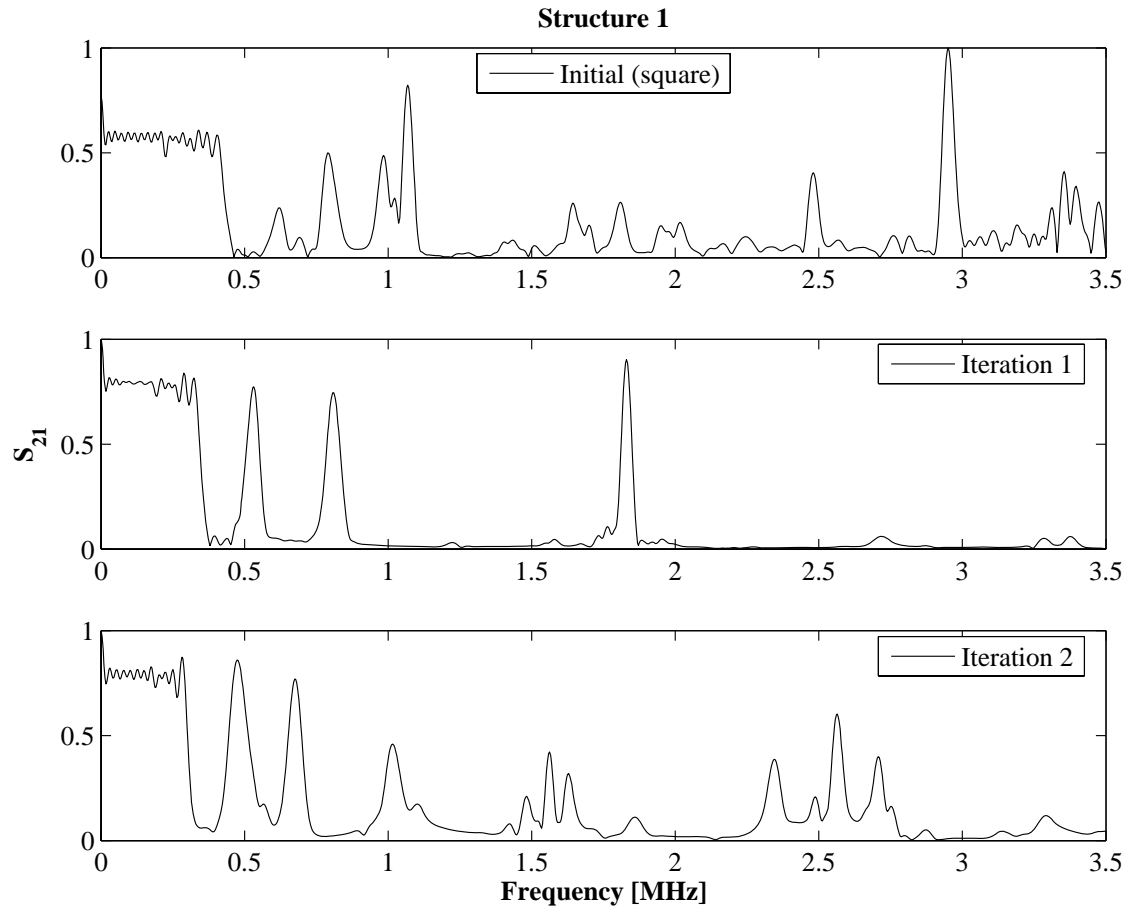


Figure 4.6: Forward transmission parameters for Structure 1.

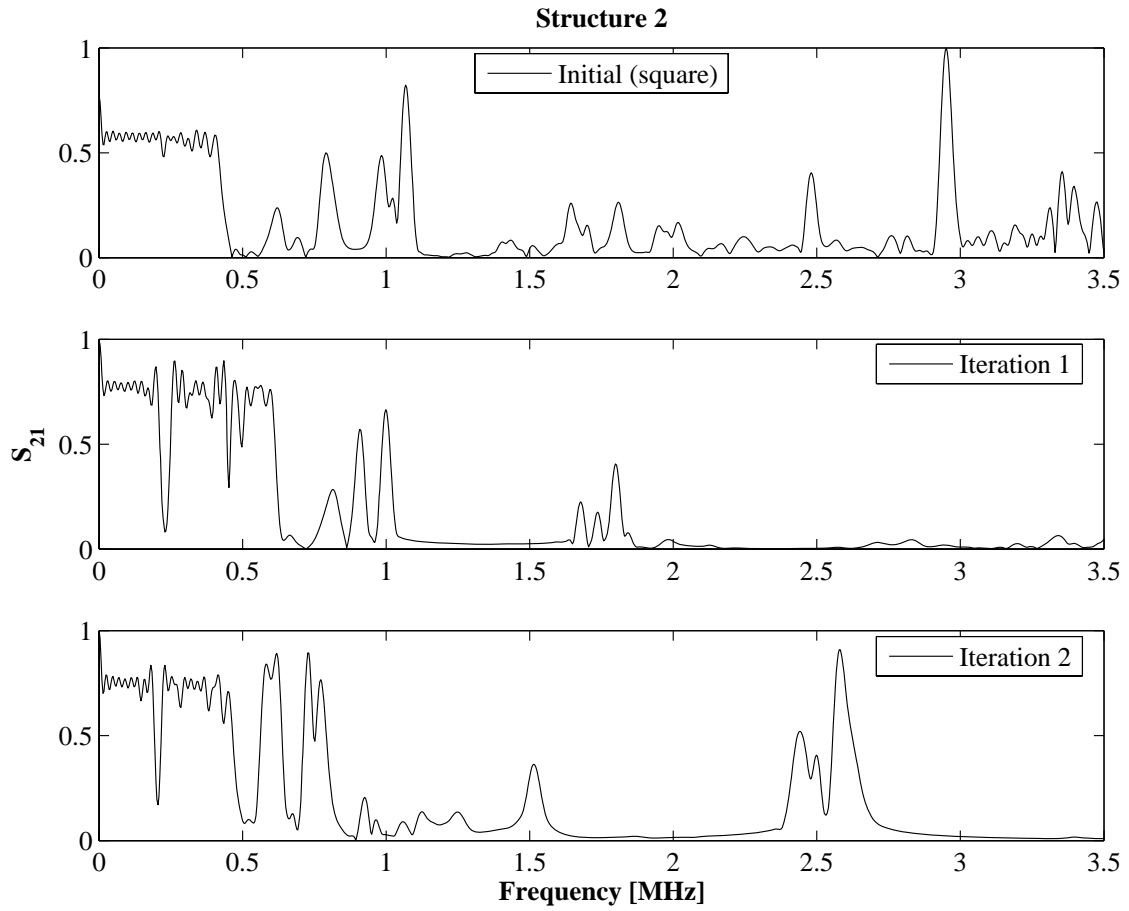


Figure 4.7: Forward transmission parameters for Structure 2.

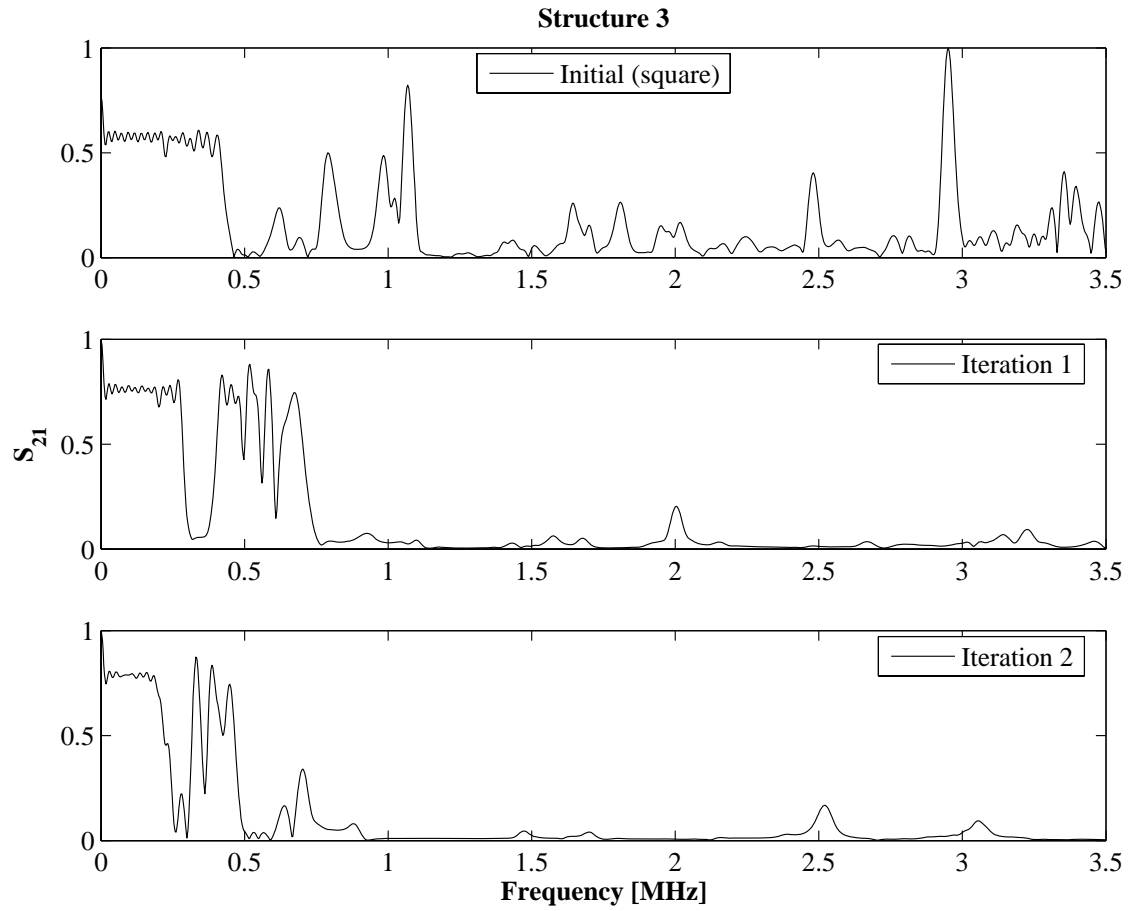


Figure 4.8: Forward transmission parameters for Structure 3.

phononic crystal becomes a frequency selective device. That is, above the lowest cut-off frequency only certain bands of frequencies will propagate through the device - these frequency bands may correspond to a different mode of propagation, or propagation path, through the two-dimensional crystal. This modal behavior mimics that of the rectangular waveguide structures developed for electromagnetic waves.

### Minimum-Phase Characteristics

From filter theory, in minimum-phase conditions there is a relationship between the magnitude and phase response of the system transfer function. The relationship between the magnitude and phase response of a minimum-phase system, with transfer function  $H(\omega) = |H(\omega)|e^{j\Theta(\omega)}$ , is [26]:

$$\Theta(\omega) = -\frac{1}{\pi} \int_0^{\infty} \log \left| \frac{\omega - x}{\omega + x} \right| \frac{d \log |H(x)|}{dx} dx, \quad (4.1)$$

where  $\omega = 2\pi f$  is the angular frequency, and  $|H(\omega)|$ , and  $\Theta(\omega)$ , are the magnitude, and phase, response, respectively.

A qualitative comparison of the wavelength characteristic (a representation of the phase response) and the  $S_{21}$  characteristic of a phononic crystal may provide evidence to suggest that a phononic crystal is a minimum-phase system.

If the phononic crystal is a minimum-phase system in some frequency regimes, this provides some insight into the pole and zero locations of the phononic crystal transfer function. For a minimum phase filter, all poles and zeros are located in

the left-half of the complex plane [27]. A non-minimum phase filter may have zeros in the right-half plane. The poles, on the other hand, must always remain in the left-half plane in order to ensure that causality is not violated.

To illustrate that there may be a relationship between the magnitude and phase response consider, for example, Figure 4.4 and Figure 4.7. At approximately  $0.25[MHz]$  there is a kink in the wavelength characteristic and a valley in the  $S_{21}$  characteristic.

As wavelength becomes smaller than the maximum feature sizes, the previously stated minimum-phase behavior is not easily identified through comparison of wavelength and  $S_{21}$  characteristics. The Bode plot provides a clear illustration of the minimum-phase behavior at high frequency (see Section 4.3.2). It may also be possible that the phononic crystal only displays minimum-phase behavior in some frequency regimes.

The minimum-phase relation for a phononic crystal may differ from that of Equation 4.1. For a phononic crystal, the minimum-phase behavior may potentially be described in terms of the principles of solid state physics.

### **Analogy to Classical Filter Characteristics**

A second result from filter theory, that may be applied in an analysis of the  $S_{21}$  characteristics of Figure 4.6, Figure 4.7, and Figure 4.8, describes the ripple in the pass and stop bands. In filter theory, four classical low pass filter responses are discussed: the maximally flat response, the Chebyshev response, the inverse Chebyshev response, and the Cauer (elliptic) response [28].

The maximally flat response (for example, a Butterworth response) has ripple in neither the pass bands nor the stop bands. The Chebyshev response has ripple in the pass bands, and maximally flat stop bands. The inverse Chebyshev response has maximally flat pass bands and ripple in the stop bands. Finally, the Cauer response has ripple in both the pass bands and stop bands. Hence, from Figure 4.6, Figure 4.7, and Figure 4.8, the fractal based phononic crystal response mimics that of the classical Chebyshev filter response. However, the DFT of the layered structure depicted in Figure 3.17 appears to mimic a Cauer response.

Pass band ripple consists of a succession of crests and valleys. From filter theory, the total number of crests and valleys in a low pass filter pass band, is referred to as the filter order. The filter order is the number of poles in the denominator of the filter transfer function. Examining the low frequency pass band of Iteration 2 in Figure 4.6, one may count 12 crests and 11 valleys, which would imply a low pass filter order of  $12 + 11 = 23$  if the phononic crystal were a Chebyshev filter.

Performing a similar analysis for Figure 4.6, Figure 4.7 and Figure 4.8, one may conclude that the filter order of a phononic crystal is relatively large when compared with, for example, the order of a filter that may be implemented with a reasonable number of operational amplifiers.

A comparison of the classical responses with the phononic crystal response could be extended to discuss the filter roll-off, quality factor and pole and zero locations. Due to the complexity of the phononic crystal response, it is difficult to deduce whether the filter order changes as the fractal inclusion evolves.

### 4.2.6 Band Gap Engineering Functions of Fractals

The  $S_{21}$  characteristics of Figure 4.6, Figure 4.7, and Figure 4.8, suggest that fractal inclusion structures provide multiple pass band characteristics: all  $S_{21}$  characteristics contain multiple stop and pass bands.

Secondly, the evolution of a fractal inclusion structure appears to cause band gap widening. For all fractal inclusion structures, it may be seen in Figure 4.6, Figure 4.7, and Figure 4.8, that after the first iteration of the fractal inclusion structure, stop band attenuation increases in the  $1[MHz]$  to  $3.5[MHz]$  regime.

The evolution of Structure 2 and Structure 3 appears to cause a band gap to form at  $0.25[MHz]$ .

### 4.2.7 Reflection, Refraction, and Diffraction in a Fractal Based Phononic Crystal

Figure 4.9 depicts the amplitude of the lattice vibrations within a unit cell for the phononic crystal that was created using Structure 3. A plane wave source was utilized to induce elastic waves in the longitudinal direction. The direction of the longitudinal component is from the left to right in Figure 4.9. By definition, the direction of wave propagation is perpendicular to the wavefront.

In Figure 4.9, the wavefronts are indicated by continuous black or white stripes. The orientation of the wavefronts (black and white stripes) indicate that many elastic waves do not propagate from left to right. Hence, through reflection, refraction, and diffraction the phononic crystal causes the induced longitudinal elastic wave to





Figure 4.9: Lattice vibrations within the unit cell for the Initial Square Structure (left), Iteration 1 of Structure 3 (center) and Iteration 2 of Structure 3 (right). The amplitude of vibration in the regions that are shaded white are larger than the amplitude of vibrations in the regions that are shaded black.

change direction.

For a longitudinal elastic wave to change direction, the elastic wave must acquire a transverse component. Through reflection, refraction, and diffraction, the phononic crystal thus redirects the induced longitudinal elastic wave energy into transverse directions.

The capacity of the phononic crystal to reflect, refract, and diffract elastic waves into multiple directions, causes the creation of multiple modes of propagation. A mode of propagation is a path that an elastic wave may follow to travel through the crystal.

The mode of propagation that the elastic wave follows as it travels through the crystal may depend on frequency. Thus, the modes of propagation produced by reflection, refraction and diffraction may be the fundamental mechanism from which the dispersive properties and band gap structure of a phononic crystal arise.

### 4.2.8 Fractals For Use In Generalized Boundaries

The successful application of fractal inclusion structures to phononic crystals opens the field to theoretical work in which inclusion boundaries are generalized. Geometrical objects such as Penrose tiles, Hilbert curves [29], Koch curves, or fractals may be suitable for use in work involving generalized inclusion boundaries. The bulk of the inclusion may also be created using such geometrical objects.

For example, the boundary of a square inclusion may be decorated using Hilbert curves, or an entire square inclusion may be built out of Hilbert curves [29]. The properties of a crystal composed of Hilbert curve based square inclusions will likely differ from the properties of a crystal composed of regular square inclusions.

The Hilbert curve based square inclusion may, for instance, display a higher characteristic acoustic impedance [29] than a regular square inclusion. The properties of a phononic crystal built out of such Hilbert curve based inclusions would also change, though the material composition of the crystal may be held constant. For this reason the phononic crystals created using generalized boundaries and bulk geometries would be referred to as meta-materials.

### 4.2.9 Implications of Fractal Structure Simulation Results

The results of this theoretical examination into fractal inclusion based phononic crystals may have practical implications relevant to the fabrication of such crystals in standard silicon processes. As discussed above, the magnitude and phase functions are sensitive to the micro features that are introduced into the inclu-

sion boundary. If fabrication process errors (such as mask errors) introduce micro features into the inclusion boundary, the magnitude and phase response of the fabricated device may drastically deviate from the simulated magnitude and phase response.

Intricate inclusion boundaries may be attained through the use of costly masks that have a small minimum address unit.

### 4.3 Circular Inclusion Based Phononic Crystals

This section contains an analysis of a two-dimensional phononic crystal that is comprised of circular inclusions. The same crystal was studied in [23]. The simulation constants are contained in Table 4.6.

No temporal window was applied to the transient response data, the mean value of the transient response was not subtracted off, the part of the transient response that is zero was not removed, and the DFT was not normalized to the DFT of the host response.

#### 4.3.1 Transient Response

The transient response is depicted in Figure 4.10. As stated in Table 4.6 the amplitude of the input source is  $10^{-6}[cm]$ . As seen in Figure 4.10, the amplitude of the transient response is always less than  $10^{-6}[cm]$  and so the simulation displayed convergence.

Table 4.6: Simulation constants for the simulation of a phononic crystal that is composed of circular inclusions.

Parameter	Value	Units
Source type	Kronecker Delta, amplitude $1 \times 10^{-6}$	[ <i>cm</i> ]
Host material	Aluminium	—
Layer material	Mercury	—
$N_x$	15	[ <i>cells</i> ]
$N_y$	3	[ <i>cells</i> ]
$\Delta t$ Numerator	0.1	—
$\Delta t$	0.997623539	[ <i>ns</i> ]
$\Delta x = \Delta y$	0.0091	[ <i>cm</i> ]
$kmax$	90000	[ <i>time steps</i> ]
$t_o$	7.4	[ $\mu s$ ]
$t_{transient}$	82.385	[ $\mu s$ ]
$acell_{CM}$	0.273	[ <i>cm</i> ]
$acell_{NODES}$	30	[ <i>nodal units</i> ]
Fill Factor	0.22	[ $cm^2/cm^2$ ]

Figure 4.10 indicates that it takes a finite amount of time,  $t_o = 7.4[\mu s]$ , for the signal to arrive at the output ( $t_o$  was given in Table 4.6). The total width of the homogeneous regions is always 4[inclusions], and from Table 4.6 the filter width  $N_x = 15[inclusions]$ , so the total width of the simulated region is  $4 + 15 = 19[inclusions]$ . From Table 4.6 each inclusion is 30[nodal units] wide. Hence, the total width of the simulation region is  $19[inclusions] \times 30[nodal\ units/inclusion] = 570[nodal\ units]$ . The source is always located at node 3, the detector is always located one inclusion (or 30[nodal units]) in from the right edge of the computational domain. Hence the distance from the source to the detector is  $570 - 3 - 30 = 537[nodal\ units]$ , or  $537 \times \Delta x = 4.8867[cm]$  (where  $\Delta x$  is given in Table 4.6).

Using the longitudinal acoustic wave velocity for the aluminium host material

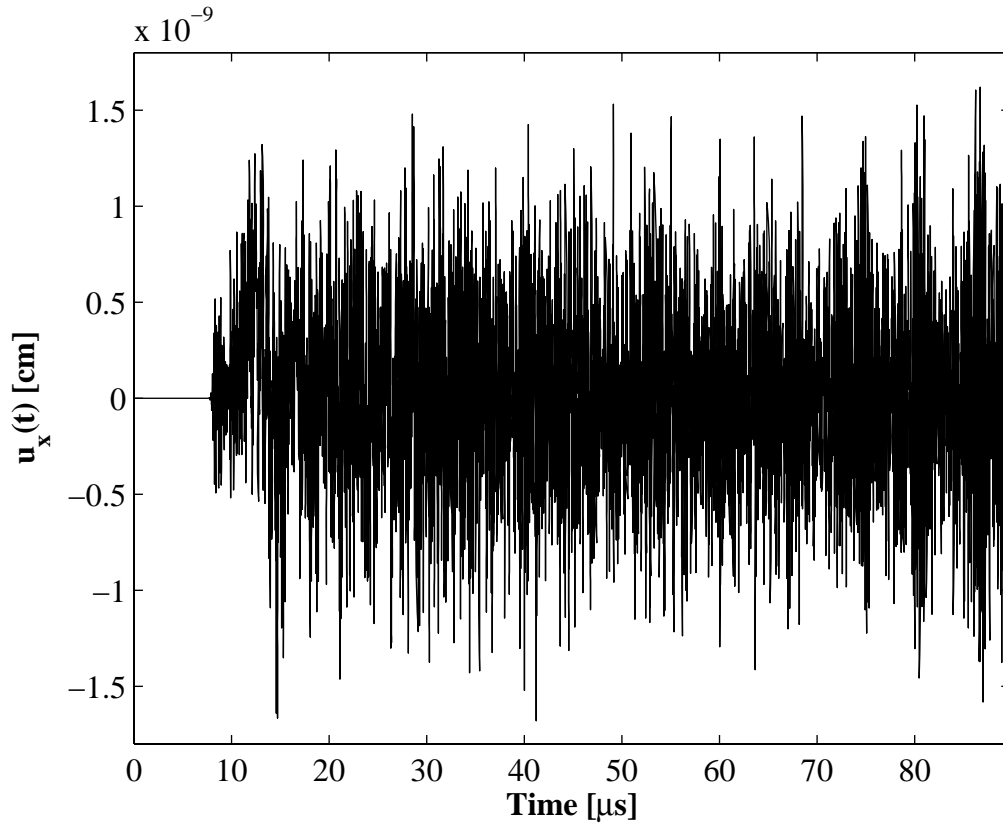


Figure 4.10: Transient response of the phononic crystal that was created using circular inclusion structures.

(see Appendix A) the time it would take a wave to travel from the source to the detector is expected to be  $t = 4.8867[cm]/645000[cm/s] = 7.576[\mu s]$ , which is approximately  $t_o = 7.4[\mu s]$ . Hence the transient simulation produced expected results.

### 4.3.2 Bode Plots

The DFT of the time domain data presented in the previous section, was used to generate the Bode plot of Figure 4.11. The portion of the phase response which corresponds to the low frequency pass band in the magnitude response is non-linear. However, the phase response in the high frequency pass band appears linear.

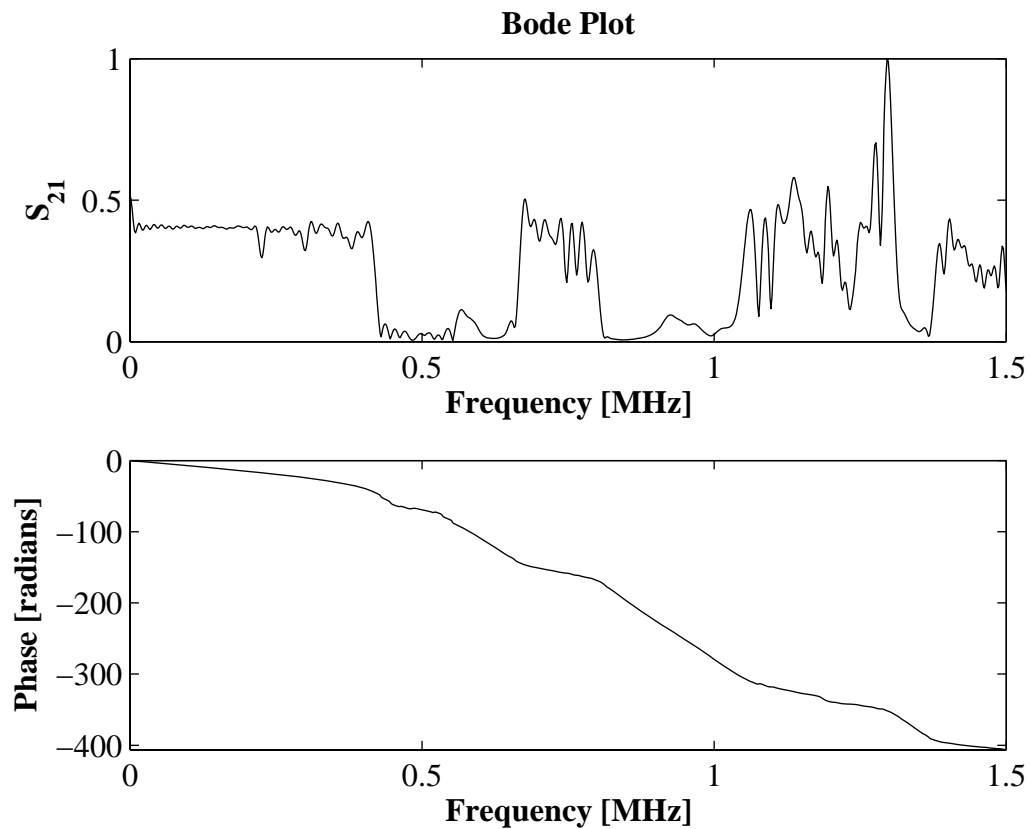


Figure 4.11: The Bode plot that was generated by taking the discrete fourier transform of the transient response of the phononic crystal that was created using circular inclusion structures.

At frequencies corresponding the band gap edges there is an inflection point in the phase response. Thus, the Bode plot supports the observation that there

is some relationship between the magnitude response and the phase response of a phononic crystal.

The normalized magnitude of response of the circular inclusion based phononic crystal is displayed in Figure 4.12 on a logarithmic axis. The attenuation in the band gap is approximately 100 times more than that in the pass band.

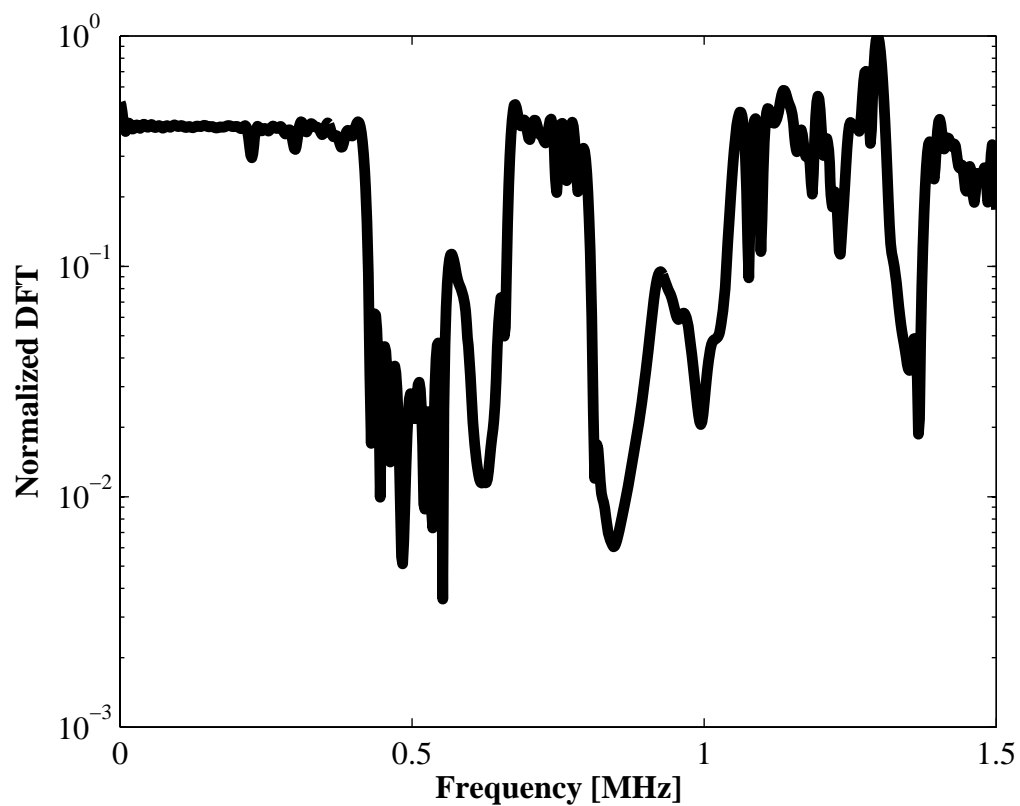


Figure 4.12: Magnitude response on a logarithmic axis.

Below  $0.5[\text{MHz}]$ , the magnitude response contains ripple in the pass and stop bands (a Cauchy response). Above  $0.75[\text{MHz}]$ , the magnitude response contains ripple in the pass bands and maximally flat stop bands (a Chebyshev response).

### 4.3.3 Group Delay Characteristics

By applying Equation 2.9 to the phase response characteristics of Figure 4.11, the group delay characteristic of Figure 4.13 was generated.

There is a small group delay variation in the low frequency,  $0.75[MHz]$ , and  $1.25[MHz]$  pass bands.

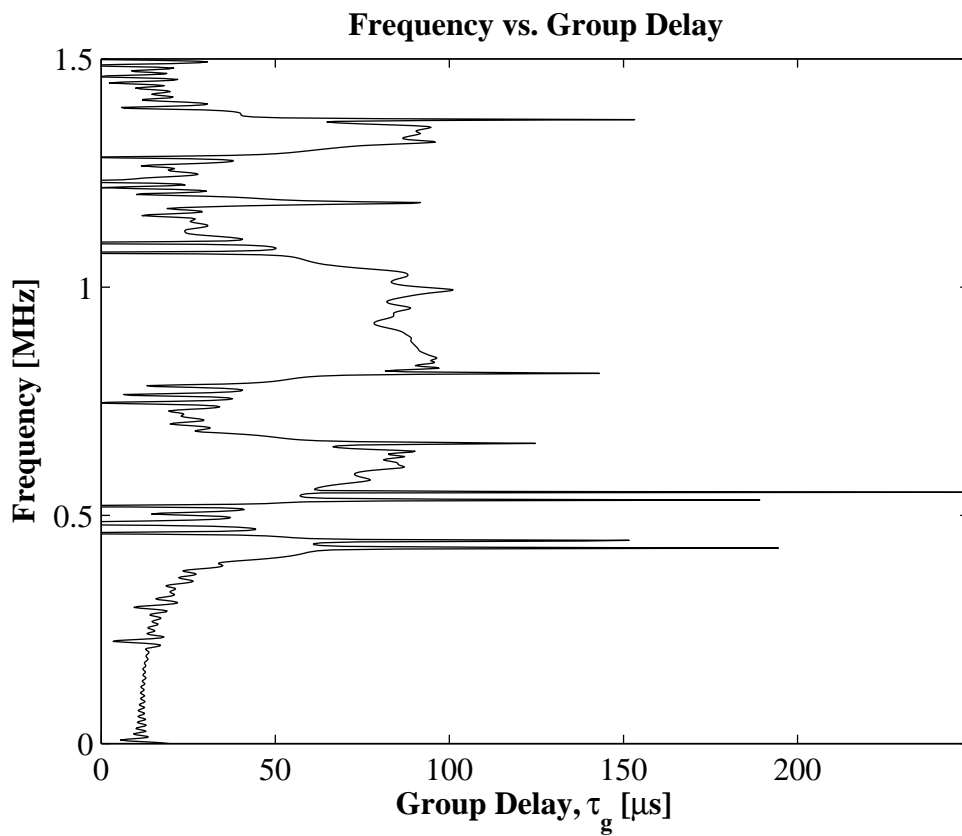


Figure 4.13: Group delay characteristic of the phononic crystal created from circular inclusions.



### 4.3.4 Phase Delay Characteristics

By applying Equation 2.10 to the phase response characteristics of Figure 4.11, the phase delay characteristic of Figure 4.14 was generated.

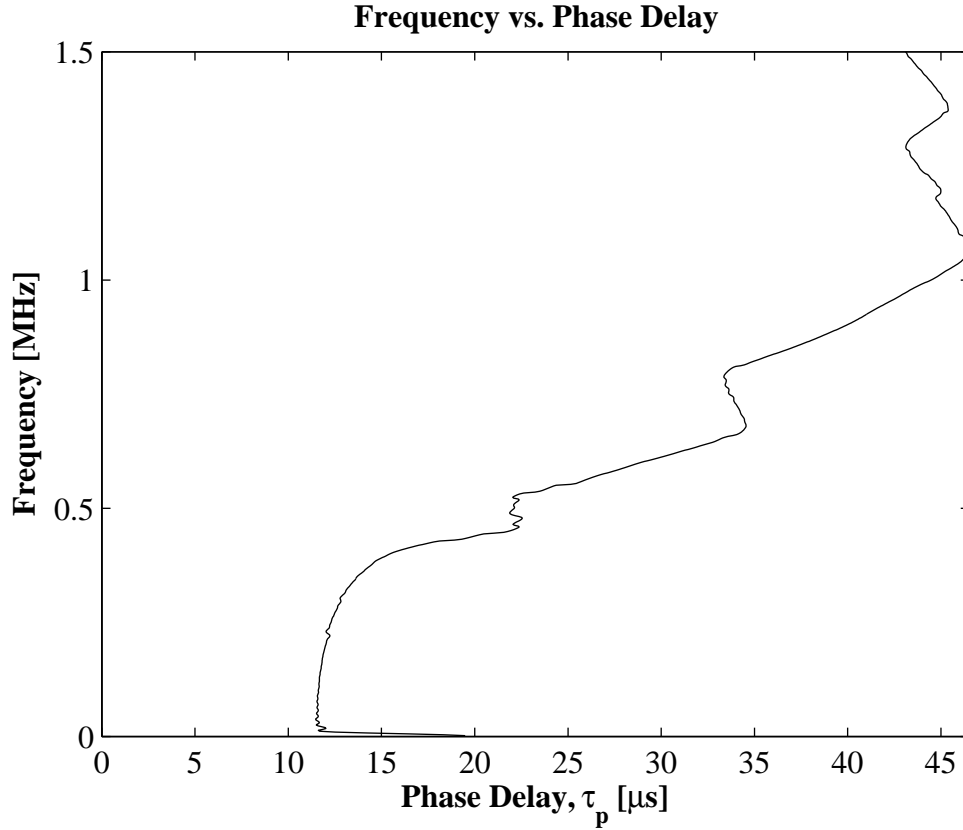


Figure 4.14: Phase delay characteristic of the phononic crystal created from circular inclusions.

### 4.3.5 Phase Velocity Characteristics

Equation 2.13 was applied to the phase delay characteristic of Figure 4.14 to generate the phase velocity characteristic of Figure 4.15. The longitudinal wave velocity,

$c_l$ , of mercury and aluminium are also plotted in Figure 4.15.

The phase velocity characteristic approximates the elastic wave velocity in mercury at high frequencies. However, the phase velocity characteristic tends toward the elastic wave velocity of aluminium in the low frequency pass band. These results support the observation that the properties of the inclusion dominate in determining the response of the crystal when wavelength is small. However, at low frequency when wavelength of elastic waves becomes too large to resolve the inclusion structures the response of the crystal approaches that of the host material.

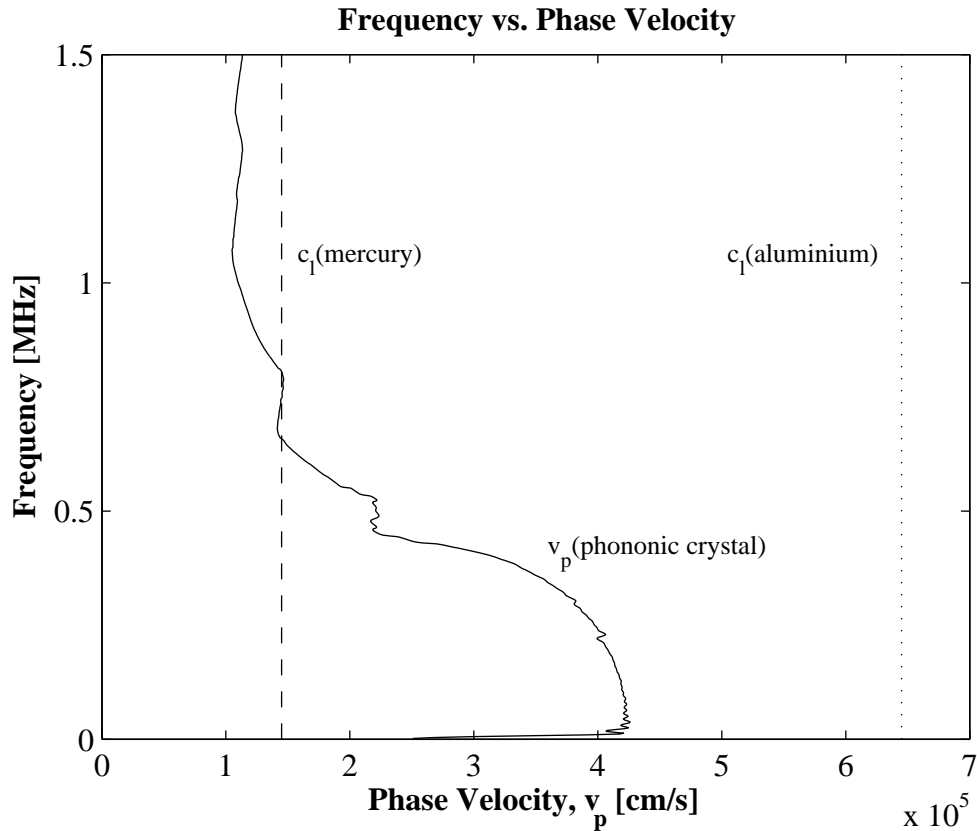


Figure 4.15: Phase velocity characteristic of the phononic crystal created from circular inclusions.

### 4.3.6 Dispersion Characteristics

By applying Equation 2.14 to the phase velocity characteristic of Figure 4.15 the dispersion characteristic of Figure 4.16 was computed. The dispersion characteristic of the phononic crystal approximates that of the mercury inclusion structure in the high frequency pass bands. In the low frequency regime the dispersion characteristic appears to approximate that of the aluminium host material. In the band gaps the dispersion characteristics deviate from both that of aluminum and mercury.

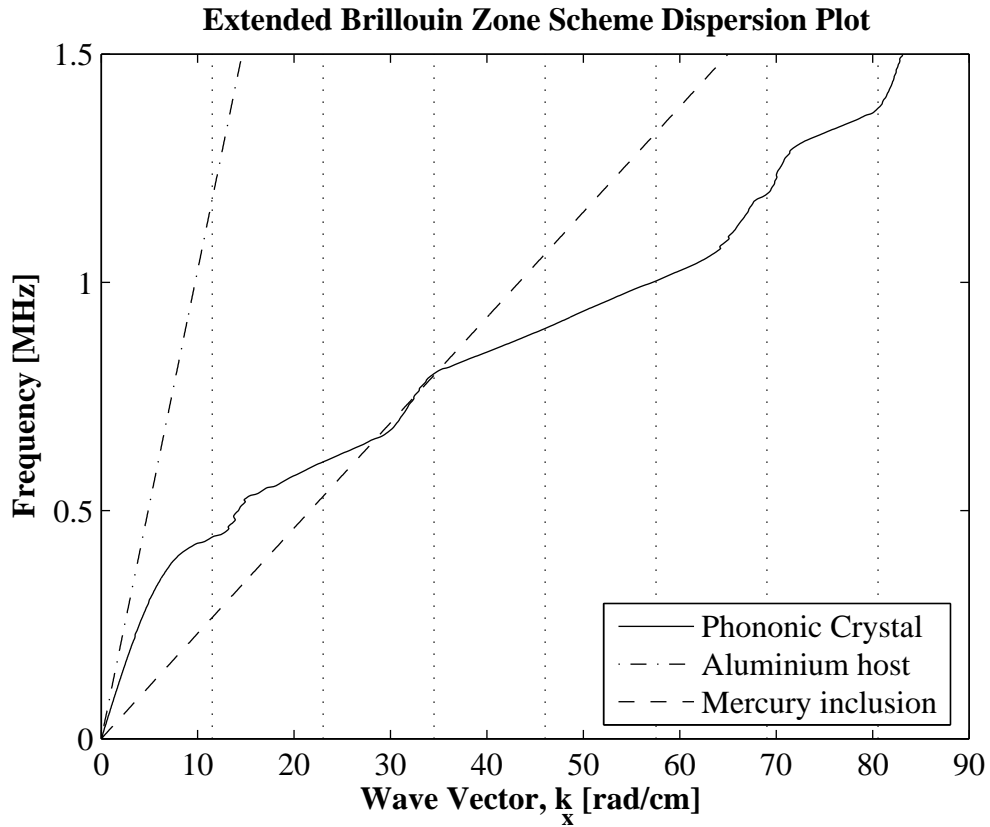


Figure 4.16: Dispersion characteristic of the phononic crystal created from circular inclusions.

### 4.3.7 Quality Factor Characteristics

Lastly, due to the complexity of the magnitude response, the quality factor,  $Q$ , of the phononic crystal was approximated as the derivative of the phase response [30]:

$$Q(\omega) = \frac{\omega}{2} \left| \frac{d(\Theta(\omega))}{d\omega} \right|. \quad (4.2)$$

where  $\Theta(\omega)$  is the phase response given in Figure 4.11.

The phase response of Figure 4.11 contains inflection points - points where the derivative of the phase response is undefined - at frequencies near the band gap edges. Thus, the  $Q$  predicted by Equation 4.2 becomes large near the band gap edges, which is expected. This further supports the observation that phononic crystal may be a minimum-phase filter (the phase characteristic describes pass band slope). Moreover, the  $Q$  is accurately predicted to be relatively small in the pass bands where the magnitude response of Figure 4.11 is almost a constant. These observations support the use of Equation 4.2 in approximating the  $Q$  of a phononic crystal.

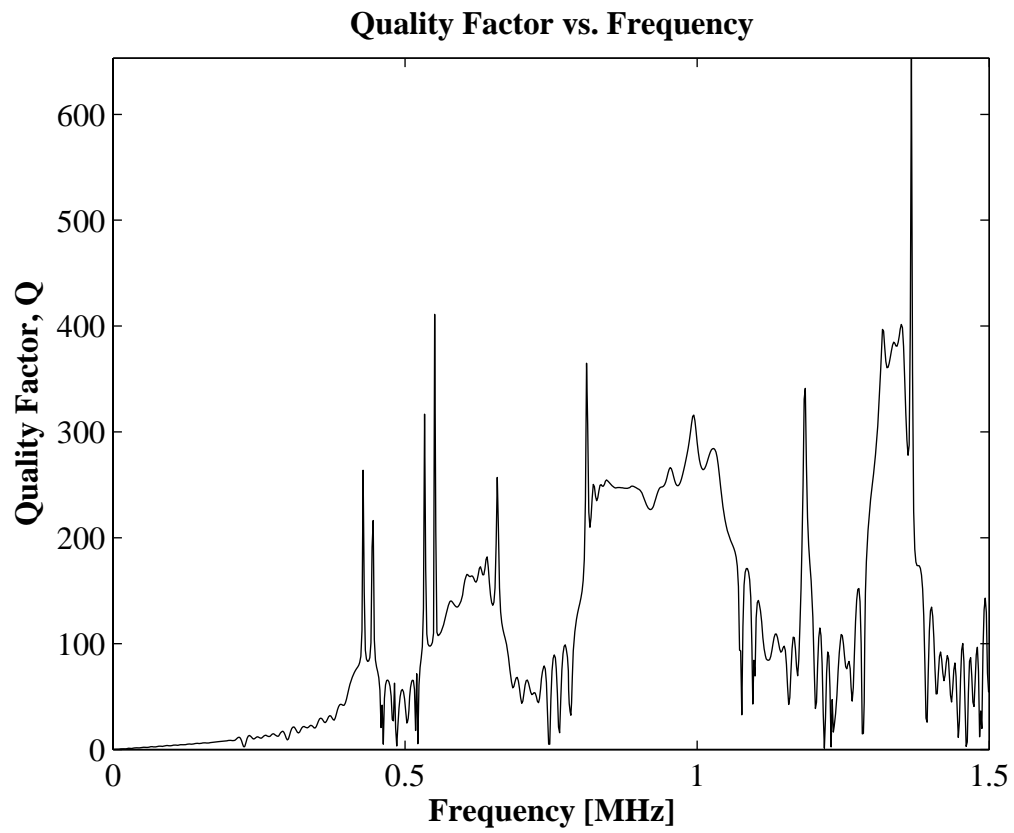


Figure 4.17: Quality factor characteristic of the phononic crystal created from circular inclusions.

## Chapter 5

# Conclusions and Topics for Further Study

First and foremost, advanced research into three-dimensional phononic crystals requires the development of a three-dimensional simulator. The three-dimensional simulator should implement a PML boundary condition and should have the capacity to simulate devices that are composed of more than two materials. The PML boundary condition is necessary to eliminate the reflections that are associated with Mur's first order ABC. The three-dimensional simulator should be capable of simulating MEMS transducers so that phononic band gap filter devices may be simulated.

In this thesis mercury was utilized as an inclusion material. Mercury is not available in standard silicon processes. An investigation should be performed to discover phononic crystals that are (1) composed of materials that are utilized in

standard silicon processes and (2) have band gap features that are useful for filtering applications. Aluminium-air and silicon-air crystals are two examples of phononic crystals that may be fabricated in standard silicon process and may have band structures useful for filtering applications. Other materials that may be utilized as the host and inclusion materials include silicon dioxide, nickel and copper.

Phononic crystal simulation results have been observed to be sensitive to material parameters (density, and transverse and longitudinal elastic wave velocities). The material parameters of a fabricated device will vary with temperature and built in stress. Hence, an investigation of the phononic band gap temperature dependence would be meaningful. Built in stresses should also be modeled.

Advanced study limited to phononic crystals may explore the wealth of crystals that may be created from meta-materials, hexagonal and random lattices, and generalized inclusion boundaries. Phononic crystal analogues of frequency selective surfaces may potentially be designed as absorbing or reflecting layers. Elastic wave lenses may possibly be developed for directing elastic wave energy toward, or from, transducers.

The effect of cascading phononic crystals should be investigated as a form of phononic crystal band gap engineering. A preliminary investigation into the cascading of phononic crystals indicated that the crystals would have to be acoustically isolated before being cascaded. By acoustically isolated it is meant that the crystals may not be fabricated adjacent to one another in a single block of the host material.

Without acoustically isolating each phononic crystal, there appears to be coupling between the crystals that inhibits the overall transfer function of the adjacent

crystals from being equal to the product of the individual crystal transfer functions. By cascading acoustically isolated phononic crystals, the total transfer function of the system may equal the product of the individual crystal transfer functions. Determining a method to efficiently acoustically isolate cascaded phononic crystals may be an important problem to consider.

Two-port network analysis should be applied to phononic crystals to quantify the properties of phononic crystals in terms of RF performance metrics, such as input reflection coefficient, size, insertion loss, quality factor, reciprocity, dispersion, power handling ability, power consumption, temperature coefficient, electrostatic discharge robustness, maximum operating frequency, ability for silicon integration, and parasitic elements.

Phononic crystal based meta-materials may be analyzed using lumped element parameters such as scattering parameters, ABCD parameters, and impedance parameters. Such analysis may reveal interesting properties of the crystals. For example, a scattering parameter analysis may indicate in which frequency regimes the phononic crystal behaves as a capacitive or inductive load. This analysis may allow for the development of mechanical phononic crystal based capacitors and inductors. Phononic crystal based capacitors and inductors would not resemble parallel plate capacitors and spiral inductors.

Using two-port network analysis, the properties of phononic crystal based meta-materials may be quantified in terms of characteristic quantities. Characteristic quantities, such as characteristic acoustic impedance, would be distinguished from actual material properties, such as acoustic impedance. Characteristic quantities



account for non-material properties such as inclusion geometry.

Though phononic crystals appear to possess unique properties, such minimum-phase characteristics and a piecewise linear phase response, a review of dispersive devices may be performed to deduce if any other known devices share similar properties. Such a study would help identify the uniqueness of phononic crystal properties.

Bragg gratings, for example, which are utilized in fiber optic applications, operate based on the principles that govern the layered structure that was discussed in Section 3.7.3. A review of dispersive devices may examine the acoustic devices, many of which possess filtering properties, that may be found in acoustics journals. Such devices may be have the capability for miniaturization.

Investigations into phononic crystal fabrication should survey the minimum feature size of MEMS fabrication processes.

Phononic band gap filters are not a standard devices. Design of phononic band gap filters should occur in parallel with fabrication processes design to ensure that the designed devices will be realizable. Silicon integrated mechanical structures that mimic the operation of ABCs, PMLs, and PBCs may be developed. Collectively this research will aid the fabrication of devices that resemble simulated structures.

Lastly, advanced research into phononic crystals may investigate potential applications, such as filters, phase shifters, audio delay applications, and dispersion compensators. It may also be possible that phononic band gap effects are being observed in existing MEMS devices, however, the engineering community may lack knowledge of the phenomenon.

Research into the development and fabrication of silicon integrated phononic band gap filters presents a wealth of challenges.

# Appendix A

## Material Constants

The utilized material constants are contained in Table A.1.

Table A.1: Material parameters.

Material Name	Density [ $g/cm^3$ ]	$c_l$ [ $cm/s$ ]	$c_t$ [ $cm/s$ ]
Air	0.001225	30000	0
Aluminum	2.692	645000	322000
Mercury	13.51	145000	0
Perspex	1.179	273000	143000
Silicon	2.33	895000	536000
Water	1	148000	0

# Appendix B

## Fractal Inclusion Layout

The layout of each fractal inclusion structure is contained herein. The  $(x, y)$  coordinate pairs, for which  $x$  and  $y$  are even integers, correspond to nodes on the integer-grid. The  $(x, y)$  coordinate pairs, for which  $x$  and  $y$  are odd integers, correspond to nodes on the half-grid. The fractal inclusion structures also occupy  $(x, y)$  coordinate pairs on the intersection of the integer-grid and the half-grid.

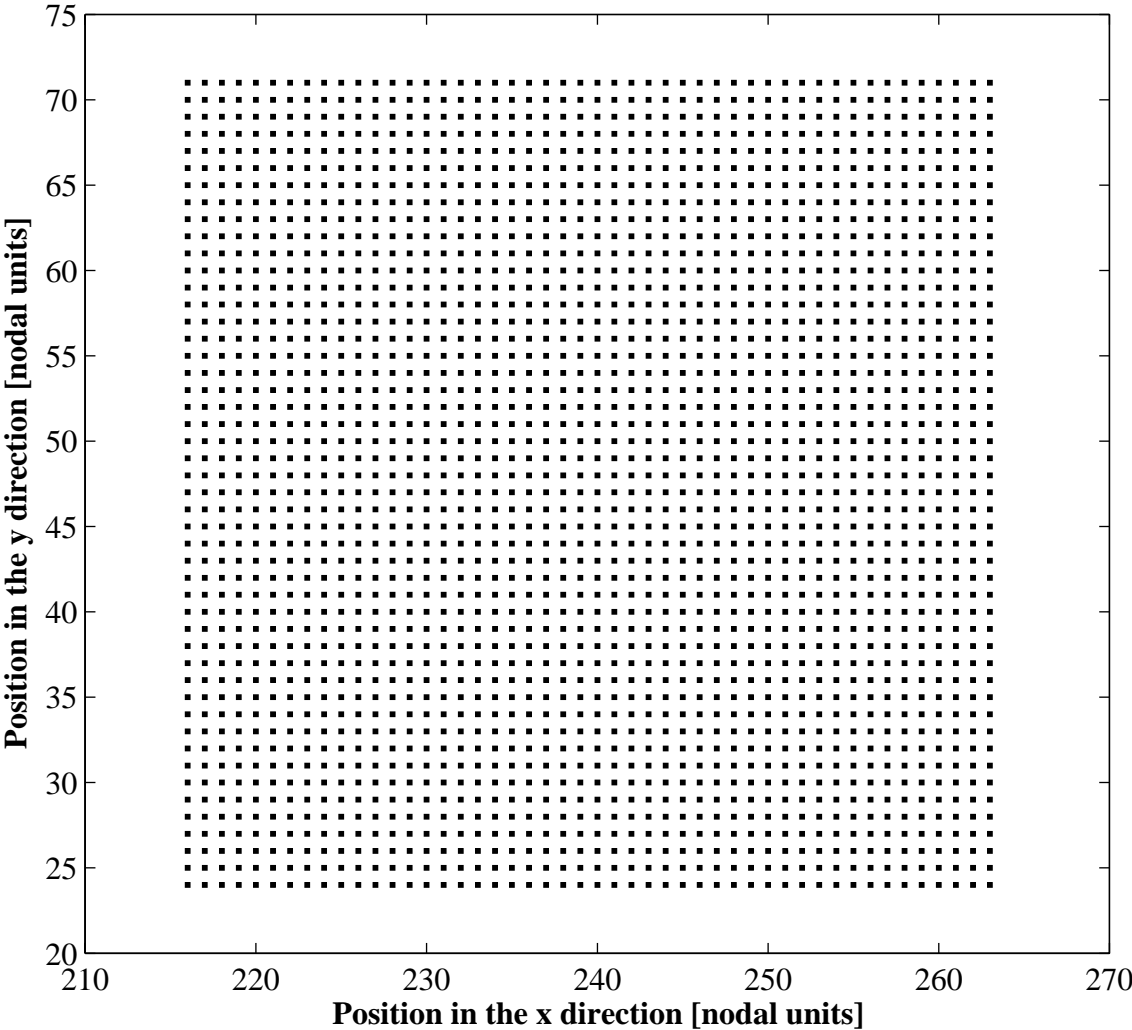


Figure B.1: Layout of Initial Square Structure.

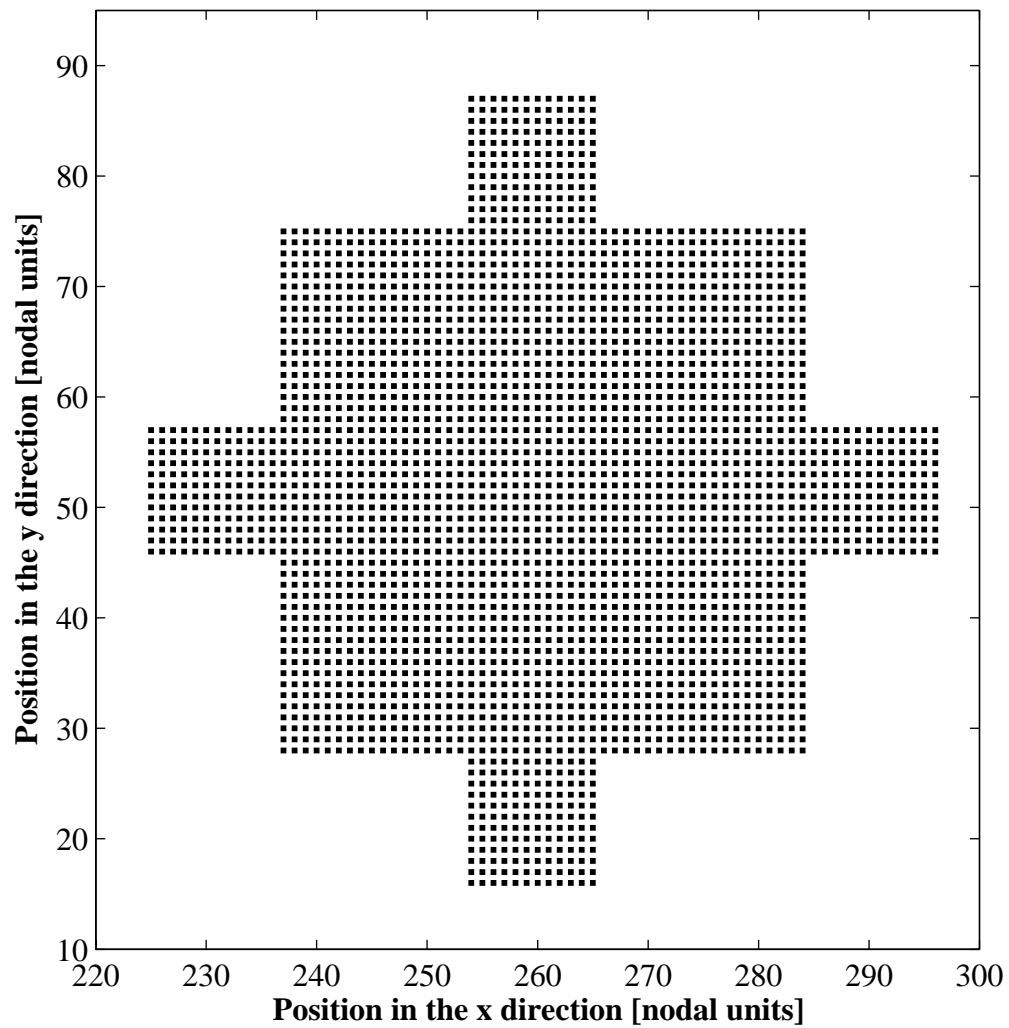


Figure B.2: Layout of Structure 1 Iteration 1.

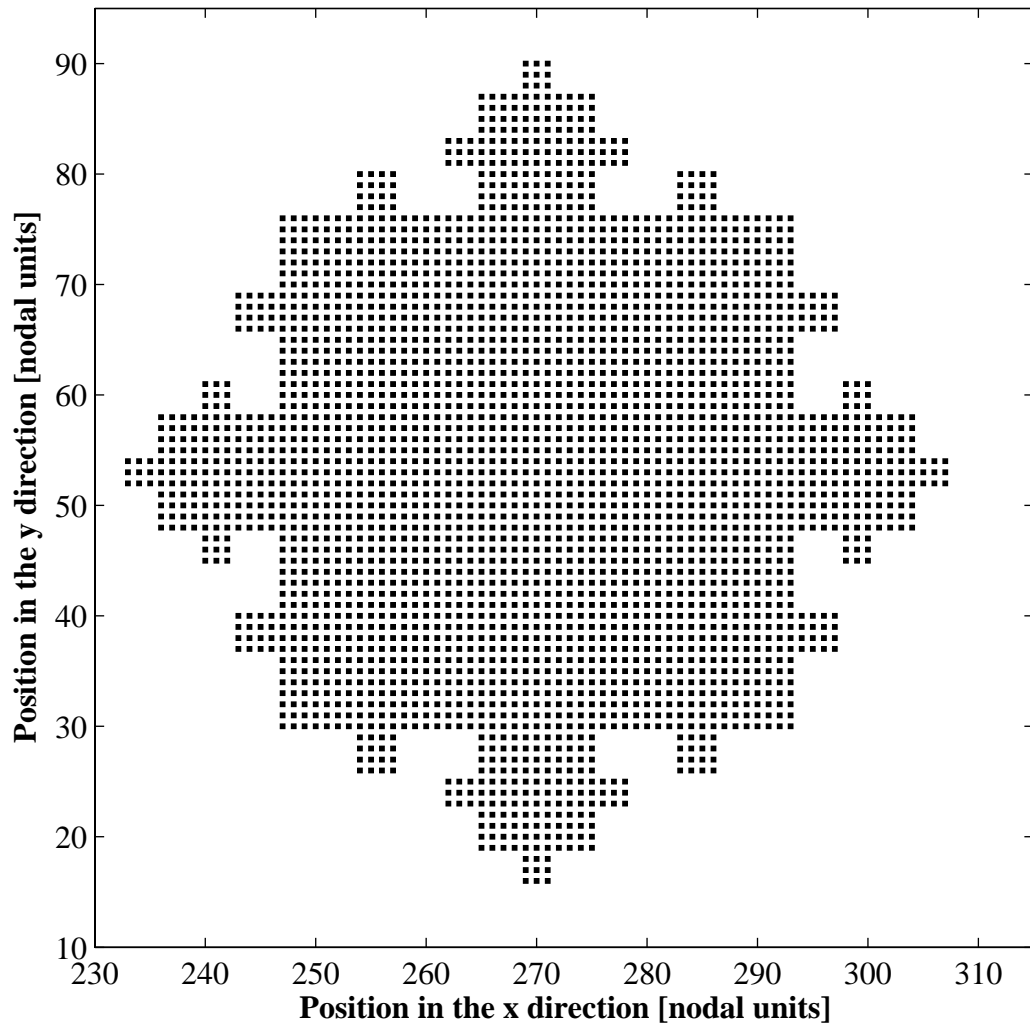


Figure B.3: Layout of Structure 1 Iteration 2.

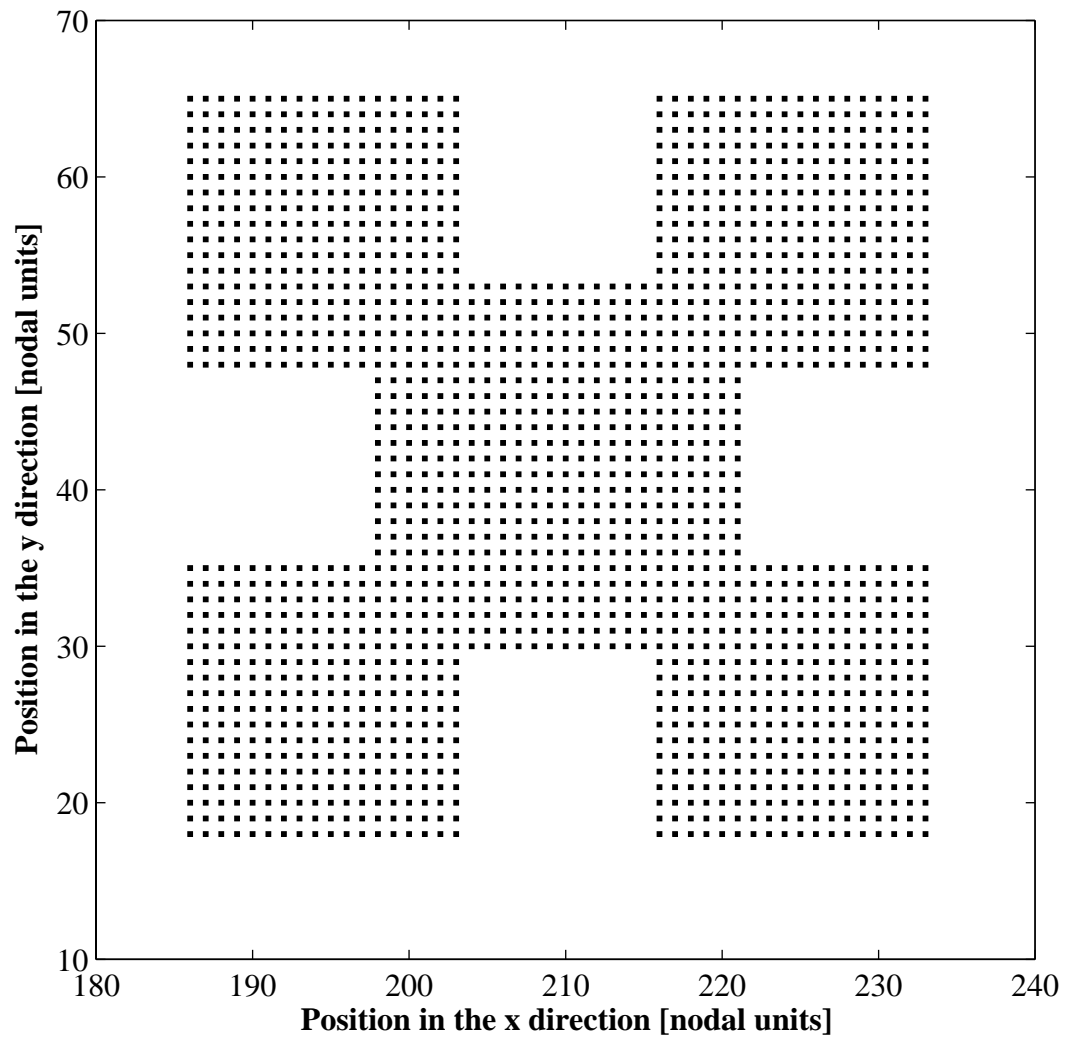


Figure B.4: Layout of Structure 2 Iteration 1.



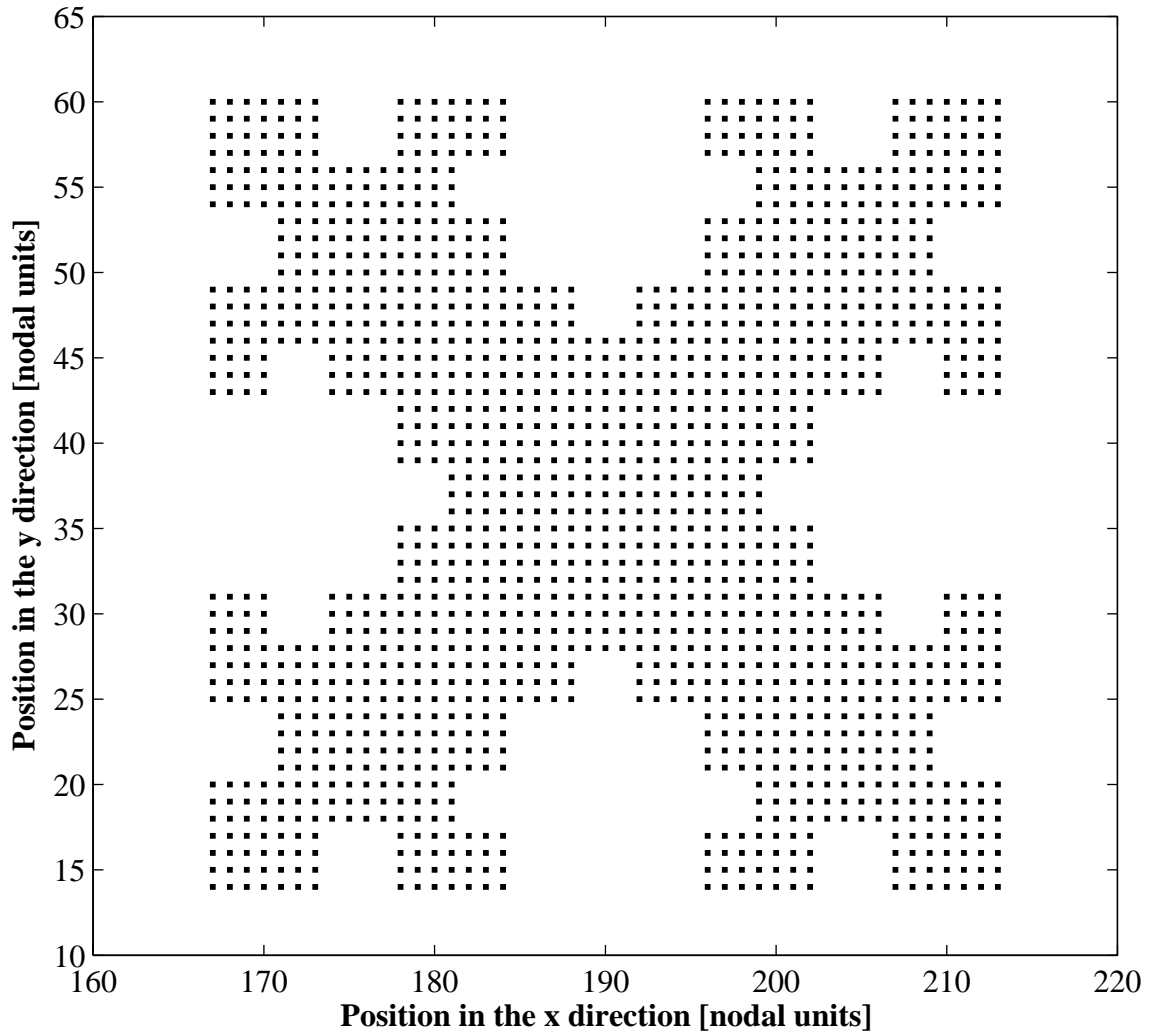


Figure B.5: Layout of Structure 2 Iteration 2.

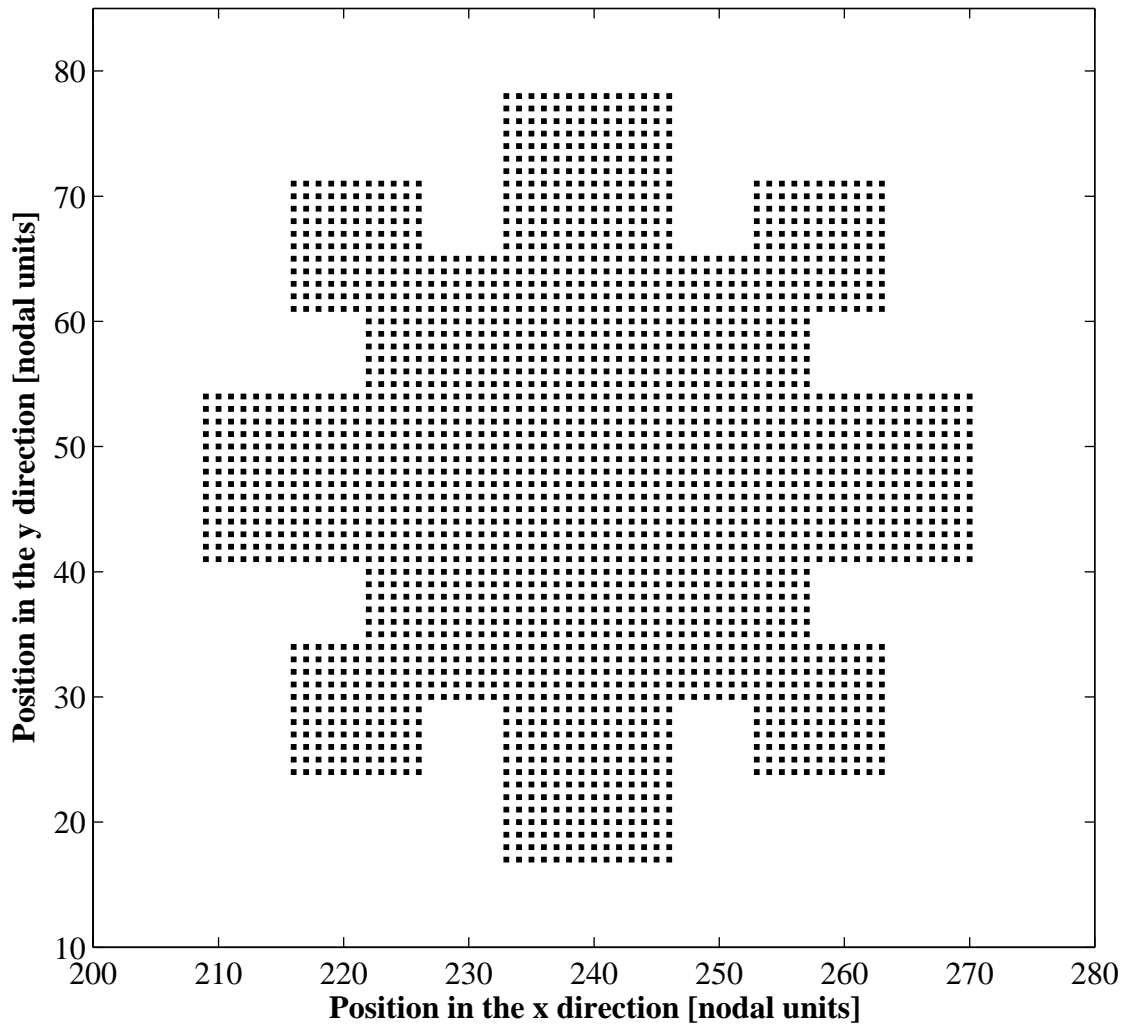


Figure B.6: Layout of Structure 3 Iteration 1.

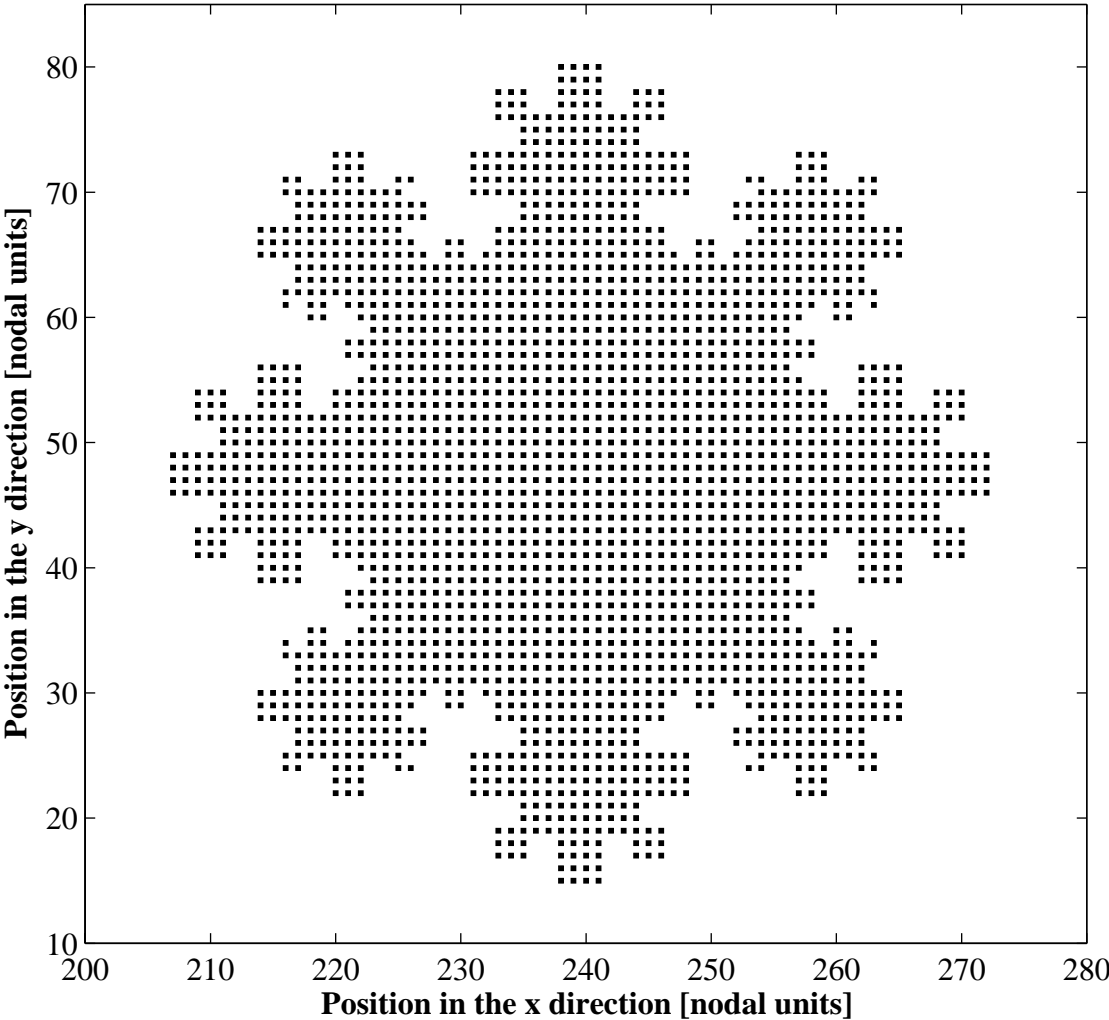


Figure B.7: Layout of Structure 3 Iteration 2.

# Bibliography

- [1] R. W. H. Stevenson, *Phonons in perfect lattices and in lattices with point imperfections*. Edinburgh and London: Oliver and Boyd Ltd., 1966.
- [2] R. Weigel *et al.*, “Microwave acoustic materials, devices, and applications,” *IEEE Transactions on Microwave Theory and Techniques*, vol. 50, no. 3, pp. 738–749, Mar. 2002.
- [3] D. Penunuri and K. Lakin, “RF filter design using LTCC and thin film BAW technology,” *2001 IEEE ULTRASONICS SYMPOSIUM*.
- [4] V. Varadan *et al.*, *RF MEMS and their applications*. Chichester, West Sussex, England: John Wiley & Sons Ltd., 2003.
- [5] M. M. Sigalas and E. N. Economou, “Elastic and acoustic wave band structure,” *Journal of Sound and Vibration*, vol. 158, no. 2, pp. 377–382, 1992.
- [6] M. S. Kushwaha *et al.*, “Acoustic band structure of periodic elastic composites,” *Physical Review Letters*, vol. 71, no. 13, pp. 2022–2025, 1993.
- [7] C. Soukoulis, *Photonic Crystals and Light Localization in the 21st Century*. Netherlands: Kluwer Academic Publishers, 2001.

- [8] Y. Pennec *et al.*, “Tunable filtering and demultiplexing in phononic crystals with hollow cylinders,” *Physical Review E*, vol. 69, pp. 1–6, Apr. 2004.
- [9] C. Nguyen, “Frequency-selective MEMS for miniaturized low-power communication devices,” *IEEE Transactions on Microwave Theory and Techniques*, vol. 47, no. 8, pp. 1486–1503, Aug. 1999.
- [10] F. Ulaby, *Fundamentals of Applied Electromagnetics*. Upper Saddle River, NJ: Prentice Hall, 2001.
- [11] F. Stremmer, *Introduction to Communication System, Third Edition*. Addison-Wesley Publishing Company, 1992.
- [12] Applied Radio Labs. (1999, Nov.) Group delay explanations and applications. DN004.pdf. [Online]. Available: <http://www.radiolab.com.au/DesignFile/DN004.pdf>.
- [13] M. M. Sigalas and E. N. Economou, “Elastic waves in plates with periodically placed inclusions,” *Journal of Applied Physics*, vol. 75, no. 6, pp. 2845–2850, Mar. 1994.
- [14] C. Soukoulis, *Photonic Crystals and Light Localization in the 21st Century*. Netherlands: Kluwer Academic Publishers, 2001.
- [15] J. Berenger, “A perfectly matched layer for the absorption of electromagnetic waves,” *Journal of Computational Physics*, vol. 114, pp. 185–200, July 1993.
- [16] M. Sigalas and N. Garcia, “Theoretical study of three dimensional elastic band gaps with the finite-difference time-domain method,” *Journal of Applied Physics*, vol. 87, no. 6, pp. 3122–3125, Mar. 2000.

- [17] G. Mur, "Absorbing boundary conditions for the finite-difference approximation of the time-domain electromagnetic-field equations," *IEEE Transactions on Electromagnetic Compatibility*, vol. 23, no. 4, pp. 377–382, Nov. 1981.
- [18] K. L. Shlager and J. B. Schneider, "A survey of the finite-difference time-domain literature," pp. 3–5, June 1999.
- [19] W. Chew and Q. Liu, "Perfectly matched layers for elastodynamics: A new absorbing boundary condition," *Journal of Computational Acoustics*, vol. 4, no. 4, pp. 341–359, Apr. 1996.
- [20] K. S. Kunz and R. J. Luebbers, *The finite difference time domain method for electromagnetics*. Boca Raton, Florida: CRC Press Inc., 1993.
- [21] J. Sun and T. Wu, "The study of acoustic band gaps in 2-D air/aluminum and steel/epoxy phononic structure," *Key Engineering Materials*, vol. 270-273, pp. 1127–1134, 2004.
- [22] R. James *et al.*, "Sonic bands, bandgaps, and defect states in layered structures-theory and experiment," *Journal of the Acoustical Society of America*, vol. 97, no. 4, pp. 2041–2047, Apr. 1995.
- [23] D. Garcia-Pablos *et al.*, "Theory and experiments on elastic band gaps," *Physical Review Letters*, vol. 84, no. 19, pp. 4349–4352, May 2000.
- [24] X. Li *et al.*, "Large acoustic band gaps created by rotating square rods in two-dimensional periodic composites," *Journal of Physics D: Applied Physics*, vol. 36, pp. L15–L17, Dec. 2003.

- [25] F. Frezza, L. Pajewski, and G. Schettini, “Fractal two-dimensional electromagnetic bandgap structures,” *IEEE Transactions on Microwave Theory and Techniques*, vol. 52, no. 1, pp. 220–227, Jan. 2004.
- [26] M. Wohlers, “Establishing bounds on the variation of the amplitude and phase of minimum-phase functions,” *IEEE Transactions on Circuits and Systems [legacy, pre - 1988]*, vol. 11, no. 4, pp. 495–496, Dec. 1964.
- [27] T. J. Ulrych and M. Lasserre, “Minimum-phase,” *Canadian Journal of Exploration Geophysics*, vol. 2, no. 1, pp. 22–32, Dec. 1966.
- [28] R. Shaumann and M. E. Van Valkenburg, *Design of Analog Filters*. New York, NY: Oxford, 2001.
- [29] J. McVay, N. Engheta, and A. Hoorfar, “High impedance metamaterial surfaces using Hilbert-curve inclusions,” *IEEE Microwave and Wireless Components Letters*, vol. 14, no. 3, pp. 130–132, Mar. 2004.
- [30] B. Razavi, “A study of phase noise in CMOS oscillators,” *IEEE Journal of Solid-State Circuits*, vol. 31, no. 3, pp. 331–343, Mar. 1996.